Ph.D. Dissertation of Jekwan Lee

Optical Probing of Spin Transports in Topological Materials

위상 물질에서의 스핀 수송에 대한 광학적 연구

February 2023

Graduate School of Physics and Astronomy
Seoul National University
Physics Major

Jekwan Lee

Optical Probing of Spin Transports in Topological Materials

Prof. Hyunyong Choi

Submitting a Ph.D. Dissertation of
Physics

January 2023

Graduate School of Physics and Astronomy
Seoul National University
Physics Major

Jekwan Lee

Confirming the Ph.D. Dissertation written by
Jekwan Lee
January 2023

Chair	Changyoung Kim	(Seal)
Vice Chair	Hyunyong Choi	(Seal)
Examiner	Bohm Jung Yang	(Seal)
Examiner	Dohun Kim	(Seal)
Examiner	Moon-Ho Jo	(Seal)

ABSTRACT

Optical Probing of Spin Transports in Topological Materials

by

Jekwan Lee

Doctor of Philosophy in Physics

Department of Physics and Astronomy

Graduate School, Seoul National University, Seoul, Korea

Thesis supervisor: Professor Hyunyong Choi

The discovery of the topological phase of matter opened a new paradigm in the condensed matter band theory. Significant progress has been achieved in both theoretical understanding and experimental demonstrations, of which the recent advances in device fabrication and measurement methodology played a key role in the accomplishments in the field of experimentation. Among the various experimental approaches to topological phenomena, this thesis focuses on optically probing the spin polarization of electrons. Van der

Waals heterostructure devices had designed to distinguish the spin degree-of-freedom transport from other trivial effects that are expected in optical measurements.

First, I studied the valley Hall effect in MoS_2 without the involvement of exciton dynamics. Such a non-excitonic valley Hall effect was induced by injecting the spin-polarized electrons from the quantum spin Hall states in the monolayer WTe_2. Without the Maialle-Silva-Sham exchange interaction that limits valley coherence lifetime, the valley polarization lasting more than 4 ns was observed while valley Hall mobility exceeds 4.49×10^3 cm^2/Vs. In addition to the exceptional valley Hall transport characteristics, the spatially resolved ultrafast Kerr-rotation microscopy revealed the independence of valley Hall mobility on the valley transport lifetime. This suggests that the observed valley Hall transport is irrelevant to the scattering-induced extrinsic valley Hall contribution, and further comparison with the theoretically computed intrinsic valley Hall contribution verified the dominant role of the intrinsic valley Hall effect, which is determined only by the Berry curvature distribution.

Utilizing the concept of spin-polarized electron injection used in the study of non-excitonic VHE, I investigated the spinful characteristics of the recently proposed higher-order topological insulator. Numerous theoretical studies have been accompanied by rising interest in this new topological

phase of matter, while the experimental study on the practical higher-order topological insulators, especially their spin degree-of-freedom characteristics, have been limited. In this regard, I designed a WTe_2-graphene heterostructure device and observed the spatially resolved Kerr rotation to reveal the topologically protected spinful 1D hinge states embedded in the multilayer WTe_2. In this study, I could successfully characterize the spinful state localized at the hinge of multilayer WTe_2 by measuring the spatially resolved Kerr rotation. Any possible origins of localized spin polarization other than the topological hinge state were excluded through the control experiments performed with a heterostructure device with the modified design. Furthermore, the external magnetic field-dependent experiment proved that the observed spinful states in multilayer WTe_2 are time-reversal invariant.

Key Words

Topological insulators, Anomalous Hall effect, Berry curvature, Spin transport, Ultrafast pulse laser, Van der Waals heterostructure

Student Number: 2019-39865

TABLE OF CONTENTS

LIST OF FIGURES

right-moving (right-up red lines) and left-moving (right-down red lines) modes remains unchanged.

Figure 2.3 Haldane's model for QSHI and Kramers' degeneracy. **a**. The helical edge states are localized at the interface between a QSHI and an ordinary insulator. The intrinsic SOC is responsible for such spin-momentum-locked edge modes. **b.** Two Kramers degenerate points (empty circles) at the TRIM are connected pairwise with each other. The spin-split states between the TRIM intersect Fermi level E_F even number of times. **c.** When the degenerate points are connected, as shown in **c**, the spin-split states intersect E_F odd number of times and cannot be eliminated. In **b** and **c**, only half of BZ is shown since the time-reversal symmetry guarantees the identity of the time-reversal pair in $\boldsymbol{-\pi/a < k < 0}$.

Figure 2.4 Schematic diagrams describing the Hall effect family. From the discovery of the Hall effect based on classical electromagnetism, Hall effects with time-reversal symmetry, spin-degree of freedom, and band-topology-related phenomena were discovered. The figures are adopted from Ref. 36

Figure 2.5 Schematic diagram describing the intrinsic contribution of AHE. The Berry curvature distribution of the system decides the carrier transport transverse to the external electric field while the time-reversal symmetry is conserved. The figure is adapted from Ref. 5

Figure 2.6 Schematic diagram describing the skew scattering (**a**) and side jump (**b**) contribution of AHE. The figure is adapted from Ref. 5

Figure 2.7 Schematic diagram explaining the intrinsic contribution of SHE. The figure is adapted from Ref. 41.

Figure 2.8 Electrical measurement of the SHE induced in graphene/MoS_2 van der Waals heterostructure. The figure is adapted from Ref. 48.

Figure 2.9 Three distinct configurations of the magneto-optical Kerr effect; **a.** Polar Kerr effect, **b.** longitudinal Kerr effect, and **c.** Transverse Kerr effect. The orientation of magnetization is normal to the reflecting surface in the polar Kerr effect regime (**a**). The orientation of magnetization is in both the reflecting surface plane and the plane of incidence in the longitudinal Kerr effect regime (**b**). The orientation of magnetization is in the reflecting surface but normal to the plane of incidence in the transverse Kerr effect regime (**c**).

were performed. The longitudinal field is applied by the bias voltage V_x. The scale bar (white) is 10 μm. **c.** A schematic energy diagram of the MoS_2 (blue) / WTe_2 (orange) heterobilayer. The short-pulse light excitation with energy ε_1 (red) below the bandgap of MoS_2 (Δ) selectively excites the spin-polarized electrons in WTe_2 (black dots). Another light excitation with energy ε_2 (green) is applied to observe the effect of the injected electrons. **d.** The excitonic VHE involves both the unbound (left) and the bound (right) electron-hole pairs. The non-excitonic VHE is unipolar – without exciton formation or dissociation. All measurements were performed at a liquid nitrogen temperature of 78 K.

Figure 3.2 Transport characteristics of the complete device. **a.** Current-voltage output curve along the source and drain. **b.** Current along the source and drain with varying bottom gate voltage.

Figure 3.3 A schematic diagram of the spatially resolved differential PL measurement. While the PL is induced by the 532 nm (2.33 eV) pump that scans the MoS_2 area, a change in the PL signal driven by the chopped 1.55 eV remote pump is recorded. The PL signal is observed by a photodetector combined with the monochromator, and the change in PL according to the existence of the pump is obtained by the lock-in amplifier synchronized with the mechanical chopper.

Figure 3.4 Spatially resolved differential PL across the MoS_2/WTe_2 edge boundary. The A exciton PL signal of MoS_2 is suppressed by the electron transfer from WTe_2. **a.** The spatially resolved 2D PL intensity of the MoS_2 A exciton (V_G = 2 V) is shown for the remote pump with σ^+ polarization (left panel) and σ^- polarization (right panel). The center of the remote pump excitation with the 2 μm waist is fixed at (0, -0.2) μm. The edge of the WTe_2 monolayer is located at the solid black line (y = 0 μm), and the longitudinal electrical bias $\overrightarrow{\boldsymbol{E_y}}$ is applied in the direction of the black arrow. **b.** PL spectrum at (0.25, 0.1) μm, with (red) and without (black) the pump pulse is shown. T and A stand for the resonant energies for the trion and the A exciton of MoS_2, respectively.

Figure 3.5 a. The V_G-dependent PL of the monolayer MoS_2. The black line represents the total PL signal while the red and blue lines denote the exciton and trion components extracted by the Lorentzian fitting, respectively **b.** The spatially resolved differential PL when V_G = 2 V (same figure as Fig. 3.4a). The x-directional deflection of the PL suppression reveals the spin-polarized electron injection and the associated transversal valley Hall transport. **c.** PL spectra when V_G = 2 V, V_G = 3 V without remote pump, and V_G = 2 V with remote pump excitation. **d.** Helicity-resolved PL spectra when V_G = 2 V.

Compared to the PL spectrum without the remote pump (black), the injection of spin-polarized electrons change σ^+ component of the PL (red) while the σ^- component of the PL (blue) is unaffected.

Figure 3.6 Additional data for the spatially resolved differential PL, taken from device #1. The data are shown when V_G is -5 V (**a**) and 6 V(**b**). **a.** When the Fermi level is sufficiently below the conduction band edge (V_G = -5 V), the 1.55 eV pump excitation in MoS_2 has not enough energy to generate any electrons or holes that would be injected into MoS_2. **b.** When V_G = 6 V, the degenerated electron doping of the MoS_2 makes the direct excitation possible by the 1.55 eV pump. **c.** Spatially resolved differential PL (taken from device #1, V_G = 2 V) is presented when the remote pump is linearly polarized. In the absence of the applied longitudinal electrical field, a signature of the valley Hall transport is still observed. The data were taken from device #1 when the polarization of the remote pump is σ+ (**d**) and σ^- (**e**).

Figure 3.7 Experiment data from the TRKR microscopy **a.** 2D snapshot of spatially resolved Kerr rotation angle show the spatial shift of the valley-polarized electron wave packets over time delay Δt at V_G = 2 V. The center of the remote pump was injected at a fixed position of (0, 0) and the probe scanned the designated area at each Δt. The dashed line denotes the *y*-position for the following line-cut plot. **b.** The one-dimensional line-cut plot of the Kerr rotation angle is displayed for several Δts. **c.** The time-domain plot of the transient Kerr rotation angle (black dots) shows fast emerging, and slow relaxation of θ_K. Solid red line shows a fitting curve for the rising and decaying of θ_K signal. Inset: the time-resolved measurement in Fig. 3.7c is done when V_G = 2 V, with the center of the remote pump at (0, 0) μm and the center of the probe at (-0.5, 0.5) μm as denoted by a black dot and white dot on the inset contour plot, respectively.

Figure 3.8 Gate-dependent Kerr rotation dynamics. **a.** Time-resolved Kerr rotation dynamics are shown with increasing V_G from -1.5 V to 4 V. Dots are the measured data, and the solid lines are the fitting curves. **b.** The V_G dependence of the rising time constant acquired from fittings in **a** (black dot with error bar). The obtained time constant is compared with the theoretical expectation (red line, not a fitting curve) computed from the valley Hall conductivity (Eq. (3.6)). Inset: the schematic energy diagram when the V_G = 1.5 ~ 4 V (shaded area), and V_G = 6 V (dashed line). **c.** The V_G dependence of the long decay time constant given by the fitting in **a**. The error bars indicate standard error.

Figure 3.9 Schematic diagram describing the effect of the longitudinal field ($\vec{\boldsymbol{E}}_{\boldsymbol{y}}$) on the electron distribution. K point of the momentum space is expressed as a red dashed line, and the bottom of the conduction band near the Fermi surface E_F is marked as a black dashed line. As V_G increases, the increased amount of electron injection and the higher Fermi surface lead to the change of electron distribution after thermalization from (i) to (ii). Note that Berry curvature is concentrated near at K point. More electrons experience a larger Berry curvature in case (ii) compared to case (i).

Figure 4.1 Crystal structure of multilayer T_d-WTe_2 and experimental design. **a.** The T_d structural phase of multilayer WTe_2 is non-centrosymmetric and has an in-plane mirror plane M_a (red dashed line). **b.** Schematic diagram of the experimental design for detecting the spin-polarized electronic states in WTe_2. The electrical bias voltage makes electrons flow through WTe_2, while the spin polarization of the electrons is optically recorded as the Kerr rotation θ_K induced in the linearly polarized pump (980 nm, 1,415 W/cm^2). The pump laser sweeps through a 6 μm x 10 μm region at graphene near the edge of WTe_2 to obtain the spatially resolved θ_K data.

Figure 4.2 Schematic diagram explaining how the WTe_2-graphene heterostructure device works in this study. **a.** The heterostructure can be modeled as a circuit with two finite resistance connected in a parallel way. The bias voltage applied between two contacts induces a current both through the WTe_2 and the graphene. Electrons injected into graphene from WTe_2 (blue arrow) are optically investigated to determine the spinful characteristics of the electronic states in WTe_2. **b.** Top view schematic diagram of the device explaining the region of the spatially resolved MOKE measurement. The dashed box indicates the range of spatial scanning while the longitudinal electric field is applied to the $-x$ direction. Arrows denote the injection of electrons from WTe_2 to graphene. The localized $\Delta\theta_K$ was expected to appear in the region marked with black circles.

Figure 4.3 Device geometry and electrical characteristics. **a.** An optical microscope image of device #1 with the number index for each metal contact. AFM scan was taken along the yellow line. **b.** The AFM data indicates the thickness of the multilayer WTe_2 flake is ~ 4 nm which corresponds to 5 atomic layers of WTe_2. The thickness of the metal contact shown in the data (30 nm) matches well with the targeted deposition thickness. **c.** The light polarization-dependent SHG was measured at the center of the multilayer WTe_2 in device #1. An 800 nm short pulse with an average intensity of 2,830 W/cm^2 was used as a pump. Anisotropic SHG reveals the crystal axes of the multilayer WTe_2. **d.** Current-voltage output curve of device #1 for each pair of source-drain contacts. All contacts are revealed to form Ohmic junctions. Numbers in the legend indicate the contact combinations used in each measurement. **e,f.** V_G-dependent transfer curve. 0.5 V of drain voltage was applied. **g.** The magnetoresistance of the multilayer WTe_2 was measured in a separate Hall measurement device shown in the inset. The applied gate voltage was 0.9 V, which is close to the charge neutral point. The magnetoresistance does not saturate within $|B_z| \leq 9$ T.

Figure 4.4 The full dataset of spatially resolved V_G-dependent $\Delta\theta_K$ measured in device #1 is shown as 2D contour plots. The bias voltage of 0.5 V was applied to generate a longitudinal electric field in the $+x$ direction, and no external magnetic field was applied. The applied V_G is indicated at the top left side of each panel. The black rectangle indicates the location of the left end part of the multilayer WTe_2. When V_G is between 0 and 1 V, a large $\Delta\theta_K$ is visible at the y position of the hinges, as well as a sign flip of $\Delta\theta_K$.

Figure 4.5 Line-cut plots of $\Delta\theta_K$ at $x = 0.75$ μm. The V_G-dependent $\Delta\theta_K$ in the top panel (0 V $\leq V_G \leq$ 1 V) shows the localized $\Delta\theta_K$ near $y = \pm 1.85$ μm; these y positions correspond to the position of the WTe_2 hinge (black dashed lines).

The V_G-dependent $\Delta\theta_K$s for V_G = -1.5, -1, 2, 3 V are displayed in the bottom panel.

Figure 4.6 B_z-dependent $\Delta\theta_K$ measurement and gap opening of the multilayer WTe_2 due to broken time-reversal symmetry. **a-c.** The line-cut plots show $\Delta\theta_K$ at x = 0.75 μm with varying V_G under B_z = 0.5 T (**a**), 1 T (**b**), and 2 T (**c**) are shown. $\Delta\theta_K$ is featureless at V_G = 1 V when B_z = 0.5 T, while it is flat when the applied V_G is 0.8 V ≤ V_G ≤ 1.2 V under B_z = 1 T. Note that no localized $\Delta\theta_K$ behavior is seen at any V_G when B_z = 2 T. Dashed lines in a-c at y = ±1.85 μm indicate the y position of the WTe_2 hinges in the real space. **d.** Schematic diagrams explaining the band structures show the effect of B_z on the spin-polarized hinge states (black lines) and spin-split bulk bands (colored lines). Because B_z breaks the time-reversal symmetry, Dirac fermions at the topological hinge states gain an effective mass. This opens a finite energy gap, which is proportional to the magnitude of B_z. The gap opening appears as a flat $\Delta\theta_K$ along y since the Fermi level falls within the gap. The dashed lines in the diagram indicate the Fermi levels when V_G is 0, 1, and 1.5 V. For the case when B_z = 2 T (**d**), the schematic represents one possibility that the hinge states are merged into the bulk band due to the induced gap in the hinge states.

Figure 4.7 Additional experiment proposed to isolate the hinge characteristics (device #4). **a.** An optical microscopy image of device #4 is shown. Two monolayer graphene flakes are separated by a 1.5 μm gap. The graphene layer for the electron transport measurement is located below WTe_2. **b, c.** Schematic representation for the expected $\Delta\theta_K$ distribution when the spin-polarized electrons in graphene originate from the WTe_2 hinge states (**b**) and bulk (**c**). Dashed rectangles are the spatial windows where the MOKE measurements were performed. The black arrows represent electron transport.

Figure 4.8 The full dataset of spatially resolved V_G-dependent $\Delta\theta_K$ measurement (device #4). 2D contour plots of the V_G-dependent $\Delta\theta_K$ from device #4 when $B_z = 0$ (**a**) and $B_z = 1$ T (**b**). Dashed lines indicate the edge of graphene flakes with the 1.5 μm gap between them. The black rectangle indicates the location of the top-end part of the multilayer WTe_2. If the spin Hall contribution is the dominant origin of the observed $\Delta\theta_K$, additional peaks and deeps should appear near the dashed line, as described in Fig. 4a. However, the distribution and V_G dependence of $\Delta\theta_K$ is not affected by the existence of a graphene gap.

Figure 4.9 Line-cut plot from the spatially resolved V_G-dependent $\Delta\theta_K$ measurement in device #4. The line-cut plots are obtained from the 2D contour plots of $\Delta\theta_K$ at x = 0.3 μm with varying V_G under B_z = 0 T (**a**) and 1 T (**b**), which corresponds to Fig. 4.8a and Fig. 4.8b, respectively. Dashed lines indicate the x position of the WTe_2 hinges in real space. Similar to the result from device #1 (Fig. 4.6), suppression of $\Delta\theta_K$ near the hinge due to the mass gap opening occurs when V_G = 0.8, 1 V.

Figure 4.10 The temperature-dependent spatially resolved $\Delta\theta_K$ when V_G = 0 V (**a**) and V_G = 2 V (**b**). No magnetic field was applied. Solid rectangles indicate the location of the left end part of the multilayer WTe_2. Dashed rectangles indicate the area where $|\Delta\theta_K|$ was obtained for each case. The exact positions of the marked area are 0 μm < x < 1.24 μm, 1.7 μm < y < 2.3 μm for **a**, and 0 μm < x < 1.25 μm, $|y|$ < 0.6 μm for **b**.

Figure 4.11 Temperature-dependent $|\Delta\theta_K|_{avg}$ obtained from the spatially resolved $\Delta\theta_K$ measurement shown in Fig. 4.10. The error bars indicate the standard variation of the $|\Delta\theta_K|_{avg}$ for each case.

Figure 4.12 Spatially resolved V_G-dependent $\Delta\theta_K$ with the bias voltage of 0.5 V along the *b*-axis. Black rectangles indicate the top-end part of the WTe_2 flake. No magnetic field was applied.

Table 3.1 Comparison of valley Hall mobility and longitudinal mobility.

CHAPTER 1 - INTRODUCTION

The observation of the quantum Hall effect in the late 20th century led to the suggestion of the topological order as a new paradigm for condensed matter classification[1-4]. Over the next few decades, the topological phase of matter has become one of the most notable topics in the field of condensed matter physics. Today, we can now systematically predict the topological phase of materials and their peculiar properties through solid theoretical bases. Along with the advances in theoretical understanding of topological materials, the experimental research method has made great progress based on the development of technology. The optimization of material growth methods helped explore the intrinsic properties of topological materials[5], advanced device fabrication processes led to more precise electronic transport experiments using exquisite electronic devices[6-8], and state-of-art methods such as angle-resolved photoemission spectroscopy (ARPES) made the explicit investigation of the electronic band possible[9-11]. Above all, the optical study on the band topology of the condensed matter system is one of the fields that has grown rapidly in line with the advance in laser optics.

Optical studies on topologically non-trivial states have been conducted[12-14], and the plasmonic characteristics of the surface states have also been studied[15,16]. Moreover, the introduction of ultrashort pulse laser opened a new chapter throughout condensed matter physics as well as the research of topological materials[17-19].

1.1 Motivation

Observing optical properties and analyzing the light-matter interaction in a condensed matter system has merits in understanding quantum mechanical phenomena in condensed matter systems; one can always choose optical excitation with spatial, temporal, and spectral conditions suitable for the investigation. Furthermore, spin angular momentum conservation during the optical transition and magnetization-dependent electric permittivity of a material guarantee spin-sensitive excitation and detection in optical experiments. Therefore, with properly designed devices, optical methodologies can be used as powerful tools to analyze and visualize the intrinsic properties of a material when the material has peculiarities in the spin degree of freedom or the geometric phase of the electron, as in topological materials.

Making optoelectronic devices happened to be something that I have learned since the beginning of my graduate studies. Hence, as soon as I came across the concept of band topology, I was fascinated by the possibility of exploring spin- and topology-related phenomena using optoelectronic devices. In particular, I tried to look for the answers to the questions that were still remaining for practical reasons, such as valley Hall dynamics of free electrons in MoS_2 or spin characteristics of the highly confined one-dimensional (1D) state in 3D crystal, by overcoming the limitations of the traditional optical experiments through devising new methodology based on well-established experiments.

1.2 Thesis highlights

In this dissertation, I will present my work on revealing spinful phenomena that are derived from the band topology of 2D materials. There are five chapters, including this introduction.

In Chapter 2, the theoretical background and details of the device and experiments are described. First of all, the basic concept and brief history of the topological insulators (TIs) and anomalous Hall effect (AHE) are introduced. Secondly, the magneto-optic Kerr effect (MOKE) is explained as observing the polar Kerr effect was the key method for detecting electron spin polarization in my studies. Lastly, the experiment setup I constructed for the experiments and details of the device fabrication process is discussed.

In Chapter 3, the “non-excitonic” valley Hall effect (VHE) in MoS_2 and its dynamic properties are demonstrated. Employing the non-excitonic VHE which was achieved by injecting spin-polarized electrons from the monolayer WTe_2, I observed a long valley polarization lifetime of more than 4 ns and valley Hall mobility exceeding 4.49×10^3 cm^2/Vs. These valley transport properties are orders of magnitude larger than the exciton-involved VHE, which is constrained by the fast valley depolarization of exciton due to the Maialle-Silva-Sham exchange process. The origin of the non-excitonic VHE is also investigated in this study. From the spatially resolved ultrafast Kerr-rotation microscopy, it is confirmed that the intrinsic VHE contribution caused by the Berry curvature distribution is dominant over the scattering-dependent extrinsic contribution.

In Chapter 4, I show the experimental evidence supporting the spinful hinge state protected by the time-reversal symmetry in the multilayer WTe_2. Based on the theoretical prediction that the multilayer T_d-WTe_2 may be a higher-order topological insulator (HOTI), few recent studies have shown there are 1D conducting channels confined at the hinges of the multilayer WTe_2. For further investigation, I designed a WTe_2-graphene heterostructure device and observed the spatially resolved Kerr rotation to reveal the spin configuration of the hinge states. The external magnetic field dependence of spatially resolved differential Kerr rotation evidenced that the multilayer WTe_2 hosts helical, spinful, and time-reversal invariant hinge states. In this study, the alternative origins of the differential Kerr rotation, such as AHE, are ruled out through the control experiments to ensure the existence of spinful hinge states.

CHAPTER 2 – THEORETICAL FOUNDATIONS AND KEY METHODS

2.1 Topological insulators

2.1.1 Introduction

An atomic insulator and semiconductor can be regarded as having the same phase in a broad sense. They both have an energy band gap that separates the empty conduction band from the occupied valence band. Although the size of the energy gap is different for each material, one can continuously transform the Hamiltonian of a system to the Hamiltonian of another without closing the energy gap in general. However, the discovery of the integer quantum Hall effect (QHE) revealed a new insulating phase that cannot be continuously deformed into an ordinary insulator while conserving the energy gap. The quantum Hall insulating phase arises when an external magnetic field is applied to 2D electron gas[20]. The strong magnetic field induces cyclotron motion of electrons that forms quantized Landau levels, and when the given system is a 2D crystal, the periodic potential leads to the gapped Landau band structure which is identical to the gapped band structure of an ordinary insulator. In spite of the similarity of band structure, the quantum Hall insulating phase has a quantized Hall conductivity

$$\sigma_{xy} = \frac{Ne^2}{h}. \quad (2.1)$$

The distinction between an ordinary insulator and a quantum Hall insulator (QHI) can be explained by the "topology" of their band structure.

2.1.2 Topological band theory: quantum Hall insulator

The Bloch Hamiltonian describing the gapped band structures can be distinguished into the equivalence classes of Bloch Hamiltonians that can be adiabatically transformed into one another without closing the energy gap. These classes can be characterized by a topological invariant that is associated with the Berry phase of the Bloch wave function[1]. In 1982, Thouless, Kohmoto, Nightingale, and den Nijs (TKNN) proposed a topological invariant $n \in \mathbb{Z}$ which is now known as Chern number or TKNN invariant,

$$n_i = \frac{1}{2\pi}\int d^2\mathbf{k}\mathcal{F}_i, \ (2.2)$$

where $\mathcal{F}_i = \nabla_k \times i\langle u_m|\nabla_k|u_m\rangle$ is the Berry curvature of the band, while u_i is the Bloch wave function and *i* is an index for a band.

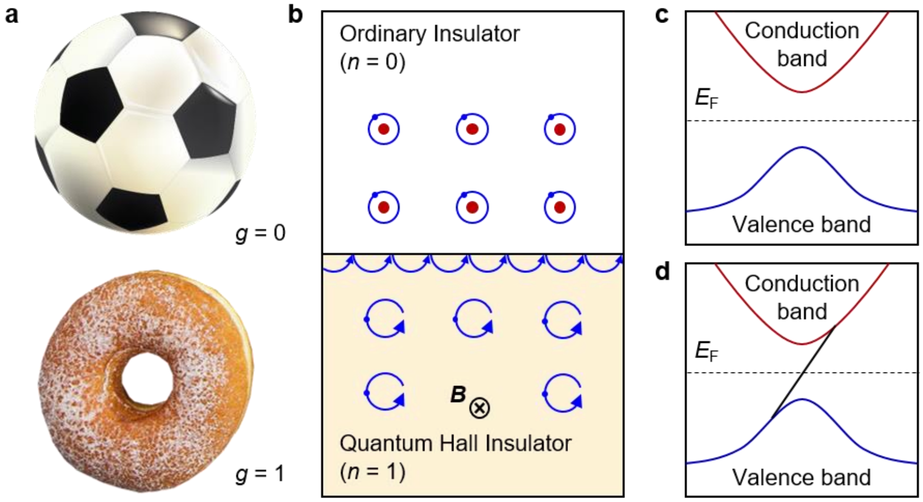

Figure 2.1 Topology and quantum Hall effect. **a.** A ball and a doughnut have a distinct topology that is characterized by the number of "holes" g. Here, g can be computed by integrating the Gaussian curvature over the surface. **b.** A quantum Hall insulator and its interface with the ordinary insulator. The skipping motion of electrons along the boundary of the quantum Hall insulator forms a chiral 1D conducting channel. **c.** A schematic band structure of an ordinary insulator with a finite bandgap. **d.** In the quantum Hall insulator, the chiral boundary states appear as a gapless in-gap mode.

Note that Chern number n_i denotes the total Berry curvature in the Brillouin zone (BZ) and cannot be changed by the smooth variation of the Hamiltonian as a topological invariant analogous to the genus of a 3D object in topology (Fig. 2.1a). In the perspective of physical interpretation, the Chern number denotes the electric polarization difference induced by the adiabatic threading of a magnetic flux quantum through the cylinder, as described by Laughlin's argument[2]. As a topological invariant, n_i classifies bands into equivalent classes while the physical realization of it is directly related to the quantum Hall conductivity σ_{xy}; the Kubo formula expression of σ_{xy} in Eq. (2.1)

$$\sigma_{xy} = \frac{Ne^2}{h} = \frac{e^2}{2\pi h}\int d^2\boldsymbol{k}\mathcal{F}_i, \text{(2.3)}$$

shows that N is identical to n_i in Eq. (2.2). This suggests that the quantization and quantized value of σ_{xy} is robust against any perturbation that alters the Hamiltonian smoothly.

From the practical point of view, the fundamental of quantized σ_{xy} can be understood by the "skipping" motion of electrons near the edge of a QHI (Fig. 2.1b). Due to the presence of an edge, the cyclotron motion of electrons cannot be completed, forming the chiral edge state of one-directional propagation along the interface between the QHI and an ordinary insulator. Regarding the chiral edge state as a product of forced cyclotron motion, it is clear that the backscattering of electrons from any non-magnetic disorder is forbidden. Such a robust chiral transport is the background of the strict quantization of σ_{xy}.

Graphene under a periodic magnetic field provides a compact model for the understanding of QHE in terms of the topological band theory. Starting from the 2×2 Bloch Hamiltonian for graphene $H(\mathbf{q}) = \hbar v_F \mathbf{q} \cdot \vec{\sigma}$ where relative momentum $\mathbf{q} \equiv \mathbf{k} - \mathbf{K}$ is defined by the corner of BZ $\mathbf{K}$ (and $\mathbf{K}' = -\mathbf{K}$) and v_F is Fermi velocity, the inversion and time-reversal symmetry make $H(\mathbf{q})$ a 2D massless Dirac Hamiltonian with the degenerate Dirac point protected by the combination of both symmetries. Here, the violation of inversion symmetry makes the Dirac Hamiltonian massive and leads the system to become an ordinary insulator with the dispersion $E(\mathbf{q}) = \pm\sqrt{(\hbar v_F \mathbf{q})^2 + m^2}$ that has a $2|m|$ of the energy gap. On the other hand, breaking time-reversal symmetry by the periodic magnetic field that follows the symmetries of honeycomb lattice makes $\mathbf{K}$ and $\mathbf{K}'$ have masses with opposite signs[21]. In this system setup which is called the Haldane model, the gapped state has $\sigma_{xy} = e^2/h$ as a QHI.

2.1.3 Bulk-boundary correspondence

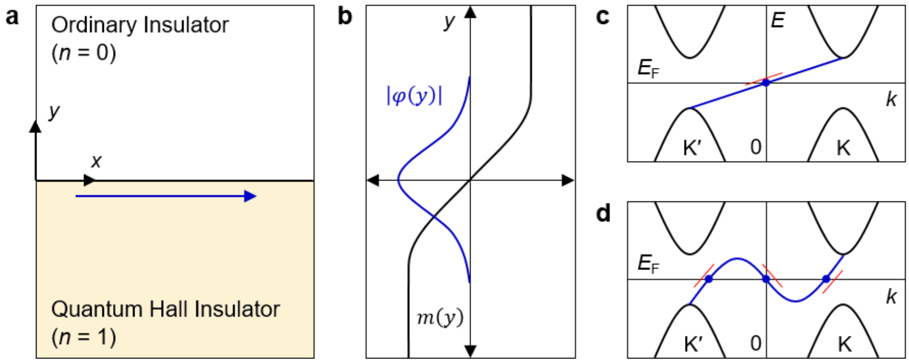

Figure 2.2 Bulk-boundary correspondence of the QHE. **a.** A chiral edge state in a semi-infinite plane. **b.** The interface between an ordinary insulator and QHI is associated with the sign change of *y*-dependent mass *m*(*y*). The *y*-direction plane wave solution gives the edge-localized state. **c.** Haldane's model describes the connection of conduction and valence band at distinct valleys by the chiral edge state of the semi-infinite QHI. **d.** The changed Hamiltonian makes the detail of the edge state change. However, the difference between right-moving (right-up red lines) and left-moving (right-down red lines) modes remains unchanged.

The gapless conducting edge state is a representative feature of the system with topologically non-trivial bands. The origin of such a peculiar state relies on the topological classification of the bulk bands. The explicit way of showing the effect of bulk topology on the edge mode is to apply the Jackiw Rebbi model[22]. Consider the *y*-dependent mass *m*(*y*) changes its sign at the Dirac point so that the 2D system has an insulating state with $\mathrm{m}(y) > 0$ and quantum Hall state with $\mathrm{m}(y) < 0$ ($\mathrm{m}'(y) = -\mathrm{m}(y) > 0$) while the system has translation symmetry along the *x* axis, as shown in Fig. 2.2a. By assuming the plane wave solution of the Dirac Hamiltonian $\psi_{q_x}(x, y) =$

$e^{\mathrm{i}q_x x}\varphi(y)$, the given 2D system of the interface between topologically distinct states can be simplified into a 1D Jackiw Rebbi problem that gives

$$\psi_{q_x}(x,y) \propto e^{\mathrm{i}q_x x} \exp\left(-\int_0^y dy' m(y') dy'/v_F\right)\begin{pmatrix}1\\1\end{pmatrix} \quad (2.4)$$

with the linear band dispersion $E(q_x) = \hbar v_F q_x$ which represents the chiral edge state[23]. Likewise, the Haldane model explanation of the infinite strip of QHI suggests a single chiral edge state connecting the valence band and conduction band at **K′** and **K** point, respectively (Fig. 2.2c). In Fig. 2.2c and d, the effect of smooth variation in the Hamiltonian is clearly visualized. While the chiral edge has only positive group velocity $dE/dq_x = \hbar v_F$ (right-moving mode) in the case shown in Fig. 2.2c, the changed Hamiltonian gives two right-moving edge modes ($N_\mathrm{R} = 2$) and one left-moving edge mode ($N_\mathrm{L} = 1$) at the intersection with the Fermi energy as shown in Fig. 2.2d. However, the difference $\Delta n = N_R - N_L = 1$ is conserved regardless of the detailed structure of the edge state. Here, Δn is identical to the Chern number difference across the interface between two states, and bulk-boundary correspondence stands for the role of bulk topology, which determines Δn and thus shapes the fundamental of the edge state.

2.1.4 Z_2 topological insulators

One essential assumption for the QHE is the violation of time-reversal symmetry that breaks the degeneracy at the Dirac point due to any kind of magnetic order. In contrast, the quantum spin Hall effect (QSHE) appears under the time-reversal symmetric condition in the system of spin 1/2 particles. The origin of QSHE can be summarized by the new mass term in the Dirac Hamiltonian related to the spin degree of freedom that leads to a band gap opening proportional to the spin-orbit coupling (SOC)[24]. The generalized Haldane model that includes spin-dependent hopping terms to consider the effect of SOC also can describe the QSHE. The resultant edge state of the quantum spin Hall insulator (QSHI) consists of a pair of two counter-propagating modes that is coupled with up and down spins.

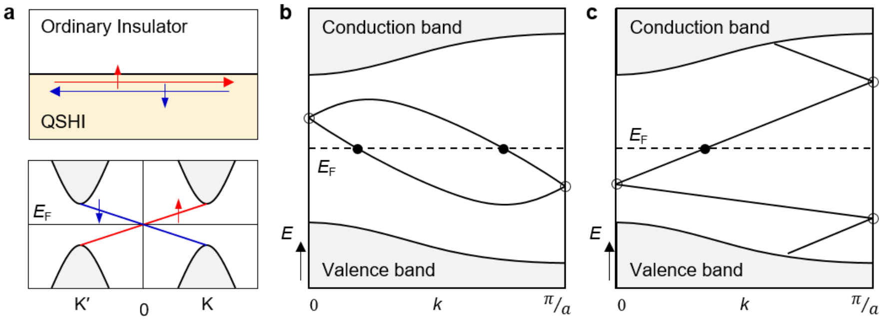

Figure 2.3 Haldane's model for QSHI and Kramers' degeneracy. **a**. The helical edge states are localized at the interface between a QSHI and an ordinary insulator. The intrinsic SOC is responsible for such spin-momentum-locked edge modes. **b.** Two Kramers degenerate points (empty circles) at the TRIM are connected pairwise with each other. The spin-split states between the TRIM intersect Fermi level E_F even number of times. **c.** When the degenerate points are connected, as shown in **c**, the spin-

split states intersect E_F odd number of times and cannot be eliminated. In **b** and **c**, only half of BZ is shown since the time-reversal symmetry guarantees the identity of the time-reversal pair in $-\boldsymbol{\pi}/\boldsymbol{a} < \boldsymbol{k} < \mathbf{0}$.

Figure 2.3a shows the real space spinful edge modes and Haldane model expression of a semi-infinite graphene strip that is a QSHI. The time-reversal pair of chiral modes form a helical edge state in QSHI. Thus a finite QSHI channel can have conducting channels at both edges so that the total conductivity is quantized with the unit conductivity of $\sigma = 2e^2/h$. Note that the QSHE is not reported in actual graphene due to the lack of SOC that generates a mass gap at the corner points of the BZ.

It is most important to understand how time-reversal symmetry works on the spin 1/2 particle to explain the band topology and corresponding bulk-boundary correspondence of the QSHI. The time-reversal symmetry can be expressed as a form of an anti-unitary operator acting on a Hilbert space

$$\Theta = e^{-\mathrm{i}\pi S_y}K, \quad (2.5)$$

where S_y is a spin operator and K is complex conjugation. Assume there is a time-reversal invariant Hamiltonian that has a non-degenerate state $|\chi\rangle$, so that

$$\Theta|\chi\rangle = c|\chi\rangle \quad (2.6)$$

for some constant c. Here, there is no solution for electron since Eq. (2.6) means

$$\Theta^2|\chi\rangle = |c|^2|\chi\rangle, \quad (2.7)$$

while $\Theta^2 = (-1)^{2S} = -1$ for electron, a spin S = 1/2 particle, but $|c|^2 \neq -1$ for any c. Therefore, any time-reversal symmetric system with S = 1/2 should have a time-reversal invariant Hamiltonian that is at least twofold degenerate. This constraint is called Kramers' degeneracy theorem. For a system with the Hamiltonian, which has in-gap edge states, the in-gap states should be twofold degenerated at the time-reversal invariant momenta (TRIM) for the spin up and down state. Regarding the spin-orbit interaction that splits the degeneracy at the momentum away from TRIMs, the degenerated state at TRIMs can be connected in two ways, as shown in Fig. 2.3b and c. In the case of a pairwise connection (Fig. 2.3b) where the edge modes intersect Fermi level E_F even number of times, the in-gap edge states can be removed by the smooth modulation of Hamiltonian through pushing the edge states out of the gap. On the contrary, the in-gap edge states cannot be removed by the similar modulation of Hamiltonian in the case shown in Fig. 2.3c, where the edge modes intersect E_F odd number of times. The difference between these two cases is characterized by the number of time-reversal pairs of intersections in total BZ N_K (note Fig. 2.3b,c shows only half of the BZ). Here, N_K is determined by the change in the topological invariant ν, which is called Z_2 invariant, across the interface between two bulk bands as

$$N_{\mathrm{K}} = \Delta\nu \mod 2, \quad (2.8)$$

defining the bulk-boundary correspondence for QSHI.

There are various ways to calculate the Z_2 invariant according to the symmetry of the given system, while it can be generally computed from the occupied Bloch functions. For example, the Z_2 invariant of a 2D system with conserved perpendicular spin *Sz* can be considered to have an independent Chern number for each of the up and down spin modes so that the quantized spin Hall conductivity is defined by the difference in the number of counter-propagating spin-up and -down modes as

$$\nu = \frac{|n_{\uparrow} - n_{\downarrow}|}{2} \mod 2, \quad (2.9)$$

while the time-reversal symmetry requires $n_{\uparrow} + n_{\downarrow} = 0$. When the crystal has inversion symmetry, ν can be computed even simpler by obtaining the parity eigenvalue at the special points in the BZ.

The Z_2 topology found in condensed matter systems is often represented by the strong SOC of the given system and topologically non-trivial band inversion, which induces negative Dirac mass. The inversion of the conduction and valence band was first achieved by manipulating the thickness of the HgTe/CdTe quantum well[25], and over the following decade, numerous 2D and 3D TIs derived from HgTe quantum well[25], narrow gap semiconductors[26], and *p* orbital related Bi_2Se_3 family[27].

2.1.5 Higher-order topological insulators

The boundary states of QHI or QSHI host peculiar characteristics that are protected by the bulk band topology through the bulk-boundary correspondence. Further from the 2D problems discussed earlier, the concept of topologically protected boundary states can also be applied to general *d*-dimensional systems. There, the topological distinction between two *d*-dimensional bulk states requires (*d*-1)-dimensional boundary to be gapless and its degeneracy protected by the bulk-boundary correspondence. Beyond this paradigm, Benalcazar, Bernevig, and Hughes suggested the generalization of bulk-boundary correspondence that supports (*d*-*n*)-dimensional gapless boundary mode that is protected by the topology of the *d*-dimensional bulk of the *n*th-order TI[28,29]. Starting from the four-band model with an anti-unitary term for combined symmetry, chiral and helical HOTIs were predicted, and the new topological classifications, e.g., ZxZ, Z_2xZ_2, and Z_4, are proposed based on various combinations of symmetries. Compared to the topological band gap inversion found in the Z_2 TIs, the phenomenological origin of the higher-order topology can be represented by the strong SOC and doubly band inversion associated with four low energy bands. So far, the band structure and corresponding topological features of HOTIs have been predicted by well-established methods such as a multi-orbital tight-binding model, first principle calculation, and Wilson loop calculation[28-31]. So far, only a few materials e.g., bismuth[32,33], SnTe[28,34], and twisted bilayer graphene[35] were predicted to have higher-order band topology,

2.2 Anomalous Hall effect

2.2.1 Introduction

The Hall effect describes the charge carrier transport transverse to the bias electric field that is caused by the Lorentz force from the external magnetic field. The anomalous Hall effect (AHE) was first reported not long after the discovery of the Hall effect as an abnormal increase of transversal current in ferromagnetic metals. While the Hall effect could be explained by classical electromagnetics, the description of AHE remained unresolved until the concept of geometric phase and band topology was formalized recently.

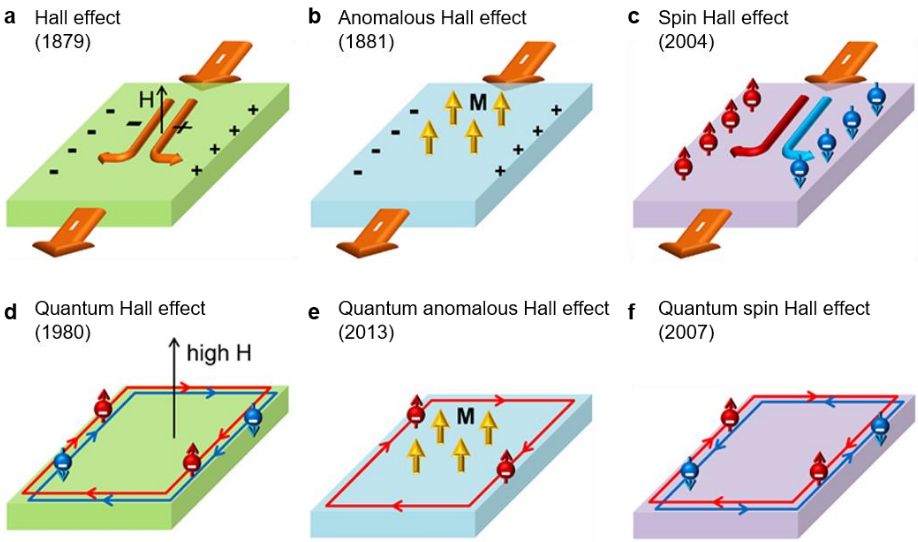

Figure 2.4 Schematic diagrams describing the Hall effect family. From the discovery of the Hall effect based on classical electromagnetism, Hall effects with time-reversal symmetry, spin-degree of freedom, and band-topology-related phenomena were discovered. The figures are adopted from Ref. 36

The AHE is now explained as a combination of intrinsic Hall conduction generated by the SOC under broken time-reversal symmetry and scattering-involved extrinsic conduction based on the quantum mechanical transport theory. Moreover, the spin Hall effect (SHE), a generation of spin currents in a direction transverse to electrical currents, is explicated by similar mechanisms as a spinful form of AHE. With the augmented understanding of the topological aspect in Hall transport regimes, we now have a complete family of Hall effects shown in Fig. 2.4 that includes the topologically protected quantum-version of Hall effects[36].

2.2.2 Intrinsic contribution

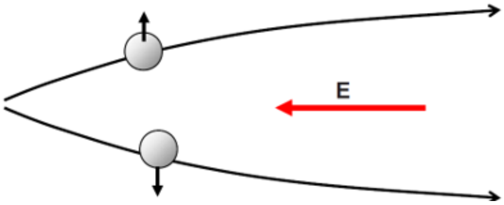

Figure 2.5 Schematic diagram describing the intrinsic contribution of AHE. The Berry curvature distribution of the system decides the carrier transport transverse to the external electric field while the time-reversal symmetry is conserved. The figure is adapted from Ref. 5

The intrinsic component of AHE is decided by the band structure of the crystal only, as its name suggests. This contribution σ_{ij}^{int} can be explicitly calculated from the Kubo formula for given Bloch Hamiltonian H with the eigenstates $|n,k\rangle$ and corresponding eigenvalues $\varepsilon_n(k)$ as

$$\sigma_{ij}^{int} = e^2\hbar \sum_{n\neq n'} \int \frac{d\boldsymbol{k}}{(2\pi)^d} \left[f\left(\varepsilon_n(\boldsymbol{k})\right) - f\left(\varepsilon_{n'}(\boldsymbol{k})\right)\right] \times$$

$$\mathrm{Im}\frac{\langle n,\boldsymbol{k}|v_i(\boldsymbol{k})|n',\boldsymbol{k}\rangle\langle n',\boldsymbol{k}|v_j(\boldsymbol{k})|n,\boldsymbol{k}\rangle}{[\varepsilon_n(\boldsymbol{k})-\varepsilon_{n'}(\boldsymbol{k})]^2}, \quad (2.8)$$

where the velocity operator $v(\boldsymbol{k}) = \frac{1}{i\hbar}[r, H(\boldsymbol{k})] = \frac{1}{\hbar}\nabla_{\boldsymbol{k}} H(\boldsymbol{k})$ relates σ_{ij}^{int} with the band topology. Such a relationship can be derived from

$$\langle n, \boldsymbol{k} | \nabla_{\boldsymbol{k}} | n', \boldsymbol{k} \rangle = \frac{\langle n, \boldsymbol{k} | \nabla_{\boldsymbol{k}} H(\boldsymbol{k}) | n', \boldsymbol{k} \rangle}{\varepsilon_{n'}(\boldsymbol{k}) - \varepsilon_n(\boldsymbol{k})}, \quad (2.9)$$

thus Eq. (2.8) can be reduced to

$$\sigma_{ij}^{int} = -\varepsilon_{ijl} \frac{e^2}{\hbar} \sum_n \int \frac{d\boldsymbol{k}}{(2\pi)^d} f\big(\varepsilon_n(\boldsymbol{k})\big) \Omega_n^l(\boldsymbol{k}) \quad (2.10)$$

where $\Omega_n^l(k)$ is the Berry curvature $\Omega_n^l(k) = \nabla_k \times A_n(k)$ defined by Berry potential $A_n(k) = i\langle n, k | \nabla_k | n, k \rangle$ and ε_{ijl} is the antisymmetric tensor. Note that the semi-classical transport theory based on the equation of motion of Bloch state wave packets can draw the same transport contribution[37].

2.2.3 Skew-scattering and side-jump contribution

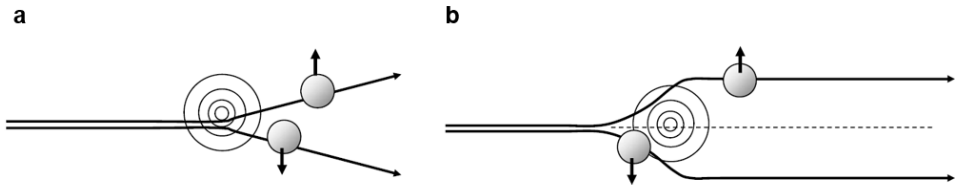

Figure 2.6 Schematic diagram describing the skew scattering (**a**) and side jump (**b**) contribution of AHE. The figure is adapted from Ref. 5

The most distinctive feature of the skew-scattering contribution compared to other contributions is its dependence on transport lifetime τ. The origin of skew-scattering can be summarized as a chiral scattering from the disorder affected by SOC. The transition due to the perturbation V is represented by the transition probability $W_{n \to n'}$ using Fermi's golden-rule as

$$W_{n \to n'} = \frac{2\pi}{\hbar} |\langle n|V|n'\rangle|^2 \delta(E_n - E_{n'}). \quad (2.11)$$

Generally, the transition probability $W_{n \to n'}$ is considered to be identical to $W_{n' \to n}$. However, in the presence of SOC, asymmetric chiral perturbations appear on the third-order term of the scattering rate in the power of the disorder strength[38]. The effect of chiral perturbation can be modeled with the asymmetric part of the transition probability

$$W_{kk'}^{A} = -\tau_A^{-1} \boldsymbol{k} \times \boldsymbol{k}' \cdot \boldsymbol{M}_s \quad (2.12)$$

that differentiates $W_{n \to n'}$ from $W_{n' \to n}$. In other words, disorder scattering in a spin-orbit coupled and magnetized environment is biased to the left or right side according to the magnetization and spin of the carrier. Therefore, the skew-scattering contribution to the anomalous Hall conductivity is approximately proportional to the transport lifetime.

The side-jump contribution to AHE is generated by the transverse displacement of a wave packet during the scattering from the impurity that has SOC. This can be modeled as a Gaussian wave packet scattered by a spherical potential well, while the SOC term $H_{\mathrm{SO}} = (1/2m^2c^2)(r^{-1}\,\partial V/\partial r)S_z L_z$ is in presence. The resultant displacement is $\Delta y = \frac{1}{6} k \lambda_c^2$ to the direction transverse to the wave vector k with $\lambda_c = \hbar/mc$ is the Compton wavelength[39]. With this argument rely on semiclassical Boltzmann transport theory, the side-jump contribution is described to be independent of τ, similar to the intrinsic contribution. Note that this model deals with the non-SOC part of the wave packet scattering in a weak SOC limit. In crystals with strong SOC, the contribution from the SOC part of the wave packet scattered by the scalar potential without SOC should be considered[40]. However, this so-called "intrinsic" side-jump contribution is also independent of τ, sharing the generic characteristics of the "extrinsic" side-jump contribution. Therefore, the side-jump contribution is often estimated by calculating τ-independent component remaining after excluding the intrinsic and skew-scattering contribution since the latter two contributions are relatively easy to identify based on the theoretical computation and τ-dependence, respectively.

2.2.4 Spin Hall effect

The SHE stems from the concept of AHE, while the spin current t0ransverse to the charge current is induced in the non-magnetic material by SHE. Similar to the AHE, the microscopic origin of SHE is characterized by three conductivity contributions; intrinsic, skew-scattering, and side-jump.

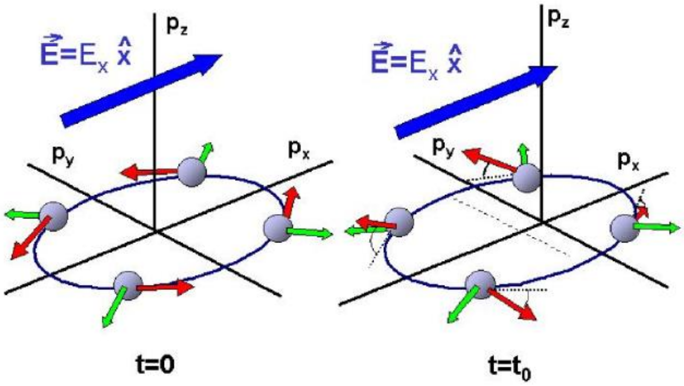

Figure 2.7 Schematic diagram explaining the intrinsic contribution of SHE. The figure is adapted from Ref. 41.

The intrinsic contribution can be illustrated semi-classically using the Kubo formula, as intrinsic AHE was described by the identical formula earlier in Sec. 2.2.2. In terms of physical meaning, the intrinsic contribution is derived by the spin precession of the Bloch electrons under the momentum-dependent magnetic field induced in the perfect crystal while they are accelerated by the external electric field[41] (Fig. 2.7). The skew-scattering and side-jump contribution are valid for the SHE, in both weak and strong SOC regime with slightly different microscopic mechanism considering the amplitude of spin-dependent splitting of the bands[42].

Because the pure spin current does not necessarily involve the carrier transport alongside the spin transport, spin-sensitive detection methods such as optical probing of spin polarization or electrical probing using ferromagnetic contacts should be used to observe the SHE experimentally.

One of the earlier studies used the magneto-optical Faraday or Kerr effect to detect the SHE-induced spin accumulation at the side edge of the semiconductor channel[43]. The inverse SHE, the generation of charge current derived by the spin current in a spin-orbit coupled system, was adopted for the electrical detection of both optically and electrically induced SHE[44,45]. In addition, the direct detection of spin using the non-local spin valve device made of ferromagnetic metal contact is widely used based on the Hanle spin precession[46-48].

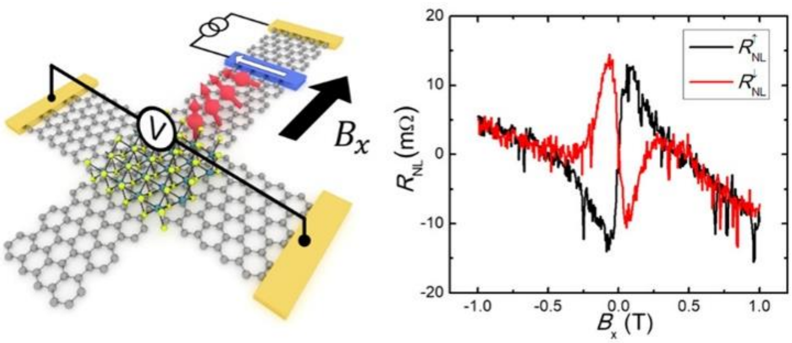

Figure 2.8 Electrical measurement of the SHE induced in graphene/MoS_2 van der Waals heterostructure. The figure is adapted from Ref. 48.

Recently, the surge of interest in 2D materials such as graphene and transition metal dichalcogenides (TMDs) influenced the study of AHE and SHE. Especially in TMDs, the presence of valley pseudospin suggests the Hall effect related to the valley degree-of-freedom, namely the valley Hall effect (VHE) that will be discussed in Section 3.

2.3 Magneto-optical Kerr effect

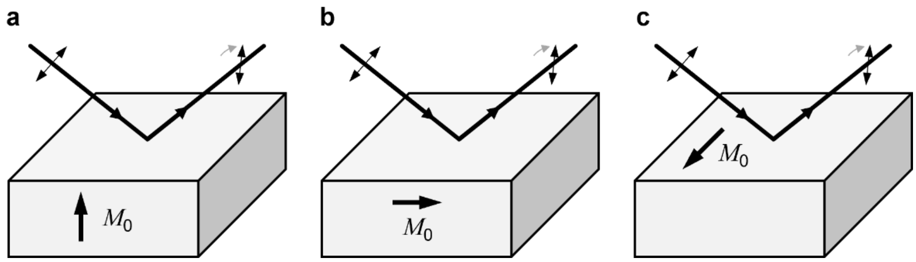

Figure 2.9 Three distinct configurations of the magneto-optical Kerr effect; **a.** Polar Kerr effect, **b.** longitudinal Kerr effect, and **c.** Transverse Kerr effect. The orientation of magnetization is normal to the reflecting surface in the polar Kerr effect regime (**a**). The orientation of magnetization is in both the reflecting surface plane and the plane of incidence in the longitudinal Kerr effect regime (**b**). The orientation of magnetization is in the reflecting surface but normal to the plane of incidence in the transverse Kerr effect regime (**c**).

The magneto-optical Kerr effect (MOKE) is one of the light-matter interactions caused by the magneto-optical characteristics of the material. When the linearly polarized light is injected into a target material with the magnetization M_0, the reflected light polarization gains ellipticity ε_K and rotates by the Kerr rotation angle θ_K. The MOKE can be classified into three distinct configurations; polar Kerr effect, longitudinal Kerr effect, and transverse Kerr effect, with respect to the relative orientation of M_0 and the plane of incidence (Fig. 2.9). All three regimes can be expressed in terms of 2 x 2 reflection coefficient tensor for TE and TM polarizations, while the off-diagonal components are proportional to the first-order effect of M_0 and their phases are different from those of diagonal components. In this dissertation, only the polar MOKE will be discussed since it can be modeled more simply and used in optical experiments.

An electromagnetic wave propagating in the –z-direction with the polarization of the x-direction can be expressed as

$$E_i(z,t) = \hat{x}\mathcal{E}\exp(-\mathrm{i}kz - \mathrm{i}\omega t) = \frac{\mathcal{E}}{\sqrt{2}}(\hat{e}_+ + \hat{e}_-)\exp(-\mathrm{i}kz - \mathrm{i}\omega t), \quad (2.13)$$

by using normal modes $\hat{e}_\pm = \frac{1}{\sqrt{2}}(\hat{x} \pm \mathrm{i}\hat{y})$ that are complex eigenvectors denoting left- and right-circularly polarized unit vectors. Here, both eigenvectors have propagation constant k. The reflection of normal modes is expressed by distinct and independent reflection coefficients $r_\pm = (1-n_\pm)/(1+n_\pm)$ for $\hat{e}_\pm$. The refraction indices $n_\pm$ are defined as

$$n_\pm = \sqrt{n_\perp^2 \mp \xi}, \quad (2.14)$$

while ξ is the parameter for the first-order effect of magnetization ($\xi \propto M_0$) and $n_\perp^2$ is one of the parameters for the second-order effect on the dielectric permittivity tensor ($n_\perp^2 \propto M_0^2$)(Appendix A). After the reflection, the reflected wave is described by

$$\begin{aligned} E_r(z,t) &= \hat{e}_+ r_+ \mathcal{E}_+ \exp(ikz - i\omega t) + \hat{e}_- r_- \mathcal{E}_- \exp(ikz - i\omega t) \\ &= \frac{\mathcal{E}}{\sqrt{2}} (\hat{e}_+ r_+ + \hat{e}_- r_-) \exp(ikz - i\omega t) \\ &= \frac{\mathcal{E}}{2} [\hat{x}(r_+ + r_-) + i\hat{y}(r_+ - r_-)] \exp(ikz - i\omega t) \end{aligned}$$

(2.15)

with the modified polarization

$$\tan A e^{i\varphi} = i\frac{r_+ - r_-}{r_+ + r_-}. \quad (2.16)$$

In general, $|r_+ - r_-| \ll |r_+ + r_-|$ for practical magnetic materials, thus the polarization can be approximated as

$$\tan A e^{i\varphi} \approx A e^{i\varphi} \approx \theta_K + i\epsilon_K, \quad (2.17)$$

while θ_K is the Kerr rotation angle and ϵ_K is the Kerr ellipticity. As a result, θ_K and ϵ_K are given by

$$\theta_{\mathrm{K}} = \mathrm{Im}\left[\frac{\xi}{n_\perp(n_\perp^2 - 1)}\right], \qquad \epsilon_{\mathrm{K}} = -\mathrm{Re}\left[\frac{\xi}{n_\perp(n_\perp^2 - 1)}\right], \quad (2.18)$$

respectively. To summarize, the polarization of the linearly polarized light rotates during the reflection from a magnetic material, and the magnetic circular dichroism is responsible for such rotation (Kerr rotation, θ_{K}). In some cases, the magnetic birefringence also induces the elliptic component (Kerr ellipticity, ϵ_{K}).

The MOKE is a useful tool for the observation of the intrinsic magnetization and the magnetic moment induced in the target material. One practical application is Kerr microscopy, which can resolve the magnetic domains and their magnetization in the magnetic material. Another valuable way of using MOKE is to measure the spin polarization induced in non-magnetic materials. Compared to the method of analyzing the polarization of photoluminescence, MOKE measurement has the advantage that it can be applied to experiments on gapless materials or materials with an indirect band gap. Moreover, since MOKE is an instantaneous phenomenon, it can also be used to observe the dynamic characteristics of the sample when combined with ultrafast pulse lasers. This so-called time-resolved Kerr rotation measurement is widely used in studies on spin-valley dynamics in TMDs and spin dynamics in topological states[49-51]. The generic design of the optical system for Kerr rotation measurement is shown in Fig. 2.10.

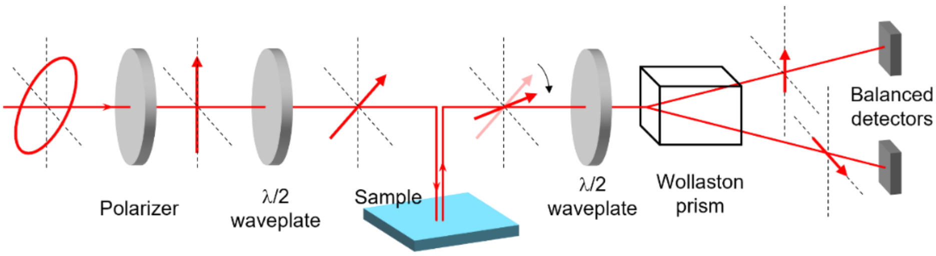

Figure 2.10 Schematic diagram of a basic experimental system for Kerr rotation measurement. The polarizer and $\lambda/2$ waveplate can be replaced with a single polarizer in some cases.

First, the initial linear polarization of the incident light is set by a linear polarizer and optional waveplate. The rotation of light polarization is then obtained by using a Wollaston prism and balanced detector, which separates and measures the *s* and *p* polarization components of the reflected light. Here, note there is a $\lambda/2$ waveplate between the sample and Wollaston prism. This waveplate is used for the zeroing of the balanced detector before placing the beam spot at the sample. The spatially and temporally resolved Kerr rotation measurement system I built, introduced in the next section, also includes this configuration.

2.4 Experimental setup and device fabrication

2.4.1 Ultrafast pulse laser system

An ultrafast pulse laser system based on Ti:Sapphire crystal was used for the time-resolved experiments introduced in this dissertation. The system is composed of three major parts; an oscillator, an amplifier, and a pulse duration modulator. In the oscillator (Micra/Verdi, Coherent), $Nd:YVO_4$ diode laser generates a continuous-wave (CW) 532 nm pump that seeds Z-cavity that has a Ti:Sapphire as a gain medium. Here, weak pulses with a center wavelength of 800 nm and a repetition rate of 80 MHz are generated by using the Kerr lens mode locking technique. Then the pulse duration is extended by the stretcher grating in the pulse duration modulator (stretcher/compressor, Coherent) to prevent unintentional nonlinear effects or damage of optics during the amplification. After the stretching, the initial pulse goes through regenerative Ti:Sapphire amplification pumped by a 532 nm CW laser in the amplifier (Reg A, Coherent). The Q-switching and cavity dumping methods are used to make high-power pulses with a center wavelength of 800 nm and a repetition rate of 250 kHz. Finally, the pulse duration is compressed by the compressor grating in the pulse duration modulator to form a 50-fs pulse that would be used for the ultrafast time-resolved experiments.

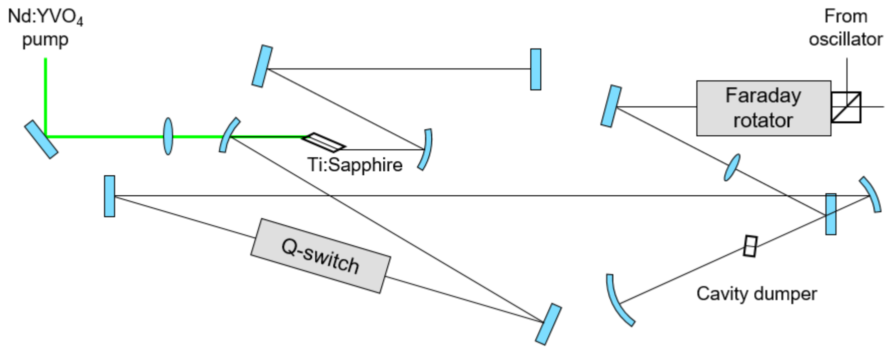

Figure 2.11 A schematic describing the Ti:Sapphire regenerative amplifier.

There are several techniques that can be used to modulate the wavelength of the ultrafast pulse for optical experiments on a wider range of target systems. The second harmonic generation (SHG) and white-light generation (WLG) are typical examples of this modulation technique that can easily obtain frequency-doubled pulse and broadband continuum pulse, respectively. A nonlinear crystal such as beta-barium borate (β-Ba(Bo$_2$)$_2$, BBO) is generally used to generate photons with doubled energy from the incident photons. The WLG, however, is rather a general phenomenon that appears in various types of materials (crystals, gases, liquids etc.) due to the self-phase modulation with self-steepening by the self-focusing of short, intense pulse laser. The spectral broadening is achieved by the combination of these nonlinear optical effects while the pulse duration is not conserved. For the WLG used in the experiments covered in this dissertation, a compressed 50-fs, 800-nm pulse was focused at a 2-mm-thick sapphire disk to generate the stable super-continuum. More advanced ways of wavelength modulation, such as optical parametric amplification and differential frequency generation, are also available but will not be discussed in detail in this dissertation.

2.4.2 Multi-role microscopy system

The majority of spatially and temporally resolved optical experiments discussed in this dissertation was performed under stable cryogenic condition. An optical cryostat with a microscope imaging system that is coupled with the multiple pulse laser alignment is essential for such experiments, and the electrical access to the sample device is also vital for the electrical measurements. In order to design a single experimental setup that is compatible with all the optical experiments that need to be performed over one sample, I built a multi-role microscopy system based on the manufactured optical microscope frame (BX51WI Olympus).

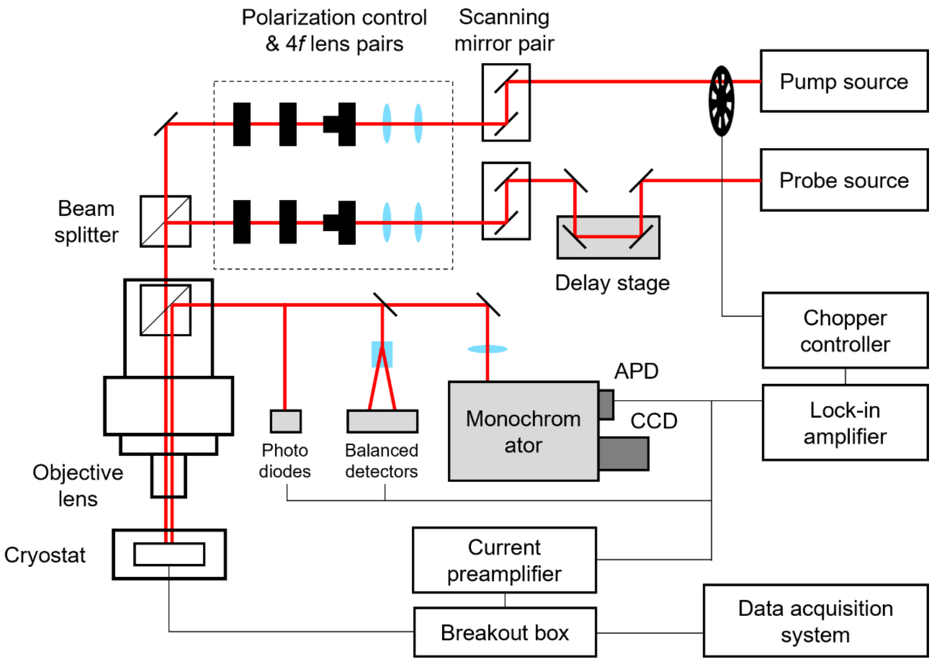

Figure 2.12 Schematic diagram of the home-built multi-role microscopy system. All possible variations of the setup are shown at once.

Two input laser beams can be used simultaneously, and the motorized delay stage (M-IMS300PP, Newport) controlled by a motion controller (ESP301, Newport) is placed on one of the input paths for the ultrafast time-resolved experiments. All available light sources, including CW supercontinuum, diode lasers, and wavelength-modulated pulse lasers from Ti:Sapphire amplifier, were compatible with both input beam paths. Scanning mirrors (GVS012/M, Thorlabs) and 4*f*-lens pairs were placed for proper 2D scanning of the incident beam at the sample position. The polarization optics suitable for each experiment were placed after the scanning mirror and lens pairs to manipulate the light polarization. Here, both manual (RSP1/M, Thorlabs) and motorized (PR50CC, Newport) rotation mounts were used for precise polarization control. The two input beam paths were combined with the beamsplitter outside the microscope and delivered to the objective lens by a beamsplitter inside the microscope, while all the beamsplitters can easily be replaced by dichroic filters or mirrors as occasion demands. The delivered beams were focused on the sample inside the cryostat by the objective lens, and the same objective lens collected the light reflected or radiated from the sample and delivered them to the optical detection part of the setup.

The light containing the signal from the device was separated by the beamsplitter or dichroic filter inside the microscope. Then, depending on the type of experiment, the signal was put into the monochromator (MonoRa320i, Dongwoo Optron) for spectroscopy or put directly into the detectors. The monochromator was used with a charge-coupled device (CCD) to take the snapshot of the spectrum (iKon-M934, Andor) and an avalanche photodetector (APD, APD410A/M, Thorlabs) for spectral scanning of the signal. Wollaston prism (WP10, Thorlabs) and balanced detector (NIRvana2008 and NIRvana2018, Newport) were used for the Kerr rotation measurements. The data were acquired by a lock-in amplifier (SR850, Stanford Instruments) connected to the detectors. For the lock-in amplifier technique, the probe beam was modulated by the mechanical chopper which is coupled to the lock-in amplifier through the chopper controller (310CD, Scitec Instruments). As a result, the photoluminescence (PL) spectroscopy, reflection (absorption) spectroscopy, SHG measurement, MOKE measurement, and the time-resolved variant of those experiments can be performed with a spatial resolution of ~ 1 μm using the single microscopy system.

In addition to the optical measurements, the electrical characteristics of the sample device can also be measured by using the electrical access embedded in the optical cryostat (Microstat Hires, Oxford). I designed a printed circuit board for the connection between the embedded electric output port and the device using the In wire. The electrical output port of the cryostat is connected to the shielded breakout box with switches for each channel. Electrical characteristics were measured by source measure unit (2450, Keithley) and data acquisition system (DAQ, National Instruments), while the electrical circuit for the measurement is designed to maintain closed and have floating ground to prevent catastrophic external influence. All the chassis and shell ground is connected to the external ground to provide proper electromagnetic shielding. Photocurrent measurements are also available by using a current preamplifier (SR560, Stanford Instruments) and the lock-in amplifier coupled with the optical chopper controller.

2.4.3 Van der Waals heterostructure device fabrication

The devices used in experiments were composed of van der Waals stacking of 2D materials. The single crystals of all TMD, TI, and hexagonal boron nitride (hBN) were stored and handled in the glovebox (N_2-filled, O_2 and H_2O less than 0.5 ppm) to avoid degradation. 2D flakes were mechanically exfoliated from the source crystal to diced and cleaned Si/SiO_2 wafer. 2D flakes were picked up and transferred onto the pre-patterned metal electrodes, including the gate electrode, to make a heterostructure device with electrical contacts according to the following procedure.

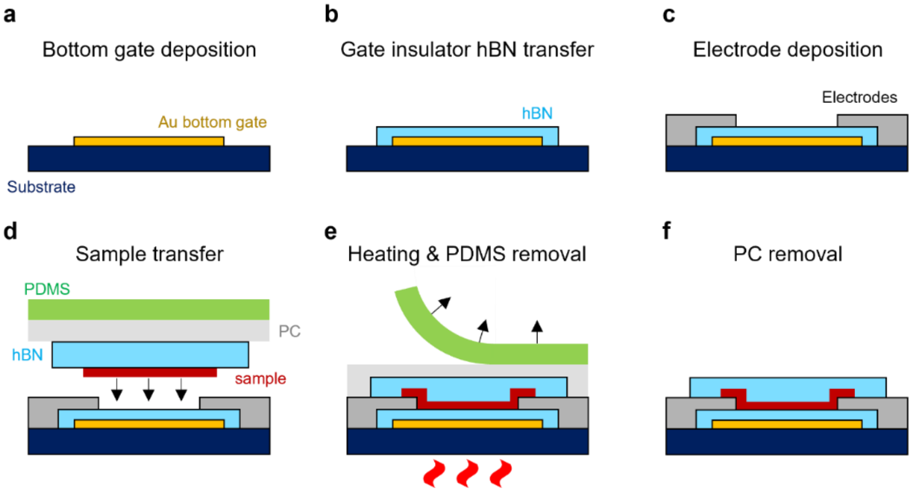

Figure 2.13 Schematic diagrams showing the van der Waals sample transfer.

1. The gate electrode is deposited on Si/SiO_2 wafer using the electron beam lithography and thermal evaporation of the metal.
2. The gate insulator hBN flake is transferred onto the gate electrode using polydimethylsiloxane (PDMS) viscoelastic stamping.
3. Metal contacts are deposited using electron beam lithography and thermal evaporation.
4. Put a piece of PDMS on a slide glass and cover it with Poly(bisphenol A carbonate) (PC) film.
5. Pick up an hBN flake with PC/PDMS while heating to 343 K (0.5 K/s).
6. Pick up a 2D flake to transfer with the hBN on PC/PDMS.
7. Repeat procedure 6 to pick up additional 2D flakes.

8. Put picked-up flakes on the pre-patterned electrodes and heat to 455 K (0.5 K/s).
9. Wait until the PC attached to the wafer is heated and melted.
10. Remove the PDMS slowly.
11. Dissolve the PC remaining on the wafer.

The device fabricated through these procedures is encapsulated by top hBN, and the sample 2D flake is not contaminated by any chemical so that the quality of the complete device is well preserved. Note that chemical cleaning (H_2O, acetone, isopropanol) and thermal annealing (10 hours at 473 K in Ar flow of 200 ccm and H_2 flow of 50 ccm) proceeded after the metal deposition and bottom hBN transfer to clean the exposed surface.

For the precise sample transfer inside the glovebox, I built a motorized transfer system equipped with a hot chuck, a motorized rotation stage (PRMTZ8/M, Thorlabs), a piezo-electric stage (MAX311D/M, Thorlabs), and a motorized stage (PLS-XY, Thorlabs).

CHAPTER 3 – NON-EXCITONIC VALLEY HALL EFFECT

3.1 Introduction

Monolayer TMDs have valley-contrasting Berry curvature due to the broken inversion symmetry. Along with the strong spin-orbit coupling, the non-zero Berry curvature at the valleys generates a valley pseudospin current transverse to the external electric field[37,52,53]. This phenomenon, called the valley Hall effect (VHE), was first predicted in the graphene with broken inversion symmetry[54] and was observed in monolayer MoS_2[55], gapped[56], and bilayer graphene[57]. Experimentally, the finite orbital moment readily facilitates optical means to activate the VHE by using circularly-polarized photons (σ^+ or σ^-) near the TMD bandgap[55,58-60]. As such, direct optical excitation has been one routine and yet convenient way of accessing the VHE and the associated transport phenomena.

However, the optically generated valley-polarized excitons are short-lasting, typically in tens of picoseconds (ps), posing great challenges in valleytronic applications. Microscopically, the intervalley exciton exchange process (Maialle-Silva-Sham exchange) significantly subdues the valley polarization lifetime[61,62]. Recent works proposed the use of type II van der Waals heterostructures in which non-excitonic unipolar carriers to overcome the issue caused by excitonic interaction, i.e., either electrons or holes, were used[63,64]. By suppressing the Maialle-Silva-Sham exchange pathway, the valley pseudospin is observed to have a much longer lifetime. Besides, the electrically-driven VHE without light excitation was also demonstrated[65], but further understanding of the origin of the VHE or dynamic property of valley Hall transport has not been clearly explained.

Here, an optical demonstration of non-excitonic VHE for time-resolved investigation using the van der Waals heterostructure is reported. The approach used in this study is to inject the spin-polarized electrons in a partially stacked vertical heterobilayer that consists of MoS_2 and WTe_2 monolayers. The VHE is solely driven by electrons, thereby long-lived VHE lasts a few nanoseconds, and the 20-fold increase of valley Hall mobility compared to the exciton-based VHE was observed by performing the temporally and spatially resolved PL and Kerr rotation microscopy[55,59,63]. Furthermore, we show that the non-excitonic VHE is deeply rooted in the Berry curvature of the occupied conduction electrons, whereby we obtained a good agreement on the gate-dependent depolarization time between the theoretical estimation of intrinsic VHE contribution and the ultrafast Kerr rotation data.

3.2 Experiments

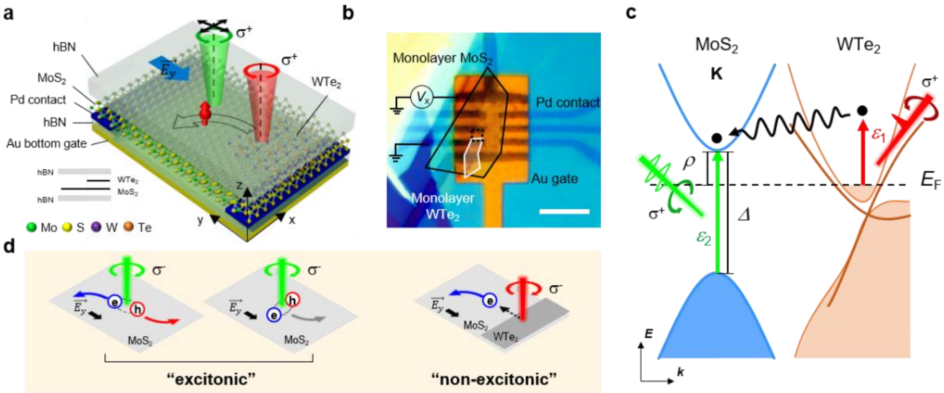

Figure 3.1 The non-excitonic valley Hall effect **a.** The schematic diagram of the heterobilayer device and the remote optical measurements are shown. Under the longitudinal electrical bias $\overrightarrow{E_y}$ between Pd electrodes (dark blue), the spin-polarized electrons are selectively excited by the circularly polarized (σ^+ in the figure) 50 fs 1.55 eV short pulse (red beam), and the VHE (black arrow) is observed by another laser (green beam). **b.** An optical microscope image of the heterobilayer device (device #1) is shown. The monolayer MoS_2 and WTe_2 are marked with the black and the white line, respectively. The dashed black line shows the spatial region where the 2D scanning experiments were performed. The longitudinal field is applied by the bias voltage V_x. The scale bar (white) is 10 μm. **c.** A schematic energy diagram of the MoS_2 (blue) / WTe_2 (orange) heterobilayer. The short-pulse light excitation with energy ε_1 (red) below the bandgap of MoS_2 (Δ) selectively excites the spin-polarized electrons in WTe_2

(black dots). Another light excitation with energy ε_2 (green) is applied to observe the effect of the injected electrons. **d.** The excitonic VHE involves both the unbound (left) and the bound (right) electron-hole pairs. The non-excitonic VHE is unipolar – without exciton formation or dissociation. All measurements were performed at a liquid nitrogen temperature of 78 K.

Figure 3.1 describes the schematics of our experiment and an optical microscope image of a device. The energy band diagram is shown in Fig. 3.1c. Because the 1D edge states in 2D TI have out-of-plane spin orientation[66,67], the monolayer 1T´-WTe_2 acts as a source of the spin-polarized electrons. Therefore, by injecting circularly polarized 50-fs pulses with photon energy ε_1 of 1.55 eV, electrons with a specific spin orientation were prepared at the junction between MoS_2 and the edge of WTe_2. Then, the transverse valley transport of VHE was generated by applying a longitudinal electric field across MoS_2. The Fermi level is tuned to be located within the MoS_2 bandgap (Δ) such that the optical excitation by the ultra-short pump pulse takes place only in WTe_2, not in MoS_2, i.e., $\rho < \varepsilon_1 < \Delta$; since the short-pulse pump excitation (remote pump) is spatially separated from the valley Hall transport region.

Figure 3.1d explains the difference between excitonic and non-excitonic VHE. Compared to the excitonic VHE, which involves the generation, dissociation, intervalley exchange of excitons[55], and the transverse transport of exciton itself[68], the non-excitonic VHE is based on the unipolar charge transport (thus termed non-excitonic), and the transverse valley Hall occurs in the MoS_2 layer with electrons (or holes) only. The non-excitonic VHE in MoS_2 was investigated by two independent measurements. First, the transverse VHE was confirmed by spatially resolved PL measurements. Second, the time-resolved Kerr rotation (TRKR) microscopy was performed with varying the Fermi level of the heterobilayer. While the former provides the conventional transverse Hall characteristics in a static limit[59-64], the latter enables to probe the dynamic features that were previously uninvestigated.

3.2.1 Sample preparation

The single crystals of MoS_2 and WTe_2 (HQ grapheneTM) and the high-quality hexagonal boron nitride (hBN) were used to obtain the atomically thin MoS_2, WTe_2, and hBN films by mechanical exfoliation, respectively. The hBN crystals were directly imported from the National Institute of Materials Science (NIMS), Japan. The thin hBN flake exfoliated from the single crystal was used to encapsulate the whole device. The MoS_2 and WTe_2 monolayer flakes were isolated from the bulk crystal on polydimethylsiloxane (PDMS) by using thermal released tape. The exfoliated monolayer flakes were then transferred onto the substrate with pre-patterned electrodes.

The Au bottom gate is used to induce a large electrostatic potential in the MoS_2-WTe_2 channel. For the device fabrication, the bottom gate electrode is patterned on a Si/SiO_2 substrate by the standard electron beam lithography, followed by the thermal evaporation of Ti (5nm) and Au (110nm). A thin hBN (15 nm) flake was used as a gate insulator, which was transferred using the PDMS stamping method. The 5 nm thick Pd electrodes were then deposited onto the gate insulator to apply the electrical bias along the longitudinal direction. Using a thin film of polycarbonate (PC, Sigma Aldrich, 6% dissolved in 1.0% ethanol stabilized chloroform, Sigma Aldrich), we sequentially picked up the hBN layer (20 nm), monolayer MoS_2, and monolayer WTe_2. The stacked heterostructure was transferred onto the pre-patterned electrodes. During the ‘pick up and transfer’ process, a stepping piezo-electric stage was used to stack layers with a speed of 50 nm/s. The fabrication process was performed in an inert atmosphere provided by a nitrogen-filled glove box to prevent the degradation of WTe_2 from the oxygen and the water vapor.

Finally, the completed device was sent to the post-annealing process (200 ℃ for 10 hours under an Ar flow of 200 ccm and H_2 flow of 50 ccm) to eliminate any organic residues and to achieve sufficiently good interfacial contact. The electrical characteristics of the complete device are shown in Fig. 3.2.

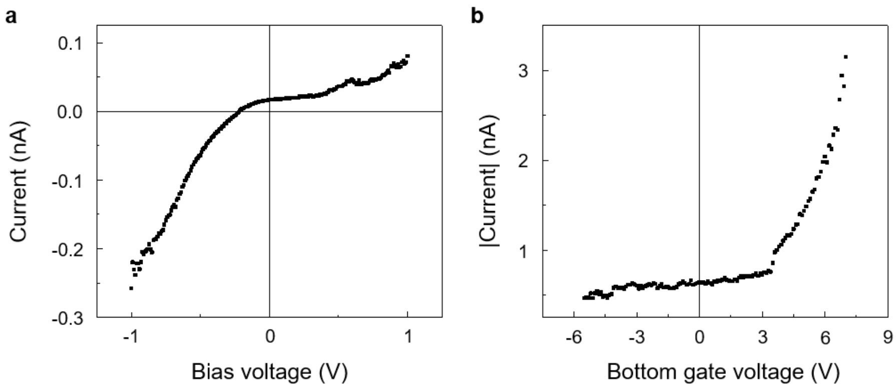

Figure 3.2 Transport characteristics of the complete device. a. Current-voltage output curve along the source and drain. b. Current along the source and drain with varying bottom gate voltage.

3.2.2 Spatially-resolved differential photoluminescence

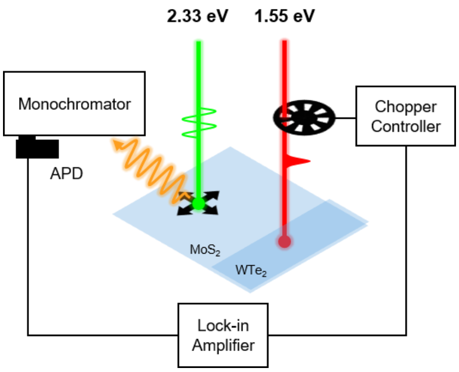

Figure 3.3 A schematic diagram of the spatially resolved differential PL measurement. While the PL is induced by the 532 nm (2.33 eV) pump that scans the MoS_2 area, a change in the PL signal driven by the chopped 1.55 eV remote pump is recorded. The PL signal is observed by a photodetector combined with the monochromator, and the change in PL according to the existence of the pump is obtained by the lock-in amplifier synchronized with the mechanical chopper.

Figure 3.3 shows the schematics of the spatially resolved differential PL measurements. The differential PL (the PL intensity difference with/without the remote pump excitation) was used to detect the spin-polarized electrons injected from WTe_2 to MoS_2. The charge injection was verified in the following way. First, the remote pump was positioned at the edge of the WTe_2 layer; the photon energy (1.55 eV) is well below the bandgap of the MoS_2 monolayer, i.e., 1.88 eV (660 nm). Then, the remote pump was modulated by a mechanical chopper with a chopping frequency of 700 Hz, and the synchronized difference in PL signal was obtained while spatially scanning the 532 nm (2.33 eV) laser. The intensity of the circularly polarized remote pump was 278 W/cm^{2,} and that of the circularly polarized (same helicity as the remote pump) 532 nm CW scanning laser was 39.8 W/cm^2. In this way, the suppression of PL synchronized to the existence of the remote pump could be detected if the spin-polarized electrons generated by the remote pump are injected into the MoS_2 and affects the electron excitation and exciton formation by the scanning 532 nm pump by occupying the MoS_2 conduction band.

The 2D map of the differential PL signals was obtained by combining the position information from the scanning mirror and the PL of the MoS_2 A exciton. The PL spectrum was measured by dispersing the luminescence signal through a monochromator (MonoRa320i, Dongwoo OptronTM).

3.2.3 Time-resolved Kerr rotation microscopy

The pump-induced Kerr rotation angle (θ_K) was measured in the following two ways. First, the 2D distribution of the Kerr rotation angle in the MoS_2 layer was measured at each pump-probe delay Δt with the gate voltage V_G of 2 V. The collected data provide the spatially resolved information at a given Δt. Second, with the chosen target position, e.g., an area exhibiting the largest Kerr rotation changes, we performed detailed studies of the TRKR with varying V_G. In both cases, the pump is far away from the MoS_2 layer. The circularly polarized pump (1.55 eV) with an intensity of 278 W/cm^2 was mechanically chopped with a chopping frequency of 700 Hz. The linearly polarized probe (1.88 eV) with the intensity of 10 W/cm^2 was obtained after a portion of the white-light continuum was spectrally filtered. The Kerr rotation was measured using a combination of a Wollaston prism and balanced detectors.

3.3 Result and discussion

3.3.1 Spatially-resolved differential photoluminescence

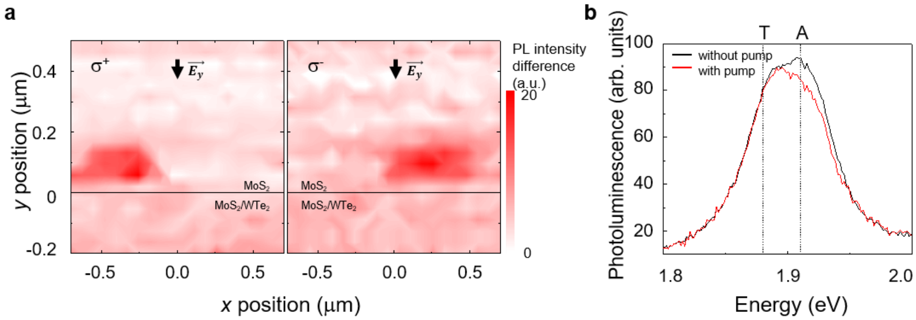

Figure 3.4 Spatially resolved differential PL across the MoS_2/WTe_2 edge boundary. The A exciton PL signal of MoS_2 is suppressed by the electron transfer from WTe_2. **a.** The spatially resolved 2D PL intensity of the MoS_2 A exciton (V_G = 2 V) is shown for the remote pump with σ^+ polarization (left panel) and σ^- polarization (right panel). The center of the remote pump excitation with the 2 μm waist is fixed at (0, -0.2) μm. The edge of the WTe_2 monolayer is located at the solid black line (y = 0 μm), and the longitudinal electrical bias $\overrightarrow{\boldsymbol{E_y}}$ is applied in the direction of the black arrow. **b.** PL spectrum at (0.25, 0.1) μm, with (red) and without (black) the pump pulse is shown. T and A stand for the resonant energies for the trion and the A exciton of MoS_2, respectively.

Figure 3.4a shows the spatially resolved differential PL measured at the A exciton resonance (~ 1.9 eV) of MoS_2 when the 1.55 eV "remote pump" pulse (left panel: σ^+, right panel: σ^-) excites at a position (x, y) of (0, -0.2) μm. The remote pump at WTe_2 with energy ε_1 exclusively excites the spin-polarized electrons in WTe_2, and the electrons are easily transferred to MoS_2 by the band alignment and external electric field (Fig. 3.1c). The transferred electrons then contribute to the differential changes of PL in the MoS_2 layer, which are measured by the local laser excitation using the 2.33 eV diode.

Figure 3.4a clearly shows that the PL signal is spatially bent in an opposite transverse direction when the light helicity of the remote pump is reversed. As displayed in Fig. 3.4b, the PL spectrum shows that the A exciton peak is reduced upon the remote pump excitation; the PL spectra are measured at (0.25, 0.1) μm, which is away from the heterojunction with the remote pump. Intuitively, if no electrons are supplied from the photoexcited MoS_2/WTe_2 edge, the PL spectrum in the MoS_2 region should be featureless irrespective of the remote pump excitation. Therefore, the significantly reshaped PL spectrum with a reduced intensity near 1.9 eV (A exciton energy of MoS_2) shown in Fig. 3.4b evidences the transfer of electrons as expected. Note that although the area of excitation is much larger in the interior (i.e., bulk state) of WTe_2 than the 1D edge, the majority of spin-polarized electrons would originate from the edge while the interior contribution rather appears as a small background because the bulk is lack of distinct helical states, and the density of states of the edge is significantly larger than the bulk[69,70]. The detailed mechanism for the suppression of A exciton PL intensity is investigated by further V_G-dependent PL measurements.

It is well known that PL from a monolayer TMD is sensitive to the carrier density[49,50,71]. For instance, when the gate voltage is applied to make the monolayer TMD n-doped, the increased electron density results in forming a greater negative trion (or attractive polaron) concentration[71]. As a result, the n doping of the monolayer TMD leads to a drastic decrease in exciton resonance peak while the increment of trion resonance peak is negligible in general, regarding the weak oscillator strength of trions[72].

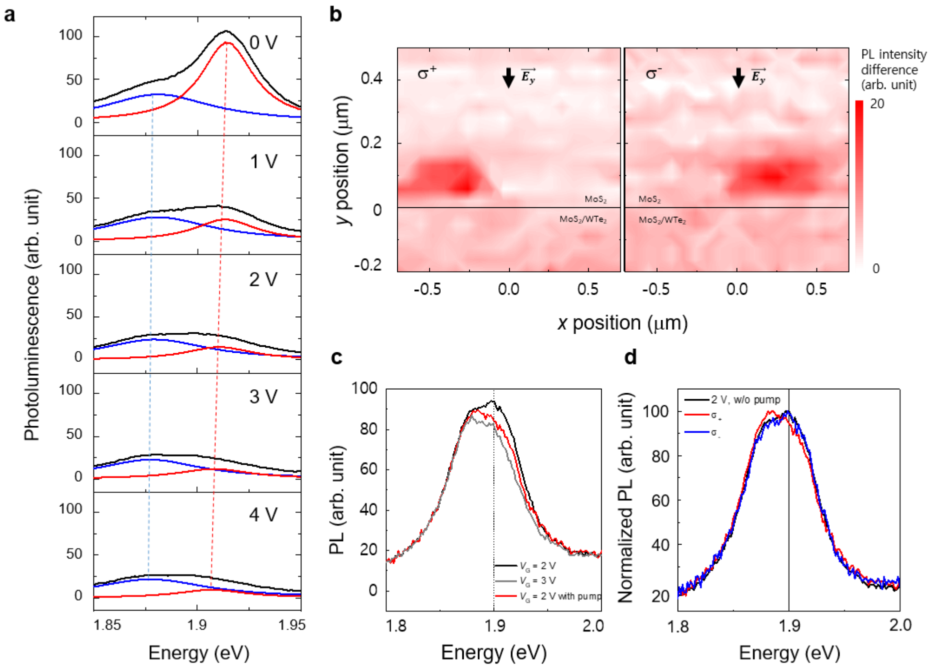

Figure 3.5 a. The V_G-dependent PL of the monolayer MoS_2. The black line represents the total PL signal while the red and blue lines denote the exciton and trion components extracted by the Lorentzian fitting, respectively **b.** The spatially resolved differential PL when V_G = 2 V (same figure as Fig. 3.4a). The *x*-directional deflection of the PL suppression reveals the spin-polarized electron injection and the associated transversal valley Hall transport. **c.** PL spectra when V_G = 2 V, V_G = 3 V without remote pump, and V_G = 2 V with remote pump excitation. **d.** Helicity-resolved PL spectra when V_G = 2 V. Compared to the PL spectrum without the remote pump (black), the injection of spin-polarized electrons change σ^+ component of the PL (red) while the σ^- component of the PL (blue) is unaffected.

Figure 3.5a shows the V_G-dependent PL. The total PL from the monolayer MoS_2 (black line) is decomposed into A exciton (red) and trion (blue) Lorentzian contributions. Significantly distinct V_G dependence of A exciton and trion was observed; the PL from the exciton decreases drastically as V_G increases while trion PL remains unchanged.

Based on the V_G-dependent PL of monolayer MoS_2, the effective injection of spin-polarized electrons is evidenced by comparing the PL spectrum measured at the suppressed region ((0.25, 0.1) of Fig. 3.5b, right panel) with and without the remote pump, as shown in Fig. 3.5c. The resultant PL spectra indicate that the electron injection is equivalent to the increase of V_G from 2 V to ~2.5 V qualitatively (Fig. 3.5c). In Fig. 3.5d, the normalized plot of helicity-resolved PL spectra when σ^+ remote pump is injected in WTe_2 are shown; note that the black line represents the MoS_2 PL without the remote pump. When the σ^+ remote pump injects the spin-polarized electron, the decreased exciton PL appears only in the σ^+ component of PL (red line), while the σ^- component of PL (blue line) is identical to the PL without the remote pump.

The quantitative estimation of how many electrons were transferred from WTe_2 to MoS_2 with conserving its spin polarization can be computed from the V_G-dependent PL and conductance data. Assuming that the PL data when

V_G is 2 V without the remote pump corresponds to 0 % injection efficiency because the PL with the remote pump is measured when V_G = 2 V, the ratio between the current I_{2V} and I_{3V} when V_G = 2 V and 3 V corresponds to the upper bound of the injection efficiency. According to Fig. 3.2, I_{2V} = 0.695 nA and I_{3V} = 0.761 nA so the upper bound of efficiency $(I_{3V}-I_{2V})/I_{2V}$ is 11.2 %.

As discussed above, the PL change is induced by the interlayer charge transfer (electron population transfer from WTe_2 to MoS_2) due to the remote pump excitation in WTe_2. The injected electrons are spin-polarized such that the electrons would fill the conduction band in MoS_2 whose valley index is matched with the associated electron spin, i.e., spin-valley locking. Here, if the electron spin experiences rapid decoherence within the interlayer charge transfer time, the PL changes in MoS_2 should not exhibit a noticeable difference between the σ^+ and σ^- PL in MoS_2. In fact, the experiment result shows that this is not the case.

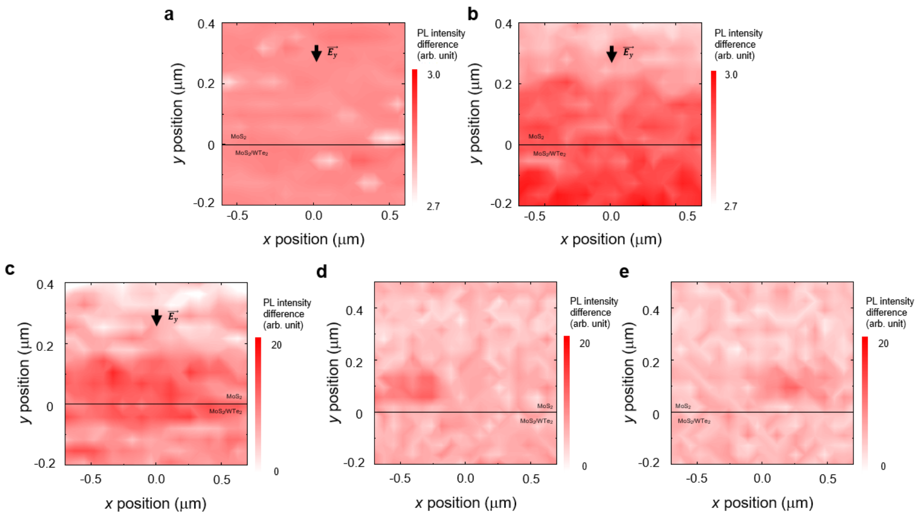

Figure 3.6 Additional data for the spatially resolved differential PL, taken from device #1. The data are shown when V_G is -5 V (**a**) and 6 V(**b**). **a.** When the Fermi level is sufficiently below the conduction band edge (V_G = -5 V), the 1.55 eV pump excitation in MoS_2 has not enough energy to generate any electrons or holes that would be injected into MoS_2. **b.** When V_G = 6 V, the degenerated electron doping of the MoS_2 makes the direct excitation possible by the 1.55 eV pump. **c.** Spatially resolved differential PL (taken from device #1, V_G = 2 V) is presented when the remote pump is linearly polarized. In the absence of the applied longitudinal electrical field, a signature of the valley Hall transport is still observed. The data were taken from device #1 when the polarization of the remote pump is σ+ (**d**) and σ^- (**e**).

In Fig. 3.6, the additional data of spatially resolved differential PL taken from device #1 are shown to support our assumptions for the injection of spin-polarized electrons and the origin of the differential PL. When V_G = -5 V (Fig. 3.6a), the 1.55 eV pump excitation in WTe_2 cannot induce the electron that would be injected into MoS_2 because the Fermi level is sufficiently below the conduction band edge. Therefore, due to the type-I heterojunction between MoS_2 and WTe_2, the suppression of PL is not induced, as shown in Fig. 3.6a. On the contrary, when V_G = 6 V, the degenerated electron doping of the MoS_2 makes the direct excitation by the 1.55 eV pump possible. The effect of the electron injection from MoS_2 becomes negligible, and thus, the differential PL vanishes, as shown in Fig. 3.6b. Figure 3.6c shows the spatially resolved PL data with a 1.55 eV linearly polarized remote pump excitation. We have observed that the suppressed exciton PL is distributed uniformly along the edge with no noticeable valley Hall deflection. This implies the spatial distribution of K and K′ valley polarization is equally spread due to the balanced up and down spin-polarized electrons. For the zero longitudinal bias voltage, we note that although the VHE is not expected to appear in the spatially resolved differential PL, our data (Figs. 3.6d, e) show that such differential PL is not completely absent. Instead, we see a signature of the VHE, though the magnitude is very weak (about 20 % of differential PL when the bias voltage is applied). The transverse spatial displacement of the VHE is quite short (~ 0.2 μm) compared to the non-zero bias voltage (~ 0.4 μm). Although there is no longitudinal bias voltage, the possible scenario may include the thermal gradient and thermoelectric photocurrent, which may give rise to the effective potential gradient. Of course, the small magnitude of valley polarization is because the spin-polarized injection should strongly depend on the longitudinal field strength.

3.3.2 Time-resolved Kerr rotation microscopy

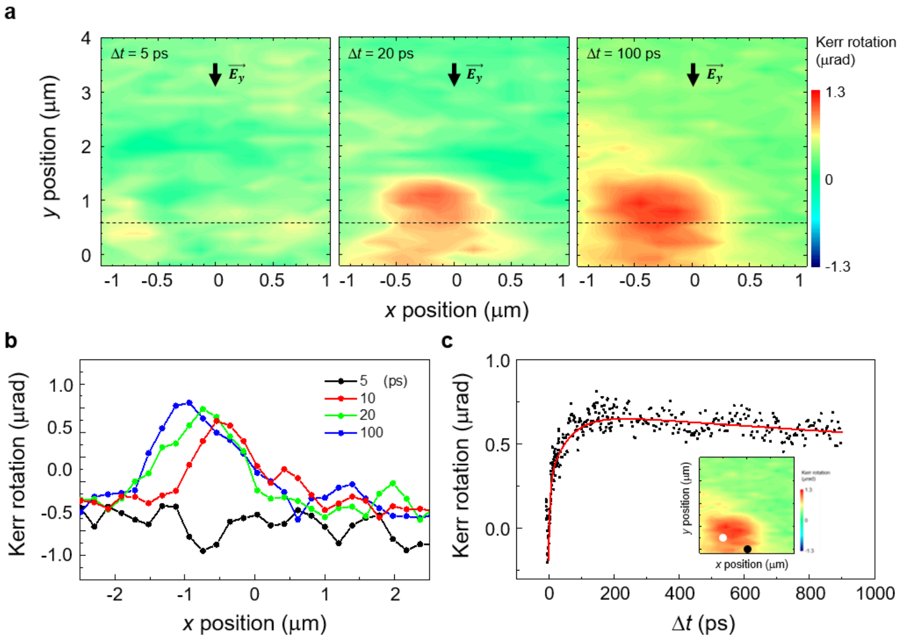

Figure 3.7 Experiment data from the TRKR microscopy **a.** 2D snapshot of spatially resolved Kerr rotation angle show the spatial shift of the valley-polarized electron wave packets over time delay Δ*t* at V_G = 2 V. The center of the remote pump was injected at a fixed position of (0, 0) and the probe scanned the designated area at each Δ*t*. The dashed line denotes the *y*-position for the following line-cut plot. **b.** The one-dimensional line-cut plot of the Kerr rotation angle is displayed for several Δ*t*s. **c.** The time-domain plot of the transient Kerr rotation angle (black dots) shows fast emerging and slow relaxation of θ_K. Solid red line shows a fitting curve for the rising and decaying of θ_K signal. Inset: the time-resolved measurement in Fig. 3.7c is done when

V_G = 2 V, with the center of the remote pump at (0, 0) μm and the center of the probe at (-0.5, 0.5) μm as denoted by a black dot and white dot on the inset contour plot, respectively.

For the further understanding of VHE arising from the injected spin-polarized electrons, the temporally and spatially resolved Kerr rotation was investigated. Figure 3.7 shows the spatially resolved TRKR data in the MoS_2 layer to visualize the transient shift of θ_K after ultra-short remote photoexcitation in the WTe_2 edge. The 2D maps of θ_K at different temporal delay Δt between the remote pump and the Kerr rotation probe pulse. Figure 3.7a shows the 2D maps of θ_K when V_G = 2 V and the helicity of the remote pump is σ^+. In Fig. 3.7b, the line-cut plots of θ_K at different Δt obtained at y = 0.7 μm are shown. Here, the time-dependent spatial shift of the θ_K corresponds to the transverse Hall transport of spin-polarized electrons.

Assuming that the thermal gradient, as well as the electric field of the remote pump, can be approximated as a Gaussian profile, the valley hall velocity v_H and corresponding Hall mobility μ_H can be obtained by regarding the emergence of θ_K as the spatial overlap of the valley-polarized electron wave packet and the probe beam over time. Supposing the two components exhibit a Gaussian distribution, the θ_K at a fixed point can be expressed as

$$\theta_K(r) \propto n_e \cdot I = n_{e,0} I_0 \left[e^{-\frac{2r^2}{R}} \right], \quad (3.1)$$

where n_e is the charge concentration of the valley-polarized electron wave packet, I is the probe beam profile, and R is the size (radius) of the Gaussian functions. The probe beam spot is measured to be ~ 2 μm. Here, the two Gaussian distributions and the transport speed of the valley-polarized electron wave packet is assumed to be unchanged. The transport velocity is computed by dividing R by the rising time, while the rising time is a temporal waist obtained from the exponential fitting of transient θ_K that would be discussed below (Fig. 3.7c). The resultant v_H was 1.87×10^3 m/s and with the corresponding $\mu_H = 4.49 \times 10^3$ cm^2/Vs. Such transverse transport characteristics are by far larger than the best known longitudinal Hall mobility μ_l of 1,020 cm^2/Vs with 1D graphene edge contact[73].

The dynamic details of the non-excitonic VHE were investigated at a fixed probe position of (-0.5, 0.5) μm in MoS_2. After acquiring the valley Hall transport properties. A representative example is shown in Fig. 3.7c for V_G = 2 V. After the TRKR signal increases with a rising time constant of about 37 ps, the signal reaches a peak at ~ 100 ps. Then much slow decaying dynamics were observed with a time constant of about 4 ns. Before explaining the subsequent TRKR experiments and discussing the non-excitonic valley Hall dynamics, there are some dynamic factors involving intralayer and interlayer excitons for the long decaying transient that should be addressed and excluded.

. First, prior local TRKR investigations in monolayer WSe_2 revealed that the depolarization rate of intralayer exciton valley polarization is around 0.5 ps^{-1} [74-76]. In addition, ultrafast four-wave-mixing [61] and pump-probe [77] spectroscopy have evidenced that the intervalley electron-hole exchange interaction is the origin of the rapid valley depolarization that occurs within 1 ps. No such rapid valley depolarization was observed in TRKR experiments. Thus, the valley-polarized exciton dynamics can be ruled out. Second, the interlayer exciton dynamics[38,78-80] cannot contribute to our TRKR signal considering the spatially separated pump and probe, the energy band alignment of gapped MoS_2 and metallic WTe_2, and the existence of the bias voltage. Lastly, the relatively long spin-flip transition can also be excluded simply because no sign change was observed in our long-lasting TRKR trace. Given that electrons dominate the valley Hall transients observed in the experiments, such an ns-long valley lifetime can be thought of as the characteristics of the conduction band split by the spin-orbit coupling (SOC), similar to the long-lived valley holes in the type-II heterostructures[64]. The small contribution of the electron-hole exchange interaction, as well as the suppressed intervalley spin-flip and the momentum transfer of electrons, are the key contributors to our long-lasting valley polarization.

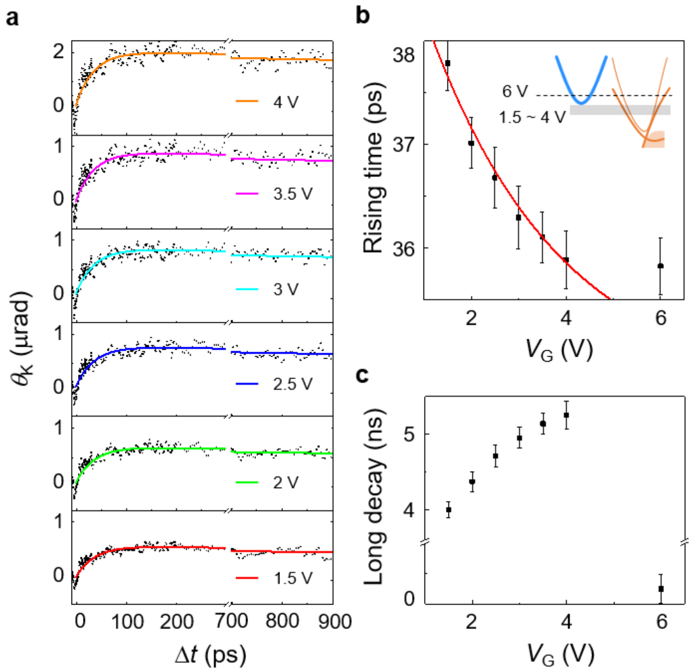

Figure 3.8 Gate-dependent Kerr rotation dynamics. **a.** Time-resolved Kerr rotation dynamics are shown with increasing V_G from -1.5 V to 4 V. Dots are the measured data, and the solid lines are the fitting curves. **b.** The V_G dependence of the rising time constant acquired from fittings in **a** (black dot with error bar). The obtained time constant is compared with the theoretical expectation (red line, not a fitting curve) computed from the valley Hall conductivity (Eq. (3.6)). Inset: the schematic energy diagram when the V_G = 1.5 ~ 4 V (shaded area), and V_G = 6 V (dashed line). **c.** The V_G dependence of the long decay time constant given by the fitting in **a**. The error bars indicate standard error.

Based on the above rationales, the V_G-dependent TRKR measurements were performed to understand the non-excitonic VHE. Figure 3.8 presents the TRKR results measured at V_G from -1.5 V to 4 V. The emerging transients can be understood as the valley-polarized electron wave packet approaching the probe position due to the onset of the VHE. Therefore, the valley Hall transport velocity can be obtained from the rising time. Figure 3.8b shows that the rising time becomes faster. Thus, the Hall conductivity is larger with increasing V_G. Using such interpretation, the experimental data are compared with the theoretical estimation of the valley Hall conductivity σ_{VH}. The monolayer MoS_2 has a C_{3h} symmetry with a strong spin-orbit coupling (SOC). The corresponding Hamiltonian is

$$\hat{H} = at\left(vk_x\hat{\sigma}_x + k_y\hat{\sigma}_y\right) + \frac{\Delta}{2}\hat{\sigma}_z - \lambda v\frac{\hat{\sigma}_z - 1}{2}\hat{s}_z \ , \quad (3.3)$$

where a is the lattice constant, t is the effective hopping integral, $v = \pm 1$ is the valley index, $\hat{\sigma}$ is the Pauli matrix, and Δ is the bandgap. The last term represents SOC, where 2λ and $\hat{s}_z$ denote the spin splitting of the valence band and the Pauli spin matrix, respectively. Using the cell periodic Bloch function u(k), the Berry curvature is defined as

$$\Omega_n(\mathbf{k}) \equiv \hat{z} \cdot \nabla_k \times \langle u_n | i\nabla_k | u_n(\mathbf{k})\rangle, \quad (3.4)$$

and the Berry curvature in the conduction band is [52]

$$\Omega_C(k) = -v\frac{2a^2t^2\Delta'}{[\Delta'^2 + 4a^2t^2k^2]^{\frac{3}{2}}} \ , \quad (3.5)$$

where $\Delta' = \Delta - vs_z\lambda$. Because the Berry curvature is an intrinsic property, one can isolate the intrinsic contribution from various extrinsic effects. The valley Hall velocity v_{VH} can be expressed as Eq. (3.2) using the electric field and the Berry curvature[37]

$$\boldsymbol{v}_{\mathrm{VH}} = \frac{1}{\hbar}\Omega(\mathbf{k}) \times e\mathbf{E} \ . \quad (3.2)$$

Besides, we used the approach of calculating valley Hall conductivity σ_{VH} to estimate the valley Hall mobility.

$$\sigma_{\mathrm{VH}} = -\xi \frac{e^2}{\hbar} \sum_n \frac{d\mathbf{k}}{(2\pi)^2} f\big(\varepsilon_n(\mathbf{k})\big)\Omega_{\mathrm{C}}(\mathbf{k}), \quad (3.6)$$

where ξ is the antisymmetric tensor, n is the band index in the 2D limit, $f\big(\varepsilon_n(\mathbf{k})\big)$ is Fermi-Dirac distribution, and $\Omega_{\mathrm{C}}(\mathbf{k})$ is the Berry curvature derived in Eqs. (3.4) and (3.5). Based on the Berry curvature and known parameters of the monolayer MoS_2[52], the intrinsic contribution can be calculated. Then, the valley Hall transport mobility μ_{VH} is derived as a function of ρ for the comparison with the experimental results. The agreement is excellent for V_G = 1.5 ~ 4 V (Fig. 5b). In this gate sweep regime, the Fermi level lies below the conduction band edge of MoS_2; the anomaly seen at V_G = 6 V may arise from the intraband electron excitation in the degenerately doped MoS_2. Note that Eq. (3.2) does not contain any extrinsic contributions of the VHE, such as skew-scattering and side-jump mechanisms[81]. This implies that the non-excitonic unipolar VHE is dominated by the intrinsic contribution, which depends only on the Berry curvature landscape of the crystal. For the quantitative comparison, we have listed the valley Hall mobility μ_H and longitudinal mobility μ_l in Table 3.1. Indeed, our measurement is exceptionally larger than the exciton-based VHE.

Table 3.1 Comparison of valley Hall mobility and longitudinal mobility.

Mobility (cm^2/Vs)	Reference
4,490	This work
6.86×10^{-3}	*Science* **344**, 1489-1492 (2014) (μ_H)[55]
160	*Science* **360**, 893-896 (2018) (μ_H)[63]
1012	*Nat. Nanotechnol.* **10**, 534-540 (2015) (μ_l)[68]
~1000	*Nat. Commun.* **10**, 611 (2019) (μ_l, 2 K)[82]

The slow decay of θ_K with a time constant of about a few nanoseconds represents the slow valley depolarization after the emerging dynamics from the valley-polarized electron wave packets. There are two possible dynamic processes associated with the corresponding origins: valley depolarization without losing the electron population and with losing through inelastic electron scattering. Under the unipolar carrier regime of the experiments in this study, the effect of electron-hole annihilation through either intravalley or intervalley exciton recombination may not significantly reduce the valley-depolarization lifetime. As discussed, the efficient intervalley electron-hole exchange interaction cannot cause the observed long valley-depolarization lifetime [60,83]. Figure 3.8c summarizes the TRKR decaying time constants.

Compared to Fig. 3.8b, while the valley Hall velocity follows $v_{\mathrm{VH}} \propto e^{-V_{\mathrm{G}}}$, the ns-long decaying time monotonically increases, which is independent of the velocity of electron wave packets. It substantiates that the intrinsic mechanism is indeed the dominant origin in our case.

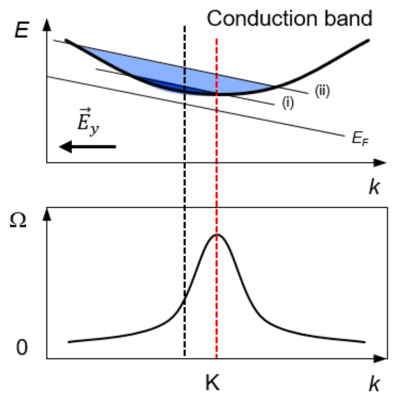

Figure 3.9 Schematic diagram describing the effect of the longitudinal field ($\vec{\boldsymbol{E}}_{\boldsymbol{y}}$) on the electron distribution. K point of the momentum space is expressed as a red dashed line, and the bottom of the conduction band near the Fermi surface E_{F} is marked as a black dashed line. As V_{G} increases, the increased amount of electron injection and the higher Fermi surface lead to the change of electron distribution after thermalization from (i) to (ii). Note that Berry curvature is concentrated near at K point. More electrons experience a larger Berry curvature in case (ii) compared to case (i).

Although both emerging and decaying dynamics of the non-excitonic VHE evidenced the dominance of the intrinsic contribution, the relationship between the V_{G} and μ_{VH} observed in the experiment (Figure 3.8b) should be discussed since the Berry curvature is irrelevant to the change in V_{G}. The intrinsic valley Hall velocity v_{VH} depends only on the Berry curvature and the electric field E applied to the electron in the band as expressed in Eq. (3.2)[37,84]. Note the Berry curvature is an intrinsic character determined by the lattice symmetry of crystal solids. According to this expression, the transverse valley Hall velocity would not be changed as long as the longitudinal electric field is constant, which for most of the cases is done by applying DC source-drain potential gradient[55,59,82]. In other words, the proportional relationship between μ_{VH} and V_G shown in Fig. 3.8 is not explicit. Instead, changing V_G, i.e., increase or decrease of the total electron population, leads to valley Hall mobility changes by rendering more or fewer electrons to be affected by a larger or smaller Berry curvature distribution in the momentum space.

In the experiments using the monolayer MoS_2, changing the electron density by V_G controls the electron distribution in the MoS_2 conduction band. The applied longitudinal electric field $\vec{E}_y$ makes the Fermi surface tilted in momentum space, as schematically shown in Fig. 3.9. After the thermalization and cooling are finished, the injected group of electrons fills the conduction band from the point marked as a black dashed line in Fig. 3.9. When V_G increases, the electron population at the K (or K′) point increases, whose effect is explained as the band filling from (i) to (ii). This appears as a faster rising dynamic component in our TRKR because the non-zero Berry curvature is concentrated at the K and K´ point of the band extrema in the momentum space, i.e., the tilted Fermi surface makes the injected electrons away from the K or K´ point.

In fact, the intrinsic SHE of injected spin-polarized electrons can lead to the deflection of θ_K in the *x*-direction, similar to what was observed in the experiments. Moreover, the spin splitting of the monolayer MoS_2 conduction band is much smaller than the valence band. Thus, the spin polarization of the injected electrons may not lead directly to effective valley polarization. If the valley polarization is not originated from the injection of spin-polarized electrons due to the small spin splitting, the experimental results can purely arise from the spin-polarized electron regardless of the valley degree of freedom. However, the transverse Hall transport observed in our experiments is a strong signature of the VHE rather than the SHE due to the following reasons. First, the θ_K signal exhibit ns-long decaying transients, denoting a far slower dynamic process when compared with the spin lifetime of the MoS_2 conduction band at 77 K because of the highly efficient Elliot-Yafet spin relaxation of the small spin splitting. Therefore, the long-lasting Kerr rotation signal represents the valley polarization. Secondly, the anomalous Hall conductivity calculated from the experiment results matches very well with the valley Hall conductivity. For an electron-doped system (such as our case), the spin Hall conductivity is about λ/Δ of the valley Hall effect, where 2λ is valance band spin splitting and Δ is the bandgap[52]. Considering an order-of-magnitude difference between λ and Δ of the monolayer MoS_2, the valley Hall effect overwhelms the spin Hall effect in the total anomalous Hall transport.

3.4 Conclusion and outlook

In conclusion, the non-excitonic VHE was demonstrated and explored using a MoS_2/WTe_2 heterobilayer structure in this study. The 2D time-resolved Kerr rotation microscopy strongly suggests that the transversal Hall dynamics is governed by the Berry curvature distribution through the intrinsic contribution of VHE. The valley Hall transport dynamics were investigated by analyzing the transient shifting of θ_K, and the results were compared with the theoretical estimation based on quantum mechanical transport theory. From a quantitative perspective, exceptional transport properties represented by v_H = 1.87 x 10^3 and μ_H = 4.49 x 10^3 cm^2/Vs were achieved by the non-excitonic regime.

Although this establishes the understanding of non-excitonic and purely intrinsic VHE, it reserves much room to improve for the practical ‘valleytronics’. For example, the use of large SOC-coupled valence bands shall increase the valley-polarized lifetime by a few orders of magnitude. Such a perspective potential, together with the unique TMD/TI heterobilayer characteristics, can pave the way toward a new 2D platform for realizing valley-based information processing.

CHAPTER 4 – SPINFUL HELICAL HINGE STATES IN THE HIGHER-ORDER TOPOLOGICAL INSULATOR

4.1 Introduction

Beyond the previous understanding of band topology, a new class of topological phase, namely a higher-order topological insulator (HOTI), is proposed recently on the basis of the generalized bulk-boundary correspondence. This extended concept of bulk-boundary correspondence covers *d*-2 or lower-dimensional topological boundaries in *d*-dimensional systems[28,29,85]. For instance, a 3D HOTI may host gapless 1D “hinge” states, where the gapped 2D surfaces are facing each other with a reversed sign of the mass. Such a phenomenon can be understood based on the fact that the bulk bands form doubly inverted structures under the presence of strong

SOC[28,30,31,86]. With these physical grounds, the band structure and the corresponding topological features of condensed matter HOTIs have been predicted by firm theoretical methods such as a multi-orbital tight-binding model, first principle calculation, and Wilson loop calculation[28-31,85,86]. As a result, a few condensed matter systems such as bismuth[32,33], topological crystalline insulator SnTe[28,30,34], twisted bilayer graphene[35,87,88], and some artificial lattices[89,90] are predicted to be HOTIs to date.

Among such candidates, WTe_2 has recently attracted much interest for its band topology and Berry curvature[91,92]. With an orthorhombic 3D crystal, it was first known as a type-II Weyl semimetal with electron and hole pockets around the Weyl points[31,93,94]. However, resolving the Weyl points remains challenging because the momentum space separation of the Weyl point of WTe_2 is far smaller than the resolution of angle-resolved photoemission spectroscopy (ARPES)[95,96]. In a monolayer limit, the thickness-dependent first-principle calculations and transport experiments revealed the quantum spin Hall insulating phase of 1T′-WTe_2 crystals[66,67]. After recent proposals on the higher-order topology, the large arc-like surface states of the bulk WTe_2, which were initially considered as characteristic Fermi arcs of the Weyl semimetal or the topologically trivial states, are started to be understood as the signature of gapped fourfold Dirac surface states[30]. For the practical demonstration, superconducting current analysis of a Josephson junction made of WTe_2 was then used to identify the hinge states as a clue for the higher-order topology[32], and subsequent experiments have reported anisotropic confinement of 1D conducting hinge channels in few-layer T_d-WTe_2[97,98]. However, experimental evidence for the symmetry-protected topological nature of the observed 1D hinge state and investigation on any spin-related phenomenon is still lacking. Moreover, in a broader sense, a time-reversal invariant spinful feature of the helical HOTI in a practical solid-state system has not been investigated[99].

In this study, the experimental evidence for the time-reversal invariant HOTI phase with spinful and helical hinge states in atomically thin T_d-WTe_2 is provided. Particularly designed WTe_2-graphene heterostructure devices were used to investigate the spin orientation of hinge states through the spatially resolved polar MOKE measurements. The experimental results match the previous reports on possible gapless spin-polarized states in the multilayer WTe_2 and further showed that those spinful states are protected by the time-reversal symmetry[100,101]. The bulk- (or gapped surface-) and hinge-originated spin polarization was distinguished by the Fermi level dependence of the Kerr rotation signals in the experiments. Furthermore, the time-reversal invariance of the spinful hinge states was examined by confirming the mass gap opening under the external magnetic field.

4.2 Experiments

Figure 4.1a shows the crystal structure of the multilayer orthorhombic T_d-WTe_2, which is a non-centrosymmetric structure belonging to the SG 31 ($Pmn2_1$) point group with two perpendicular axes (a- and b-axis) and one mirror line along the b-axis. These spatial symmetries and the time-reversal symmetry satisfies the necessary prerequisites to support the non-trivial spin-polarized helical hinges in HOTI[100,102]. In the heterostructure device used in experiments, multilayer WTe_2 is placed on monolayer graphene to detect the spinful 1D hinge state by observing the spin polarization of electrons in graphene that is injected from WTe_2.

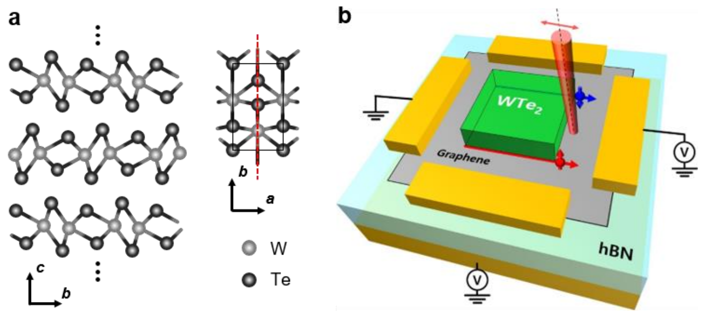

Figure 4.1 Crystal structure of multilayer T_d-WTe_2 and experimental design. **a.** The T_d structural phase of multilayer WTe_2 is non-centrosymmetric and has an in-plane mirror plane M_a (red dashed line). **b.** Schematic diagram of the experimental design for detecting the spin-polarized electronic states in WTe_2. The electrical bias voltage makes electrons flow through WTe_2, while the spin polarization of the electrons is optically recorded as the Kerr rotation θ_K induced in the linearly polarized pump (980 nm, 1,415

W/cm^2). The pump laser sweeps through a 6 μm x 10 μm region at graphene near the edge of WTe_2 to obtain the spatially resolved θ_K data.

4.2.1 Experiment design

The experiment schematic illustrated in Fig. 4.1b summarizes the key concept of spatially resolved experiments to detect the spinful hinge states. The spatially resolved differential Kerr rotation ($\Delta\theta_K$) measurement using a WTe_2-graphene heterostructure device is designed for the detection of spin-polarized electrons in graphene that is injected from the multilayer WTe_2. The electrodes are directly contacted with graphene only. Thus the heterostructure can be modeled as a resistive circuit with two resistors connected in a parallel way (Fig. 4.2). When the bias voltage is applied to graphene, the current is induced in WTe_2 as well as in graphene because there is a finite resistance both for WTe_2 and graphene channels. As a result, a portion of electrons in graphene flows through WTe_2, and those electrons are injected back into graphene during the conduction, as shown in Fig. 4.2. Therefore, the signature of the spin-polarized states in WTe_2 can be detected by optically inspecting the spin-polarized carriers in graphene. To cancel out any effect of unintentional background factors, such as defects in graphene or chemical residues during the device fabrication process, the spatially resolved θ_K was measured with and without the bias voltage (V_{bias} = 0.5 V) and the difference between two measurement $\Delta\theta_K$ was used for the further analysis.

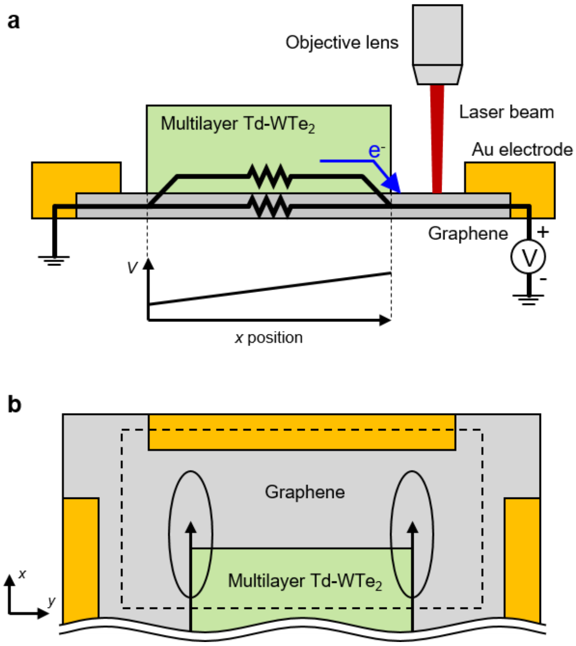

Figure 4.2 Schematic diagram explaining how the WTe_2-graphene heterostructure device works in this study. **a.** The heterostructure can be modeled as a circuit with two finite resistance connected in a parallel way. The bias voltage applied between two contacts induces a current both through the WTe_2 and the graphene. Electrons injected into graphene from WTe_2 (blue arrow) are optically investigated to determine the spinful characteristics of the electronic states in WTe_2. **b.** Top view schematic diagram of the device explaining the region of the spatially resolved MOKE measurement. The dashed box indicates the range of spatial scanning while the longitudinal electric field is applied to the $-x$ direction. Arrows denote the injection of electrons from WTe_2 to graphene. The localized $\Delta\theta_K$ was expected to appear in the region marked with black circles.

There are the following reasons why graphene was used to detect the signature of the hinge states instead of direct optical probing at the hinges. First, the spatial length scale of the hinge states, which is only a few nanometers wide[88,89], accounts for only a small fraction of the spot size of the incident laser beam (diameter ~1.5 μm). This means that any meaningful optical responses originating from the hinge state would be extremely weak compared to the optical responses of the bulk, surface, and any other background signal generated within the beam spot. Therefore, the scaling problem limits the signal-to-noise ratio and hinders the direct detection of the hinge state if $\Delta\theta_K$ were to be measured on the laser-excited hinges. Secondly, because the hinge, by definition, is a junction between two surfaces orienting in distinct directions, an incident laser introduces both the in-plane and the out-of-plane excitation at the two surfaces facing the hinge. In this case, the electrons excited according to the optical selection rule can have complex spin polarization configurations. Lastly, while the edge of the 2D surface is excited by the pump, the 1D hinge may induce an anisotropic polarization-dependent reflection of light that affects the light polarization after the reflection and hinders the isolation of actual $\Delta\theta_K$ from the spin-polarized state.

To prevent the geometric artifact expected to rise during the direct optical excitation at the hinge, graphene layer was used to elicit the spin polarization of electrons in the hinge states. Graphene is known to exhibit a long spin diffusion length of up to 30 μm due to weak spin-orbit coupling and high carrier mobility[90,91]. In the heterostructure device used in the experiments, the electric potential gradient generates the longitudinal electron transport that injects electrons from WTe_2 to graphene, and the spin polarization of the injected electrons can survive long enough to be detected by MOKE measurements owing to the long spin diffusion length of the graphene. As a result, $\Delta\theta_K$ is distributed into the graphene rather than the localized WTe_2 hinges. Thus a line cut at $x = 0.75$ μm obtained from the spatially resolved measurement was used to analyze $\Delta\theta_K$ while keeping a certain distance from the edge of the WTe_2 crystal, which is responsible for the aforementioned artifacts.

4.2.2 Device characteristics

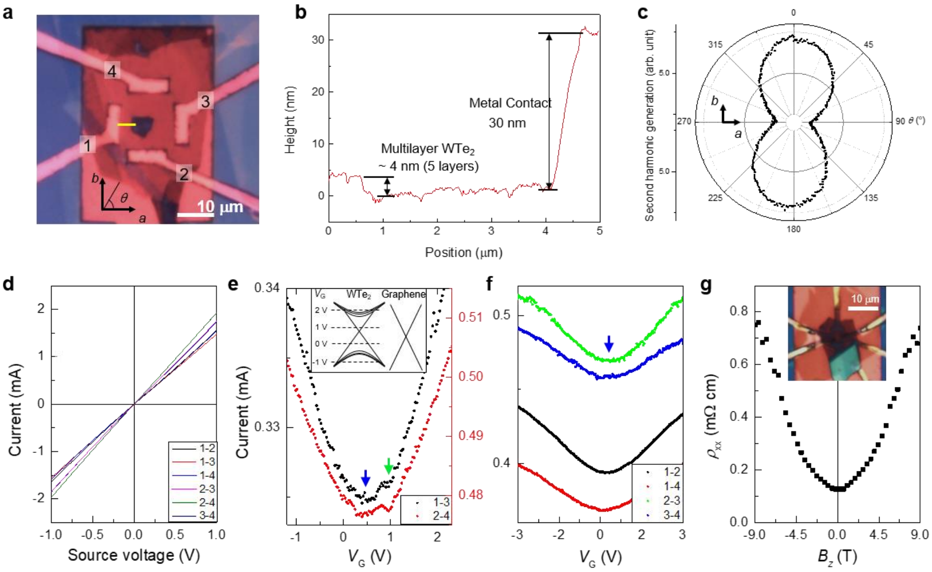

Figure 4.3 Device geometry and electrical characteristics. **a.** An optical microscope image of device #1 with the number index for each metal contact. AFM scan was taken along the yellow line. **b.** The AFM data indicates the thickness of the multilayer WTe_2 flake is ~ 4 nm which corresponds to 5 atomic layers of WTe_2. The thickness of the metal contact shown in the data (30 nm) matches well with the targeted deposition thickness. **c.** The light polarization-dependent SHG was measured at the center of the multilayer WTe_2 in device #1. An 800 nm short pulse with an average intensity of 2,830 W/cm^2 was used as a pump. Anisotropic SHG reveals the crystal axes of the multilayer WTe_2. **d.** Current-voltage output curve of device #1 for each pair of source-drain contacts. All contacts are revealed to form Ohmic junctions. Numbers in the legend indicate the contact combinations used in each measurement. **e,f.** V_G-dependent transfer curve. 0.5 V of drain voltage was applied. **g.** The magnetoresistance of the multilayer WTe_2 was measured in a separate Hall measurement device shown in the inset. The applied gate voltage was 0.9 V, which is close to the charge neutral point. The magnetoresistance does not saturate within $|B_z| \leq 9$ T.

Figure 4.3a shows the optical microscopy image of a complete heterostructure device with electrodes (device #1). The thickness of multilayer WTe_2 was confirmed by atomic force microscopy (AFM), as shown in Fig. 4.3b. The light polarization-dependent SHG using a 30-fs, 800-nm short pulse (Mira 900, Coherent) is shown in Fig. 4.3c. The significant amount of SHG shows the lack of inversion symmetry in the multilayer WTe_2. In addition, the anisotropic SHG reveals the axis orientation of the multilayer WTe_2 crystal in the device. The orientation is consistent with the result of the polarization-dependent absorption measurement[103].

The two-terminal I-V curves and V_G-dependent transfer curves (at the bias voltage of 0.5 V) measured with device #1 are shown in Figs. 4.3d, e. All contacts formed Ohmic junctions (linear I-V curves), and the transport characteristics between the combinations of contacts were found to be uniform (resistance ~600 Ω)[104,105]. The transfer curves in Figs. 4.3e, f shows the effect of electrostatic doping on the current flow in our heterostructure. A charge neutral point of graphene and WTe_2 were observed when the current was measured between contact 1, 3, and 2, 4, as marked as blue and green arrows in Fig. 4.3e, respectively. This corroborates the validity of the current flow model described in Fig. 4.2.

For the further potential-dependent experiments, the Fermi-level change ΔE_F with respect to the applied bottom gate voltage V_G was estimated first, where ΔE_F is a differential change of E_F compared to $V_G = 0$ V. Here, a simple electrostatic calculation of $Q_{2D} = C_i V_i$ [106] was used, where $Q_{2D} = eA\int_0^{E_F} \frac{2|E|}{\pi\hbar^2 v_F^2} dE$ is the total charges accumulated in graphene with area A due to the gate voltage, $C_i = \varepsilon \frac{A}{d}$ is the capacitance of the graphene-hBN-electrode capacitor, and V_i is the gate voltage applied across the gate insulator hBN. Following parameters were used for the numerical computation of the Fermi-level change ΔE_F: the Fermi velocity of graphene near Dirac point $v_F \sim 1 \times 10^6$ m/s[107], the permittivity of hBN $\varepsilon = 3.75\varepsilon_0$[108], and the thickness of hBN $d = 25$ nm. With these parameters, the ΔE_F induced by the gate voltage V_G was estimated. For example, V_G of -1 and 2 V corresponds to -10 and 20 meV, respectively.

Figure 4.3g shows the magnetoresistance of the multilayer WTe_2 measured in a separately made device fabricated in Hall bar geometry. The maximum magnetic field applied during the measurement (attoDRY 2100, Attocube systems) was 9 T. The non-saturating magnetoresistance up to 9 T can be attributed to the compensated electron and hole density[109], proving the high quality of the WTe_2 single crystal used in this study.

4.2.3 Spatially resolved differential Kerr rotation measurement

The Kerr rotation measurements were performed at a temperature of 1.62 K in a closed-cycle cryostat system (attoDRY 2100, Attocube systems) combined with an objective lens (LT-APO/NIR/0.81, Attocube systems) focusing the pump laser at the sample position with the spot size of 1.5 μm. The position of the sample was adjusted by piezo stages, and the position of the pump laser was controlled by a pair of scanning mirrors (GVS012/M, Thorlabs). The 980 nm pump laser was obtained by using a 980 nm centered bandpass filter (FB980-10, Thorlabs) and the supercontinuum light source (SuperK COMPACT, NKT Photonics). The pump power at the sample position was set to 25 μW, and the light polarization was tuned by a polarizer (GL10-B, Thorlabs) and a $\lambda/2$ wave plate (AHWP05M-980) mounted on a motorized rotation stage (PR50PP, Newport). The pump laser was modulated by an optical chopper with a frequency of 1.7 kHz. The Kerr rotation angle θ_K was measured using a Wollaston prism (WP10, Thorlabs) and balanced detectors along with a lock-in amplifier (SR850, Stanford Research Systems). The bias voltage and gate voltage was controlled by the electrical data acquisition system (BNC-2110 and DAQ, National Instruments). The longitudinal bias voltage applied to the device during the experiment was set to 0.5 V.

4.3 Result and discussion

4.3.1 Spatially-resolved differential Kerr rotation measurement

The V_G-dependent Kerr-rotation signals were first investigated to find the spinful characteristics of the anisotropic WTe_2 hinge states. Figure 4.3e shows the transfer curve between contact 1 and 3, i.e., parallel to the a-axis referring to Fig. 4.3a. The conductance deeps observed at V_G = 0.5 and 0.95 V correspond to the charge neutrality point of the graphene and the multilayer WTe_2, respectively, as illustrated in the inset of Fig. 4.3e. 2D contour plots in Fig. 4.4 present the spatially resolved $\Delta\theta_K$ near the WTe_2 edge with different V_Gs in the absence of the external magnetic field. At V_G = 0 and 1 V, a substantial amount of the spin-polarized electrons is concentrated near $y = \pm 1.85$ μm, while $\Delta\theta_K$ is evenly distributed throughout $|y| \leq 1.85$ μm at $V_G < -1$ and $V_G > 2$ V. Considering the V_G-tuned Fermi level described in Fig. 4.3e and the spatial distribution of $\Delta\theta_K$ in Fig. 4.4, the observed $\Delta\theta_K$ distributions at V_G = 0 and 1 V match with the spin-polarized in-gap states localized in the hinge, while those of V_G = -1 and 2 V represent the electrons from the spin-split bulk bands. The $\Delta\theta_K$ near the two parallel hinges has opposite signs, indicating the spinful and helical nature of the localized electron states.

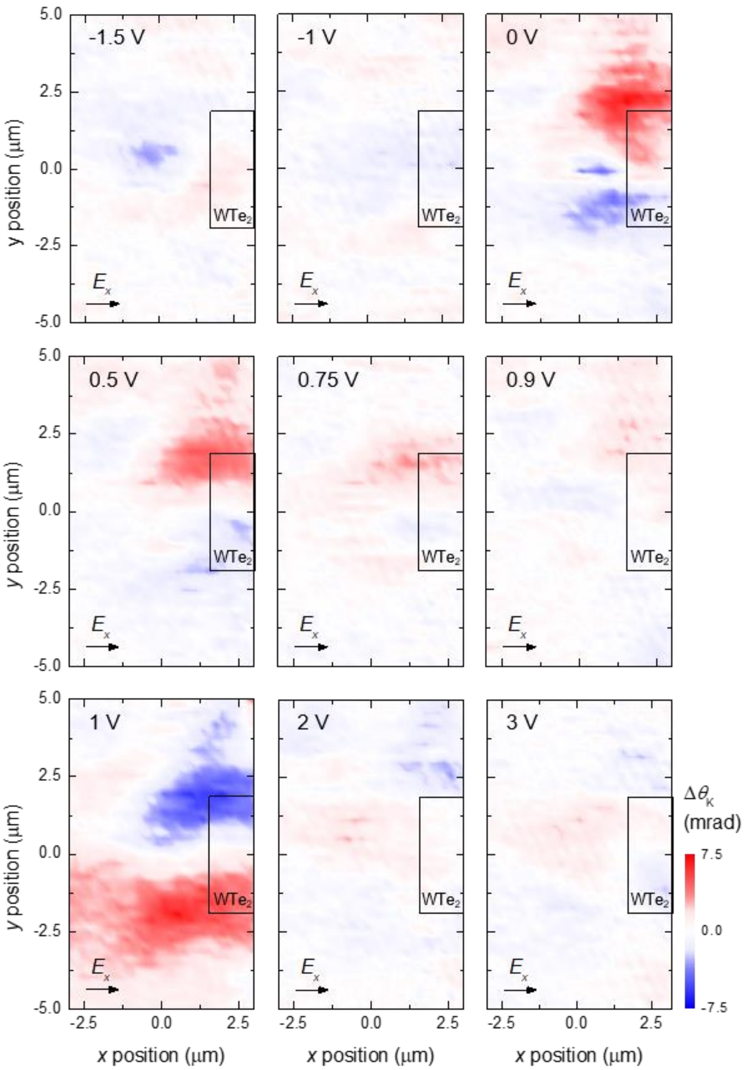

Figure 4.4 The full dataset of spatially resolved V_G-dependent $\Delta\theta_K$ measured in device #1 is shown as 2D contour plots. The bias voltage of 0.5 V was applied to generate a longitudinal electric field in the $+x$ direction, and no external magnetic field was applied. The applied V_G is indicated at the top left side of each panel. The black rectangle

indicates the location of the left end part of the multilayer WTe_2. When V_G is between 0 and 1 V, a large $\Delta\theta_K$ is visible at the y position of the hinges, as well as a sign flip of $\Delta\theta_K$.

To elucidate the bulk- and hinge-originated $\Delta\theta_K$ in detail, the line-cut plots of y-dependent $\Delta\theta_K$ measured at different V_G were obtained from the 2D contour plot as shown in Fig. 4.5. In the bulk-insulating range of V_G (Fig. 4.5, top panel), $|\Delta\theta_K|$ localized at $|y|$ = 1.85 μm decreases monotonically with increasing V_G, and $\Delta\theta_K$ changes the sign abruptly when V_G reaches 1 V, where the Fermi level passes the charge neutral point at V_G = 0.95 V (Fig. 4.3e). In contrast, when WTe_2 is degenerately doped, i.e., $V_G \geq 2$ V or $V_G \leq -1$ V (Fig. 4.5, bottom panel), $\Delta\theta_K$ evenly spreads across $|y| \leq 1.85$ μm and no sign change of $\Delta\theta_K$ across the y position was observed. Note that the sign of $\Delta\theta_K$ implies the orientation of spin-polarized electrons, and $|\Delta\theta_K|$ reflects the concentration of the conducting electrons (or the density of state at the Fermi level, equivalently) with the corresponding spin polarization. These results strongly suggest that although the spin configuration of helical hinge states of the bottom surface of multilayer WTe_2 resembles that of the spin-momentum-locked helical edge states of the 2D quantum spin Hall insulator, while the multilayer WTe_2 is not simply a stack of weak 2D topological insulator layers as proven previously[97].

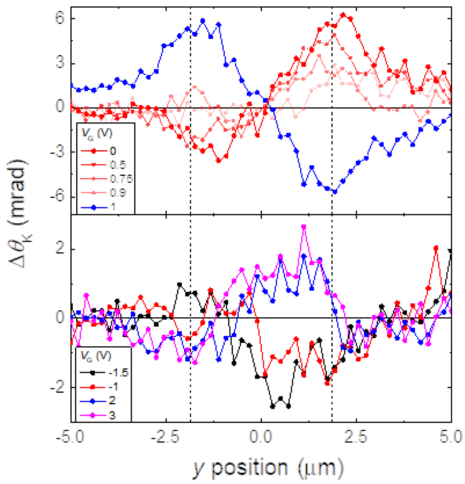

Figure 4.5 Line-cut plots of $\Delta\theta_K$ at x = 0.75 μm. The V_G-dependent $\Delta\theta_K$ in the top panel (0 V$\leq V_G \leq$ 1 V) shows the localized $\Delta\theta_K$ near y = ±1.85 μm; these y positions correspond to the position of the WTe_2 hinge (black dashed lines). The V_G-dependent $\Delta\theta_K$s for V_G = -1.5, -1, 2, 3 V are displayed in the bottom panel.

4.3.2 Magnetic field dependence

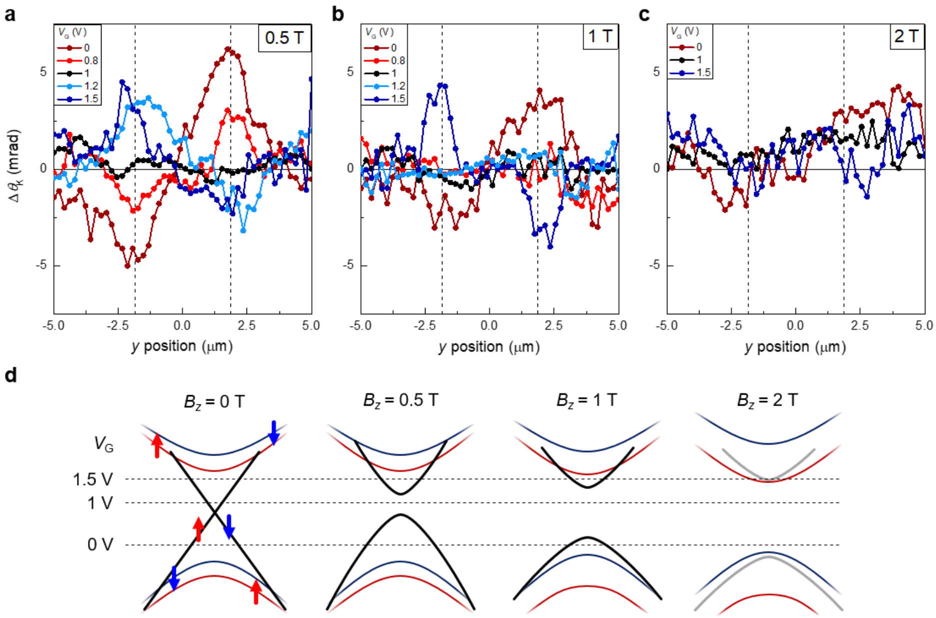

Figure 4.6 B_z-dependent $\Delta\theta_K$ measurement and gap opening of the multilayer WTe_2 due to broken time-reversal symmetry. **a-c.** The line-cut plots show $\Delta\theta_K$ at $x = 0.75$ μm with varying V_G under $B_z = 0.5$ T (**a**), 1 T (**b**), and 2 T (**c**) are shown. $\Delta\theta_K$ is featureless at $V_G = 1$ V when $B_z = 0.5$ T, while it is flat when the applied V_G is $0.8 \text{ V} \leq V_G \leq 1.2$ V under $B_z = 1$ T. Note that no localized $\Delta\theta_K$ behavior is seen at any V_G when $B_z = 2$ T. Dashed lines in a-c at $y = \pm1.85$ μm indicate the y position of the WTe_2 hinges in the real space. **d.** Schematic diagrams explaining the band structures show the effect of B_z on the spin-polarized hinge states (black lines) and spin-split bulk bands (colored lines). Because B_z breaks the time-reversal symmetry, Dirac fermions at the topological hinge states gain an effective mass. This opens a finite energy gap, which is proportional to the magnitude of B_z. The gap opening appears as a flat $\Delta\theta_K$ along y since the Fermi level falls within the gap. The dashed lines in the diagram indicate the Fermi levels when V_G is 0, 1, and 1.5 V. For the case when $B_z = 2$ T (**d**), the schematic represents one possibility that the hinge states are merged into the bulk band due to the induced gap in the hinge states.

As for the HOTI characteristics, the band topology of the multilayer WTe_2 is protected by the time-reversal symmetry. In other words, the degeneracy of hinge states should be lifted without time-reversal symmetry. One method to examine such topological protection using the same experimental regime of the MOKE measurement is to perform the magnetic-field dependent $\Delta\theta_K$ measurements, which can detect the gap opening at the Dirac point due to the broken time-reversal symmetry. Figures 4.6a-c show the line-cut plots of the V_G-dependent $\Delta\theta_K$ along the transversal direction under external magnetic field B_z of 0.5, 1, and 2 T. The B_z was applied perpendicular to the device *xy* plane. In Fig. 4.6a, where B_z is 0.5 T, the $\Delta\theta_K$ signal localized near the hinges vanishes as V_G approaches the charge neutrality. With the increased B_z to 1 T (Fig. 4.6b), the $\Delta\theta_K$ signals near the hinge are more suppressed compared to the case of B_z of 0.5 T, yet the localized $\Delta\theta_K$ survives only when V_G is pushed further below (0 V) and above (1.5 V) the charge neutrality point. When B_z is sufficiently large, Fig. 4.6c shows the vanishing $\Delta\theta_K$ signals, which imply that no spin-polarized electron concentration at any specific location is present. This can be readily understood as the mass gap opening due to the broken time-reversal symmetry[110,111]. The schematic diagrams in Fig. 4.6d show how B_z is expected to affect the gapless dispersion of the helical hinge states with the degenerated Dirac point. When B_z = 0 T, the hinge states remain gapless because the Dirac point is protected by the time-reversal symmetry. In the case of relatively weak B_z (= 0.5, 1 T), the bandgap is created in the hinge states while preserving its spin texture (Figs. 4.6a, b). When a relatively strong B_z of 2 T is applied (Fig. 4.6c), the trace of the hinge disappears. Such disappearance of $\Delta\theta_K$ characteristics when B_z = 2 T may originate from either the merging of hinge states into the bulk band while maintaining the HOTI phase (Fig. 4.6d)[112] or WTe_2 exhibits no HOTI phases with increasing external magnetic fields. A further theoretical and experimental investigation is necessary to elucidate the correlation between the spin texture and the band configuration under strong B_z.

4.3.3 Exclusion of spin Hall effect contribution

The existence of B_z might affect spin-polarized electron transport in alternative ways other than the mass gap opening while exhibiting the same $\Delta\theta_K$ results. First, one plausible explanation would be the QHE induced in WTe_2 accompanied by the chiral boundary. However, B_z used in our experiment is insufficient to generate such an effect[94,113], and the observed V_G-dependent $\Delta\theta_K$ revealed counter-propagating hinge modes that are not consistent with the chiral state characteristics. Second, the effect of B_z on the graphene channel may cause a similar V_G dependence of $\Delta\theta_K$, such as opening a gap at the Dirac point of graphene or causing transverse spin (or valley) flow in graphene. Nevertheless, the Bz used in this study is far smaller than the lower boundary for B_z (~10 T) to observe such effects according to the existing studies[114-116]. Lastly, the recent theoretical study proposed that the broken time-reversal symmetry can be associated with the spatial split of the hinge modes rather than the bandgap opening[111]. While the proposal assumes the specific condition of out-of-plane magnetic flux for the mixture of Zeeman field and boundary states, the B_z applied to the multilayer WTe_2 in this study is perpendicular and parallel to the surfaces interfacing each other at the hinge, respectively. Therefore, considering the non-zero mass and Zeeman contribution to the position away from the hinge, such spatially shifted hinge modes cannot occur between the two surface states.

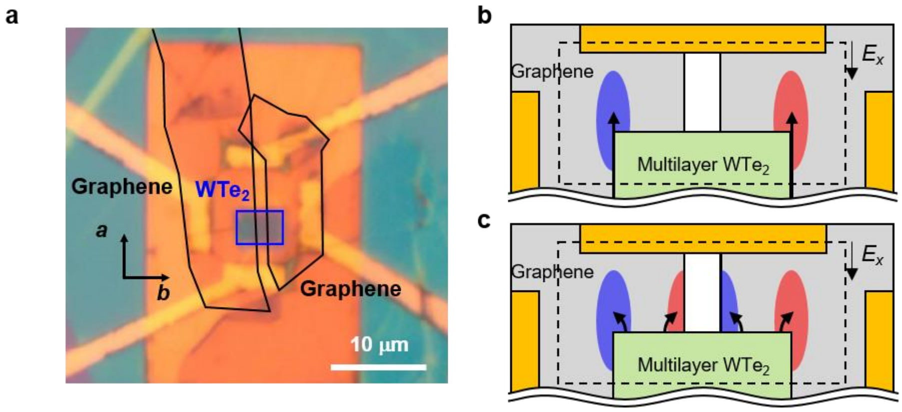

Figure 4.7 Additional experiment proposed to isolate the hinge characteristics (device #4). **a.** An optical microscopy image of device #4 is shown. Two monolayer graphene flakes are separated by a 1.5 μm gap. The graphene layer for the electron transport measurement is located below WTe_2. **b, c.** Schematic representation for the expected $\Delta\theta_K$ distribution when the spin-polarized electrons in graphene originate from the WTe_2 hinge states (**b**) and bulk (**c**). Dashed rectangles are the spatial windows where the MOKE measurements were performed. The black arrows represent electron transport.

The transverse spin accumulation induced in the WTe_2 bulk, e.g., by the SHE, might be a plausible alternative to explain the $\Delta\theta_K$ observed in the experiments. To further substantiate that observed $\Delta\theta_K$ features arise from the spinful hinge state exclusively, a device with the modified structure (device #4) was made for the spatially resolved $\Delta\theta_K$ measurement. Figure 4.7a shows the optical microscopy image of device #4. The graphene layer below the multilayer WTe_2 has a 1.5 μm wide gap along the a-axis of the multilayer WTe_2. The localized $\Delta\theta_K$ should arise only near the WTe_2 hinge if $\Delta\theta_K$ originates from the hinge states as it was expected at first (Fig. 4.7b).

On the other hand, if the observed $\Delta\theta_K$ originates from the bulk spin transport in WTe_2, the spin-polarized electrons in WTe_2 will go through the spin Hall transport and be injected into each graphene (Fig. 4.7c). As a result, the presence of a gap in graphene would collect the accumulated spin-polarized electrons at the edge of graphene on both sides of the gap (Fig. 4.7c).

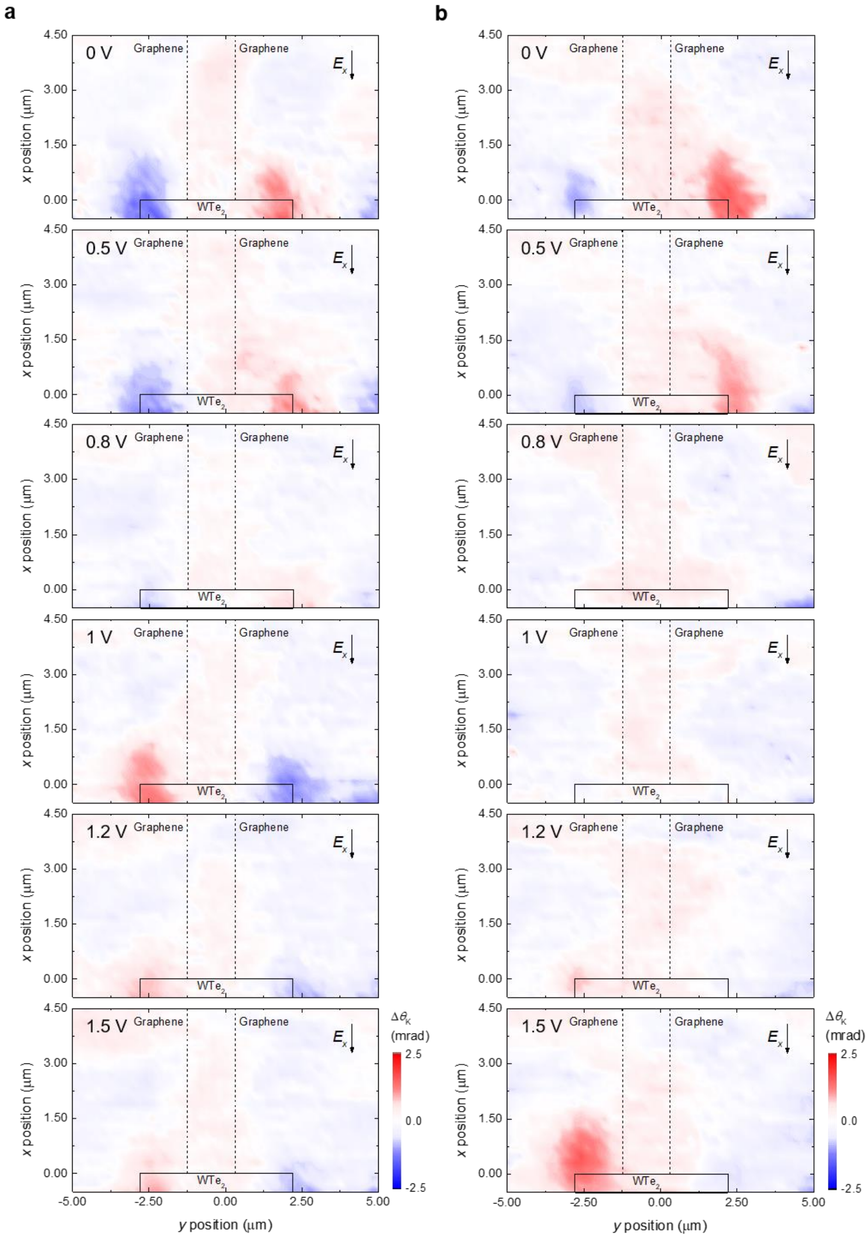

Figure 4.8 The full dataset of spatially resolved V_G-dependent $\Delta\theta_K$ measurement (device #4). 2D contour plots of the V_G-dependent $\Delta\theta_K$ from device #4 when $B_z = 0$ (**a**) and $B_z = 1$ T (**b**). Dashed lines indicate the edge of graphene flakes with the 1.5 μm gap

between them. The black rectangle indicates the location of the top-end part of the multilayer WTe_2. If the spin Hall contribution is the dominant origin of the observed $\Delta\theta_K$, additional peaks and deeps should appear near the dashed line, as described in Fig. 4a. However, the distribution and V_G dependence of $\Delta\theta_K$ is not affected by the existence of a graphene gap.

The V_G-dependent spatially resolved $\Delta\theta_K$ measured in device #4 are shown in Figs. 4.8. The measurements were performed at different V_G with (Fig. 4.8b, B_z = 1 T) and without an external magnetic field (Fig. 4.8a). The first thing to notice is that no accumulation of the spin-polarized electrons was seen on either side of the graphene gap regardless of $V_{G,}$ and $\Delta\theta_K$ appears only in line with the WTe_2 hinges. A clear sign flip of $\Delta\theta_K$ was observed when E_F is swept across the Dirac point of the hinge states, as in the results from device #1. In addition, $\Delta\theta_K$ under the magnetic field shows the gap opening of the hinge states. Under the external magnetic field B_z of 1 T, the localized $\Delta\theta_K$ at the *y*-position of the hinges disappears when the Fermi level is close to the Dirac point (i.e., V_G near 0.88 V in the case of device #4), demonstrating the degeneracy lifting of hinge eigenstates at the Dirac point due to the time-reversal symmetry violation. To summarize, the V_G- and B_z-dependent $\Delta\theta_K$ distribution in device #4 is essentially identical to the devices without the graphene gap (device #1~3). These data provide concrete evidence that SHE in the bulk of multilayer WTe_2 is not likely the origin of our observation.

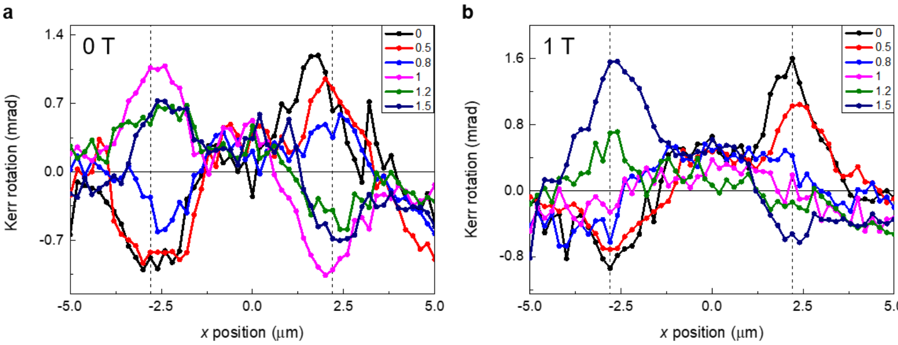

Figure 4.9 Line-cut plot from the spatially resolved V_G-dependent $\Delta\theta_K$ measurement in device #4. The line-cut plots are obtained from the 2D contour plots of $\Delta\theta_K$ at x = 0.3 μm with varying V_G under B_z = 0 T (**a**) and 1 T (**b**), which corresponds to Fig. 4.8a and Fig. 4.8b, respectively. Dashed lines indicate the x position of the WTe_2 hinges in real space. Similar to the result from device #1 (Fig. 4.6), suppression of $\Delta\theta_K$ near the hinge due to the mass gap opening occurs when V_G = 0.8, 1 V.

4.3.4 Supplementary experiments

To supplement the evidences obtained by the V_G- and B_z-dependent $\Delta\theta_K$ measurements, further experiments with new variables were conducted. In the first supplementary experiment using device #1, the temperature dependence of the spin polarization from the hinge and the bulk state was examined to verify the distinction between the two states.

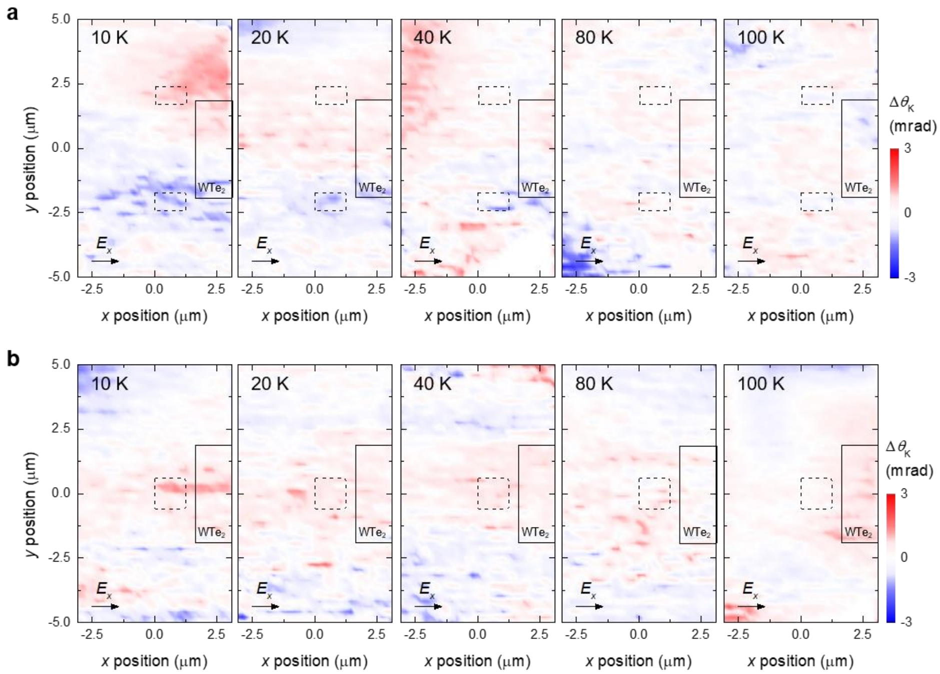

Figure 4.10 The temperature-dependent spatially resolved $\Delta\theta_K$ when V_G = 0 V (**a**) and V_G = 2 V (**b**). No magnetic field was applied. Solid rectangles indicate the location of the left end part of the multilayer WTe_2. Dashed rectangles indicate the area where $|\Delta\theta_K|$ was obtained for each case. The exact positions of the marked area are 0 μm < x < 1.24 μm, 1.7 μm < y < 2.3 μm for **a**, and 0 μm < x < 1.25 μm, $|y|$ < 0.6 μm for **b**.

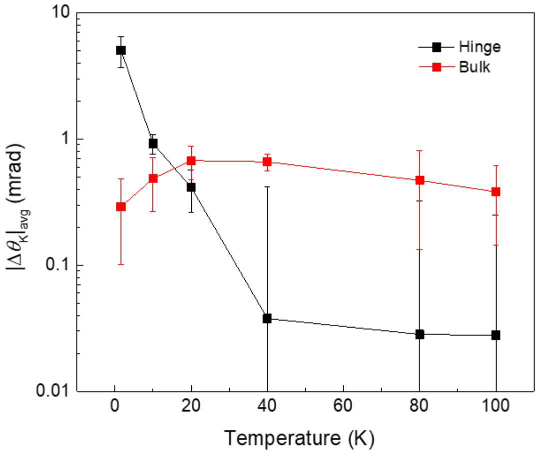

Figure 4.11 Temperature-dependent $|\Delta\theta_K|_{avg}$ obtained from the spatially resolved $\Delta\theta_K$ measurement shown in Fig. 4.10. The error bars indicate the standard variation of the $|\Delta\theta_K|_{avg}$ for each case.

Figure 4.10 shows the temperature-dependent $\Delta\theta_K$ when $V_G = 0$ (a) and 2 V (b), while each corresponds to the case of bulk-insulating and n-doping, respectively. Therefore, $\Delta\theta_K$ in Fig. 4.10a represents the hinge-originating spin polarization, while the spin polarization expressed as $\Delta\theta_K$ in Fig. 4.10b originates from the bulk states. As shown in Fig. 4.10, the spatial localization of $\Delta\theta_K$ for each case is consistent with the origin, and $\Delta\theta_K$ in both cases decreases as the sample temperature rises. For further comparison between the hinge and bulk contribution, the averaged $\Delta\theta_K$ magnitude $|\Delta\theta_K|_{avg}$ in the specific area was calculated (dashed rectangles in Fig. 4.10). Fig. 4.11 shows the summarized temperature dependence of $|\Delta\theta_K|_{avg}$. $|\Delta\theta_K|_{avg}$ of the hinge decreases drastically below the noise level and becomes negligible as the sample temperature rises, while $|\Delta\theta_K|_{avg}$ of the bulk is relatively irrelevant to the temperature change. Such a distinction of the temperature dependence reveals that the observed hinge state is not a simple confinement of the trivial spin-split bulk state or 2D electron gas at the geometric boundary[117,118].

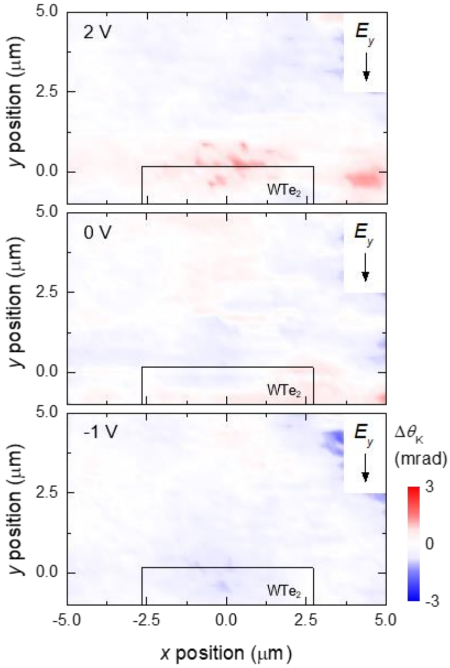

Figure 4.12 Spatially resolved V_G-dependent $\Delta\theta_K$ with the bias voltage of 0.5 V along the *b*-axis. Black rectangles indicate the top-end part of the WTe_2 flake. No magnetic field was applied.

The hinges along the *b*-axis of multilayer WTe_2 were also examined to check the consistency with the previous studies that reported the anisotropic hinge state. Using contact 2 and 4 in device #1, the 0.5 V of bias voltage was applied along the b-axis, and $\Delta\theta_K$ was measured at the graphene near the upper edge of multilayer WTe_2. Figure 4.12 shows the V_G-dependent spatially resolved $\Delta\theta_K$. Unlike Fig. 4.4, which showed localized $\Delta\theta_K$ near the hinge, the localized $\Delta\theta_K$ at the x-position of the hinge was not observed in the case when the longitudinal field was applied along the b-axis. Instead, only bulk-originating $\Delta\theta_K$ was observed at the V_Gs corresponding to the degenerated n- and p-doping of the multilayer WTe_2. The absence of spin-polarized states localized at the hinges suggests the anisotropic nature of the topological hinge state, as argued in prior investigations[97,98]. Moreover, the absence of $\Delta\theta_K$ localized at the x-position of hinges also provides the clue that the transverse spin current induced in the graphene by the SOC proximity effect from the multilayer WTe_2 can be excluded from the possible origin of the observed $\Delta\theta_K$.

4.4 Conclusion and outlook

In conclusion, experimental evidence for the time-reversal invariant helical HOTI phase in the multilayer T_d-WTe_2 was demonstrated through optical measurements on the WTe_2-graphene heterostructure device. The spin polarization of electrons originating from the 1D hinge state of the multilayer WTe_2 was investigated by the spatially resolved MOKE measurement in the heterostructure device. The V_G- and B_z-dependent data provide solid evidence that the helical spin-polarized states are within the bulk bandgap while they are localized at the geometric hinge of the multilayer WTe_2, whose energy degeneracy is protected by the time-reversal symmetry. Because the topologically protected spinful mode is highly confined in the 1D channel, the hinge state of the HOTI may open up a new arena to study the strong correlation and topology in other higher-order topological materials.

CHAPTER 5 – SUMMARY

The optical properties of a condensed matter system often provide valuable information on the interesting quantum mechanics of the material. The optical approach to complex band-related physics has been one of the most challenging subjects, and the technological advancements in laser and material synthesis even accelerated the study of the newly discovered phases of condensed matter.

This thesis describes experimental research focused on the spinful features of the condensed matter systems that host the topological spin transport phenomena. The optical measurements were used as a major tool to investigate the quantum mechanical phenomena, and in particular, the polar MOKE was measured to look into the electron spin polarization under experimental conditions. In addition, peculiarly designed van der Waals heterostructure devices also played a key role in the experiments to overcome the practical limitations of the optical experiment.

Chapter 3 reports the observation of non-excitonic VHE that is induced by the injection of the spin-polarized electron. The VHE in 2D van der Waals crystals is a promising approach to studying the valley pseudospin. Most experiments so far have used bound excitons through local photoexcitation. However, the valley depolarization of such excitons is fast, so several challenges remain to be resolved. We address this issue by exploiting a unipolar VHE using a heterobilayer made of monolayer MoS_2/WTe_2 to exhibit a long valley-polarized lifetime due to the absence of electron-hole exchange interaction. The unipolar VHE is manifested by reduced photoluminescence at the MoS_2 A exciton energy. Furthermore, we provide quantitative information on the time-dependent valley Hall dynamics by performing the spatially-resolved ultrafast Kerr-rotation microscopy; we find that the valley-polarized electrons persist for more than 4 nanoseconds and the valley Hall mobility exceeds 4.49×10^3 cm^2/Vs, which is orders of magnitude larger than previous reports.

In Chapter 4, we discussed the spinful nature of the hinge states in the multilayer T_d-WTe_2, a HOTI. Higher-order topological insulators are recently discovered quantum materials exhibiting distinct topological phases with generalized bulk-boundary correspondence. T_d-WTe_2, a non-centrosymmetric type-II Weyl semimetal, is a promising candidate to reveal topological hinge excitation in an atomically thin regime. However, with initial theories and experiments focusing on localized one-dimensional conductance only, no experimental reports exist on how the spin orientations are distributed over the helical hinges—this is critical, yet one missing puzzle. Here, we employ the magneto-optic Kerr effect to visualize the spinful characteristics of the hinge states in a few-layer T_d-WTe_2. By examining the spin polarization of electrons injected from WTe_2 to graphene under external electric and magnetic fields, we conclude that WTe_2 hosts a spinful and helical topological hinge state protected by the time-reversal symmetry. Our experiment provides a fertile diagnosis to investigate the topologically protected gapless hinge states and may call for new theoretical studies to extend the previous spinless model.

To summarize, optical measurements on van der Waals heterostructure devices consisting of topological materials revealed the spin dynamics and existence of the topologically protected spinful states hidden by the trivial phenomena. A comprehensive optical experiment system was built for consistent and precise measurements. Besides, detailed procedures and hardware for optimal device manufacturing were also built. Based on these efforts, the MOKE observation under carrier injection regime realized by a specially designed heterostructure device was used in both studies of VHE and HOTI. As a result, the exciton-free VHE and spinful hinge states of the multilayer WTe_2 were successfully characterized. In addition to a better understanding of topological spin transport, I was able to achieve methodological development in optically detecting the spinful effects covered in trivial backgrounds.

BIBLIOGRAPHY

1 Thouless, D. J., Kohmoto, M., Nightingale, M. P. & den Nijs, M. Quantized Hall Conductance in a Two-Dimensional Periodic Potential. *Physical Review Letters* **49**, 405-408, doi:10.1103/PhysRevLett.49.405 (1982).

2 Laughlin, R. B. Quantized Hall conductivity in two dimensions. *Physical Review B* **23**, 5632-5633, doi:10.1103/PhysRevB.23.5632 (1981).

3 Thouless, D. J. Quantization of particle transport. *Physical Review B* **27**, 6083-6087, doi:10.1103/PhysRevB.27.6083 (1983).

4 Wen, X.-G. Topological orders and edge excitations in fractional quantum Hall states. *Advances in Physics* **44**, 405-473, doi:10.1080/00018739500101566 (1995).

5 Chen, X., Ma, X.-C., He, K., Jia, J.-F. & Xue, Q.-K. Molecular Beam Epitaxial Growth of Topological Insulators. *Advanced Materials* **23**, 1162-1165, doi:https://doi.org/10.1002/adma.201003855 (2011).

6 Kim, D. *et al.* Surface conduction of topological Dirac electrons in bulk insulating Bi2Se3. *Nature Physics* **8**, 459-463, doi:10.1038/nphys2286 (2012).

7 Taskin, A. A. & Ando, Y. Berry phase of nonideal Dirac fermions in topological insulators. *Physical Review B* **84**, 035301, doi:10.1103/PhysRevB.84.035301 (2011).

8 Checkelsky, J. G. *et al.* Quantum Interference in Macroscopic Crystals of Nonmetallic Bi_2Se_3. *Physical Review Letters* **103**, 246601, doi:10.1103/PhysRevLett.103.246601 (2009).

9 Hsieh, D. *et al.* Observation of unconventional quantum spin textures in topological insulators. *Science* **323**, 919-922 (2009).

10 Chen, Y. *et al.* Experimental realization of a three-dimensional topological insulator, Bi2Te3. *Science* **325**, 178-181 (2009).

11 Wang, J. *et al.* Evidence for electron-electron interaction in topological insulator thin films. *Physical Review B* **83**, 245438, doi:10.1103/PhysRevB.83.245438 (2011).

12 McIver, J. W., Hsieh, D., Steinberg, H., Jarillo-Herrero, P. & Gedik, N. Control over topological insulator photocurrents with light polarization. *Nature Nanotechnology* **7**, 96-100, doi:10.1038/nnano.2011.214 (2012).

13 Hsieh, D. *et al.* Nonlinear Optical Probe of Tunable Surface Electrons on a Topological Insulator. *Physical Review Letters* **106**, 057401, doi:10.1103/PhysRevLett.106.057401 (2011).

14 Schafgans, A. A. *et al.* Landau level spectroscopy of surface states in the topological insulator $Bi_{0.91}Sb_{0.09}$ via magneto-optics. *Physical Review B* **85**, 195440, doi:10.1103/PhysRevB.85.195440 (2012).

15 Di Pietro, P. *et al.* Observation of Dirac plasmons in a topological insulator. *Nature Nanotechnology* **8**, 556-560, doi:10.1038/nnano.2013.134 (2013).

16 Karch, A. Surface plasmons and topological insulators. *Physical Review B* **83**, 245432, doi:10.1103/PhysRevB.83.245432 (2011).

17 Sobota, J. A. *et al.* Ultrafast Optical Excitation of a Persistent Surface-State Population in the Topological Insulator Bi_2Se_3. *Physical Review Letters* **108**, 117403, doi:10.1103/PhysRevLett.108.117403 (2012).

18 Wang, Y. H. *et al.* Measurement of Intrinsic Dirac Fermion Cooling on the Surface of the Topological Insulator Bi_2Se_3 Using Time-Resolved and Angle-Resolved Photoemission Spectroscopy. *Physical Review Letters* **109**, 127401, doi:10.1103/PhysRevLett.109.127401 (2012).

19 Onishi, Y. *et al.* Ultrafast carrier relaxation through Auger recombination in the topological insulator $Bi_{1.5}Sb_{0.5}Te_{1.7}Se_{1.3}$. *Physical Review B* **91**, 085306 (2015).

20 Klitzing, K. v., Dorda, G. & Pepper, M. New Method for High-Accuracy Determination of the Fine-Structure Constant Based on Quantized Hall Resistance. *Physical Review Letters* **45**, 494-497, doi:10.1103/PhysRevLett.45.494 (1980).

21 Haldane, F. D. M. Model for a Quantum Hall Effect without Landau Levels: Condensed-Matter Realization of the "Parity Anomaly". *Physical Review Letters* **61**, 2015-2018, doi:10.1103/PhysRevLett.61.2015 (1988).

22 Jackiw, R. & Rebbi, C. Solitons with fermion number 1/2. *Physical Review D* **13**, 3398-3409, doi:10.1103/PhysRevD.13.3398 (1976).

23 Hasan, M. Z. & Kane, C. L. Colloquium: Topological insulators. *Reviews of Modern Physics* **82**, 3045-3067, doi:10.1103/RevModPhys.82.3045 (2010).

24 Kane, C. L. & Mele, E. J. Quantum Spin Hall Effect in Graphene. *Physical Review Letters* **95**, 226801, doi:10.1103/PhysRevLett.95.226801 (2005).

25 Bernevig, B. A., Hughes, T. L. & Zhang, S.-C. Quantum Spin Hall Effect and Topological Phase Transition in HgTe Quantum Wells. *Science* **314**, 1757-1761, doi:doi:10.1126/science.1133734 (2006).

26 Hsieh, T. H. *et al.* Topological crystalline insulators in the SnTe material class. *Nature Communications* **3**, 982, doi:10.1038/ncomms1969 (2012).

27 Zhang, H. *et al.* Topological insulators in Bi_2Se_3, Bi_2Te_3 and Sb_2Te_3 with a single Dirac cone on the surface. *Nature Physics* **5**, 438-442, doi:10.1038/nphys1270 (2009).

28 Schindler, F. *et al.* Higher-order topological insulators. *Science Advances* **4**, eaat0346, doi:doi:10.1126/sciadv.aat0346 (2018).

29 Benalcazar, W. A., Bernevig, B. A. & Hughes, T. L. Quantized electric multipole insulators. *Science* **357**, 61-66, doi:doi:10.1126/science.aah6442 (2017).

30 Wang, Z., Wieder, B. J., Li, J., Yan, B. & Bernevig, B. A. Higher-Order Topology, Monopole Nodal Lines, and the Origin of Large Fermi Arcs in Transition Metal Dichalcogenides $X\mathrm{Te}_2$ (X = Mo, W). *Physical Review Letters* **123**, 186401, doi:10.1103/PhysRevLett.123.186401 (2019).

31 Armitage, N. P., Mele, E. J. & Vishwanath, A. Weyl and Dirac semimetals in three-dimensional solids. *Reviews of Modern Physics* **90**, 015001, doi:10.1103/RevModPhys.90.015001 (2018).

32 Schindler, F. *et al.* Higher-order topology in bismuth. *Nature Physics* **14**, 918-924, doi:10.1038/s41567-018-0224-7 (2018).

33 Noguchi, R. *et al.* Evidence for a higher-order topological insulator in a three-dimensional material built from van der Waals stacking of bismuth-halide chains. *Nature Materials* **20**, 473-479, doi:10.1038/s41563-020-00871-7 (2021).

34 Tang, F., Po, H. C., Vishwanath, A. & Wan, X. Efficient topological materials discovery using symmetry indicators. *Nature Physics* **15**, 470-476, doi:10.1038/s41567-019-0418-7 (2019).

35 Park, M. J., Kim, Y., Cho, G. Y. & Lee, S. Higher-Order Topological Insulator in Twisted Bilayer Graphene. *Physical Review Letters* **123**, 216803, doi:10.1103/PhysRevLett.123.216803 (2019).

36 Chang, C.-Z. & Li, M. Quantum anomalous Hall effect in time-reversal-symmetry breaking topological insulators. *Journal of Physics: Condensed Matter* **28**, 123002 (2016).

37 Nagaosa, N., Sinova, J., Onoda, S., MacDonald, A. H. & Ong, N. P. Anomalous Hall effect. *Reviews of Modern Physics* **82**, 1539-1592, doi:10.1103/RevModPhys.82.1539 (2010).

38 Sinitsyn, N. A., MacDonald, A. H., Jungwirth, T., Dugaev, V. K. & Sinova, J. Anomalous Hall effect in a two-dimensional Dirac band: The link between the Kubo-Streda formula and the semiclassical Boltzmann equation approach. *Physical Review B* **75**, 045315, doi:10.1103/PhysRevB.75.045315 (2007).

39 Berger, L. Side-Jump Mechanism for the Hall Effect of Ferromagnets. *Physical Review B* **2**, 4559-4566, doi:10.1103/PhysRevB.2.4559 (1970).

40 Weischenberg, J., Freimuth, F., Sinova, J., Blügel, S. & Mokrousov, Y. Ab Initio Theory of the Scattering-Independent Anomalous Hall Effect. *Physical Review Letters* **107**, 106601, doi:10.1103/PhysRevLett.107.106601 (2011).

41 Sinova, J. *et al.* Universal Intrinsic Spin Hall Effect. *Physical Review Letters* **92**, 126603, doi:10.1103/PhysRevLett.92.126603 (2004).

42 Sinova, J., Valenzuela, S. O., Wunderlich, J., Back, C. H. & Jungwirth, T. Spin Hall effects. *Reviews of Modern Physics* **87**, 1213-1260, doi:10.1103/RevModPhys.87.1213 (2015).

43 Kato, Y. K., Myers, R. C., Gossard, A. C. & Awschalom, D. D. Observation of the Spin Hall Effect in Semiconductors. *Science* **306**, 1910-1913, doi:doi:10.1126/science.1105514 (2004).

44 Ando, K. *et al.* Photoinduced inverse spin-Hall effect: Conversion of light-polarization information into electric voltage. *Applied Physics Letters* **96**, 082502 (2010).

45 Olejník, K. *et al.* Detection of Electrically Modulated Inverse Spin Hall Effect in an Fe / GaAs Microdevice. *Physical Review Letters* **109**, 076601, doi:10.1103/PhysRevLett.109.076601 (2012).

46 Garlid, E. S., Hu, Q. O., Chan, M. K., Palmstrøm, C. J. & Crowell, P. A. Electrical Measurement of the Direct Spin Hall Effect in Fe / $In_xGa_{1-x}As$ Heterostructures. *Physical Review Letters* **105**, 156602, doi:10.1103/PhysRevLett.105.156602 (2010).

47 Torres, W. S. *et al.* Spin precession and spin Hall effect in monolayer graphene/Pt nanostructures. *2D Materials* **4**, 041008 (2017).

48 Safeer, C. *et al.* Room-temperature spin Hall effect in graphene/MoS_2 van der Waals heterostructures. *Nano letters* **19**, 1074-1082 (2019).

49 Zhu, C. R. *et al.* Exciton valley dynamics probed by Kerr rotation in WSe_2 monolayers. *Physical Review B* **90**, 161302, doi:10.1103/PhysRevB.90.161302 (2014).

50 Dey, P. *et al.* Gate-Controlled Spin-Valley Locking of Resident Carriers in WSe_2 Monolayers. *Physical Review Letters* **119**, 137401, doi:10.1103/PhysRevLett.119.137401 (2017).

51 Tse, W.-K. & MacDonald, A. H. Giant Magneto-Optical Kerr Effect and Universal Faraday Effect in Thin-Film Topological Insulators. *Physical Review Letters* **105**, 057401, doi:10.1103/PhysRevLett.105.057401 (2010).

52 Xiao, D., Liu, G.-B., Feng, W., Xu, X. & Yao, W. Coupled Spin and Valley Physics in Monolayers of MoS_2 and Other Group-VI Dichalcogenides. *Physical Review Letters* **108**, 196802, doi:10.1103/PhysRevLett.108.196802 (2012).

53 Xiao, D., Chang, M.-C. & Niu, Q. Berry phase effects on electronic properties. *Reviews of Modern Physics* **82**, 1959-2007, doi:10.1103/RevModPhys.82.1959 (2010).

54 Xiao, D., Yao, W. & Niu, Q. Valley-Contrasting Physics in Graphene: Magnetic Moment and Topological Transport. *Physical Review Letters* **99**, 236809, doi:10.1103/PhysRevLett.99.236809 (2007).

55 Mak, K. F., McGill, K. L., Park, J. & McEuen, P. L. The valley Hall effect in MoS_2 transistors. *Science* **344**, 1489-1492, doi:doi:10.1126/science.1250140 (2014).

56 Gorbachev, R. V. *et al.* Detecting topological currents in graphene superlattices. *Science* **346**, 448-451, doi:doi:10.1126/science.1254966 (2014).

57 Sui, M. *et al.* Gate-tunable topological valley transport in bilayer graphene. *Nature Physics* **11**, 1027-1031, doi:10.1038/nphys3485 (2015).

58 Mak, K. F., He, K., Shan, J. & Heinz, T. F. Control of valley polarization in monolayer MoS_2 by optical helicity. *Nature Nanotechnology* **7**, 494-498, doi:10.1038/nnano.2012.96 (2012).

59 Lee, J., Mak, K. F. & Shan, J. Electrical control of the valley Hall effect in bilayer MoS_2 transistors. *Nature Nanotechnology* **11**, 421-425, doi:10.1038/nnano.2015.337 (2016).

60 Yu, T. & Wu, M. W. Valley depolarization dynamics and valley Hall effect of excitons in monolayer and bilayer MoS_2. *Physical Review B* **93**, 045414, doi:10.1103/PhysRevB.93.045414 (2016).

61 Hao, K. *et al.* Direct measurement of exciton valley coherence in monolayer WSe_2. *Nature Physics* **12**, 677-682, doi:10.1038/nphys3674 (2016).

62 Wang, G. *et al.* Colloquium: Excitons in atomically thin transition metal dichalcogenides. *Reviews of Modern Physics* **90**, 021001, doi:10.1103/RevModPhys.90.021001 (2018).

63 Jin, C. *et al.* Imaging of pure spin-valley diffusion current in WS_2-WSe_2 heterostructures. *Science* **360**, 893-896, doi:doi:10.1126/science.aao3503 (2018).

64 Kim, J. *et al.* Observation of ultralong valley lifetime in WSe_2/MoS_2 heterostructures. *Science Advances* **3**, e1700518, doi:doi:10.1126/sciadv.1700518 (2017).

65 Hung, T. Y. T., Camsari, K. Y., Zhang, S., Upadhyaya, P. & Chen, Z. Direct observation of valley-coupled topological current in MoS_2. *Science Advances* **5**, eaau6478, doi:doi:10.1126/sciadv.aau6478 (2019).

66 Fei, Z. *et al.* Edge conduction in monolayer WTe_2. *Nature Physics* **13**, 677-682, doi:10.1038/nphys4091 (2017).

67 Tang, S. *et al.* Quantum spin Hall state in monolayer 1T'-WTe_2. *Nature Physics* **13**, 683-687, doi:10.1038/nphys4174 (2017).

68 Cui, X. *et al.* Multi-terminal transport measurements of MoS_2 using a van der Waals heterostructure device platform. *Nature Nanotechnology* **10**, 534-540, doi:10.1038/nnano.2015.70 (2015).

69 Onga, M., Zhang, Y., Ideue, T. & Iwasa, Y. Exciton Hall effect in monolayer MoS_2. *Nature Materials* **16**, 1193-1197, doi:10.1038/nmat4996 (2017).

70 Mak, K. F. *et al.* Tightly bound trions in monolayer MoS_2. *Nature Materials* **12**, 207-211, doi:10.1038/nmat3505 (2013).

71 Koschorreck, M. *et al.* Attractive and repulsive Fermi polarons in two dimensions. *Nature* **485**, 619-622, doi:10.1038/nature11151 (2012).

72 Schneider, C., Glazov, M. M., Korn, T., Höfling, S. & Urbaszek, B. Two-dimensional semiconductors in the regime of strong light-matter coupling. *Nature Communications* **9**, 2695, doi:10.1038/s41467-018-04866-6 (2018).

73 Yan, T., Yang, S., Li, D. & Cui, X. Long valley relaxation time of free carriers in monolayer WSe_2. *Physical Review B* **95**, 241406, doi:10.1103/PhysRevB.95.241406 (2017).

74 Yan, T., Ye, J., Qiao, X., Tan, P. & Zhang, X. Exciton valley dynamics in monolayer WSe_2 probed by the two-color ultrafast Kerr rotation. *Physical Chemistry Chemical Physics* **19**, 3176-3181, doi:10.1039/C6CP07208A (2017).

75 Ye, Z., Sun, D. & Heinz, T. F. Optical manipulation of valley pseudospin. *Nature Physics* **13**, 26-29, doi:10.1038/nphys3891 (2017).

76 Jin, C. *et al.* Identification of spin, valley and moiré quasi-angular momentum of interlayer excitons. *Nature Physics* **15**, 1140-1144, doi:10.1038/s41567-019-0631-4 (2019).

77 Schaibley, J. R. *et al.* Directional interlayer spin-valley transfer in two-dimensional heterostructures. *Nature Communications* **7**, 13747, doi:10.1038/ncomms13747 (2016).

78 Rivera, P. *et al.* Observation of long-lived interlayer excitons in monolayer $MoSe_2$–WSe_2 heterostructures. *Nature Communications* **6**, 6242, doi:10.1038/ncomms7242 (2015).

79 Chen, H. *et al.* Ultrafast formation of interlayer hot excitons in atomically thin MoS_2/WS_2 heterostructures. *Nature Communications* **7**, 12512, doi:10.1038/ncomms12512 (2016).

80 Borunda, M. *et al.* Absence of Skew Scattering in Two-Dimensional Systems: Testing the Origins of the Anomalous Hall Effect. *Physical Review Letters* **99**, 066604, doi:10.1103/PhysRevLett.99.066604 (2007).

81 Marinov, K., Avsar, A., Watanabe, K., Taniguchi, T. & Kis, A. Resolving the spin splitting in the conduction band of monolayer MoS_2. *Nature Communications* **8**, 1938, doi:10.1038/s41467-017-02047-5 (2017).

82 Wu, Z. *et al.* Intrinsic valley Hall transport in atomically thin MoS_2. *Nature Communications* **10**, 611, doi:10.1038/s41467-019-08629-9 (2019).

83 Yang, L. *et al.* Long-lived nanosecond spin relaxation and spin coherence of electrons in monolayer MoS_2 and WS_2. *Nature Physics* **11**, 830-834, doi:10.1038/nphys3419 (2015).

84 Song, X., Xie, S., Kang, K., Park, J. & Sih, V. Long-Lived Hole Spin/Valley Polarization Probed by Kerr Rotation in Monolayer WSe_2. *Nano Letters* **16**, 5010-5014, doi:10.1021/acs.nanolett.6b01727 (2016).

85 Benalcazar, W. A., Bernevig, B. A. & Hughes, T. L. Electric multipole moments, topological multipole moment pumping, and chiral hinge states in crystalline insulators. *Physical Review B* **96**, 245115, doi:10.1103/PhysRevB.96.245115 (2017).

86 Ezawa, M. Second-order topological insulators and loop-nodal semimetals in Transition Metal Dichalcogenides XTe_2 (X = Mo, W). *Scientific Reports* **9**, 5286, doi:10.1038/s41598-019-41746-5 (2019).

87 Ahn, J., Park, S. & Yang, B.-J. Failure of Nielsen-Ninomiya Theorem and Fragile Topology in Two-Dimensional Systems with Space-Time Inversion Symmetry: Application to Twisted Bilayer Graphene at Magic Angle. *Physical Review X* **9**, 021013, doi:10.1103/PhysRevX.9.021013 (2019).

88 Liu, B. *et al.* Higher-Order Band Topology in Twisted Moiré Superlattice. *Physical Review Letters* **126**, 066401, doi:10.1103/PhysRevLett.126.066401 (2021).

89 Kempkes, S. N. *et al.* Robust zero-energy modes in an electronic higher-order topological insulator. *Nature Materials* **18**, 1292-1297, doi:10.1038/s41563-019-0483-4 (2019).

90 Ezawa, M. Higher-Order Topological Insulators and Semimetals on the Breathing Kagome and Pyrochlore Lattices. *Physical Review Letters* **120**, 026801, doi:10.1103/PhysRevLett.120.026801 (2018).

91 Sun, B. *et al.* Evidence for equilibrium exciton condensation in monolayer WTe_2. *Nature Physics* **18**, 94-99, doi:10.1038/s41567-021-01427-5 (2022).

92 Wang, P. *et al.* One-dimensional Luttinger liquids in a two-dimensional moiré lattice. *Nature* **605**, 57-62, doi:10.1038/s41586-022-04514-6 (2022).

93 Soluyanov, A. A. *et al.* Type-II Weyl semimetals. *Nature* **527**, 495-498, doi:10.1038/nature15768 (2015).

94 Li, P. *et al.* Evidence for topological type-II Weyl semimetal WTe_2. *Nature Communications* **8**, 2150, doi:10.1038/s41467-017-02237-1 (2017).

95 Deng, K. *et al.* Experimental observation of topological Fermi arcs in type-II Weyl semimetal $MoTe_2$. *Nature Physics* **12**, 1105-1110, doi:10.1038/nphys3871 (2016).

96 Wang, C. *et al.* Observation of Fermi arc and its connection with bulk states in the candidate type-II Weyl semimetal WTe_2. *Physical Review B* **94**, 241119, doi:10.1103/PhysRevB.94.241119 (2016).

97 Choi, Y.-B. *et al.* Evidence of higher-order topology in multilayer WTe_2 from Josephson coupling through anisotropic hinge states. *Nature Materials* **19**, 974-979, doi:10.1038/s41563-020-0721-9 (2020).

98 Kononov, A. *et al.* One-Dimensional Edge Transport in Few-Layer WTe_2. *Nano Letters* **20**, 4228-4233, doi:10.1021/acs.nanolett.0c00658 (2020).

99 Xie, B. *et al.* Higher-order band topology. *Nature Reviews Physics* **3**, 520-532, doi:10.1038/s42254-021-00323-4 (2021).

100 Das, P. K. *et al.* Layer-dependent quantum cooperation of electron and hole states in the anomalous semimetal WTe_2. *Nature Communications* **7**, 10847, doi:10.1038/ncomms10847 (2016).

101 Fanciulli, M. *et al.* Spin, time, and angle resolved photoemission spectroscopy on WTe_2. *Physical Review Research* **2**, 013261, doi:10.1103/PhysRevResearch.2.013261 (2020).

102 Das, P. *et al.* Electronic properties of candidate type-II Weyl semimetal WTe_2. A review perspective. *Electronic Structure* **1**, 014003 (2019).

103 Tiwari, A. *et al.* Giant c-axis nonlinear anomalous Hall effect in Td-$MoTe_2$ and WTe_2. *Nature Communications* **12**, 2049, doi:10.1038/s41467-021-22343-5 (2021).

104 Fiori, G. *et al.* Electronics based on two-dimensional materials. *Nature Nanotechnology* **9**, 768-779, doi:10.1038/nnano.2014.207 (2014).

105 Cusati, T. *et al.* Electrical properties of graphene-metal contacts. *Scientific Reports* **7**, 5109, doi:10.1038/s41598-017-05069-7 (2017).

106 Xu, S.-Y. *et al.* Electrically switchable Berry curvature dipole in the monolayer topological insulator WTe_2. *Nature Physics* **14**, 900-906, doi:10.1038/s41567-018-0189-6 (2018).

107 Bolotin, K. I., Sikes, K. J., Hone, J., Stormer, H. L. & Kim, P. Temperature-Dependent Transport in Suspended Graphene. *Physical Review Letters* **101**, 096802, doi:10.1103/PhysRevLett.101.096802 (2008).

108 Laturia, A., Van de Put, M. L. & Vandenberghe, W. G. Dielectric properties of hexagonal boron nitride and transition metal dichalcogenides: from monolayer to bulk. *npj 2D Materials and Applications* **2**, 6, doi:10.1038/s41699-018-0050-x (2018).

109 Wang, Y. *et al.* Direct Evidence for Charge Compensation-Induced Large Magnetoresistance in Thin WTe_2. *Nano Letters* **19**, 3969-3975, doi:10.1021/acs.nanolett.9b01275 (2019).

110 Rosenberg, G. & Franz, M. Surface magnetic ordering in topological insulators with bulk magnetic dopants. *Physical Review B* **85**, 195119, doi:10.1103/PhysRevB.85.195119 (2012).

111 Queiroz, R. & Stern, A. Splitting the Hinge Mode of Higher-Order Topological Insulators. *Physical Review Letters* **123**, 036802, doi:10.1103/PhysRevLett.123.036802 (2019).

112 Otaki, Y. & Fukui, T. Higher-order topological insulators in a magnetic field. *Physical Review B* **100**, 245108, doi:10.1103/PhysRevB.100.245108 (2019).

113 Wang, P. *et al.* Landau quantization and highly mobile fermions in an insulator. *Nature* **589**, 225-229, doi:10.1038/s41586-020-03084-9 (2021).

114 Castro Neto, A. H., Guinea, F., Peres, N. M. R., Novoselov, K. S. & Geim, A. K. The electronic properties of graphene. *Reviews of Modern Physics* **81**, 109-162, doi:10.1103/RevModPhys.81.109 (2009).

115 Das Sarma, S., Adam, S., Hwang, E. H. & Rossi, E. Electronic transport in two-dimensional graphene. *Reviews of Modern Physics* **83**, 407-470, doi:10.1103/RevModPhys.83.407 (2011).

116 Settnes, M., Garcia, J. H. & Roche, S. Valley-polarized quantum transport generated by gauge fields in graphene. *2D Materials* **4**, 031006 (2017).

117 Thoutam, L. R. *et al.* Temperature-Dependent Three-Dimensional Anisotropy of the Magnetoresistance in WTe_2. *Physical Review Letters* **115**, 046602, doi:10.1103/PhysRevLett.115.046602 (2015).

118 Wu, S. *et al.* Observation of the quantum spin Hall effect up to 100 kelvin in a monolayer crystal. *Science* **359**, 76-79, doi:doi:10.1126/science.aan6003 (2018).

APPENDIX A - DIELECTRIC PERMITTIVITY TENSOR

In Chapter 2, the theoretical background of MOKE was explained based on the magnetic circular dichroism. There, refraction indices $n_{\pm}$ was expressed in terms of the first- and second-order effects of magnetization ($\xi \propto M_0$ and $n_{\perp}^2 \propto M_0^2$, respectively) for the circularly polarized normal modes were used to explain the magnetic circular dichroism in magnetic materials. Such a magneto-optical effect is derived from the time-reversal operation on the dielectric permittivity tensor. In the magnetically non-ordered lossless materials, the dielectric permittivity tensor is Hermitian $\epsilon_{ij}(\omega, H_0) = \epsilon_{ji}^*(\omega, -H_0)$ and the time-reversal transformation yields

$$\epsilon_{ij}(\omega_0, H_0) = \epsilon_{ji}(\omega_0, -H_0) \quad \text{(A1)}$$

when the external magnetic field H_0 is applied to the material. Note that the real and imaginary parts of permittivity follow the same time-reversal operation relation in Eq. A1. Therefore, the general expression of dielectric permittivity as a function of H_0 can be written as

$$\epsilon_{ij}(H_0) = \epsilon_{ij} + \Delta\epsilon_{ij}(H_0) = \epsilon_{ij} + i\epsilon_0 \sum_k f_{ijk} H_{0k} + \epsilon_0 \sum_{k,l} c_{ijkl} H_{0k} H_{0l} + \cdots, \quad \text{(A2)}$$

where f_{ijk} and c_{ijkl} are real parameters that $f_{ijk} = -f_{jik}$ and $c_{ijkl} = c_{jikl} = c_{ijlk} = c_{jilk}$. If the material is isotropic and three-dimensional, the matrix expression of the dielectric permittivity under the magnetic field $\boldsymbol{H}_0 = H_{0z}\hat{z}$ yields

$$\boldsymbol{\epsilon}(\boldsymbol{H}_0) = \epsilon_0 \begin{bmatrix} n_o^2 + c_{1133} H_{0z}^2 & if H_{0z} & 0 \\ -if H_{0z} & n_o^2 + c_{2233} H_{0z}^2 & 0 \\ 0 & 0 & n_e^2 + c_{3333} H_{0z}^2 \end{bmatrix}. \quad \text{(A3)}$$

where n_o and n_e are refractive index orthogonal and parallel to the external field.

In magnetic materials that have magnetization $\boldsymbol{M}_0$, $\boldsymbol{M}_0$ replaces the role of H_0 in the magneto-optical effects. For $\boldsymbol{M}_0 = M_{0z}\hat{z}$, $\boldsymbol{\epsilon}(\boldsymbol{M}_0)$ is expressed as

$$\boldsymbol{\epsilon}(\boldsymbol{M}_0) = \epsilon_0 \begin{bmatrix} n_\perp^2 & i\xi & 0 \\ -i\xi & n_\perp^2 & 0 \\ 0 & 0 & n_\parallel^2 \end{bmatrix}, \quad \text{(A4)}$$

having ξ as a first-order effect of $\boldsymbol{M}_0$ and $n_\perp^2$, $n_\parallel^2$ as second-order components. Here, the antisymmetric off-diagonal components related to the first-order parameter are responsible for the magnetic circular dichroism explained in Chapter 2, eventually causing the magneto-optical Kerr effect.

APPENDIX B - SUPPLEMENTARY DATA FOR CHAPTER 3

B.1 Extended dataset - spatially resolved Kerr rotation

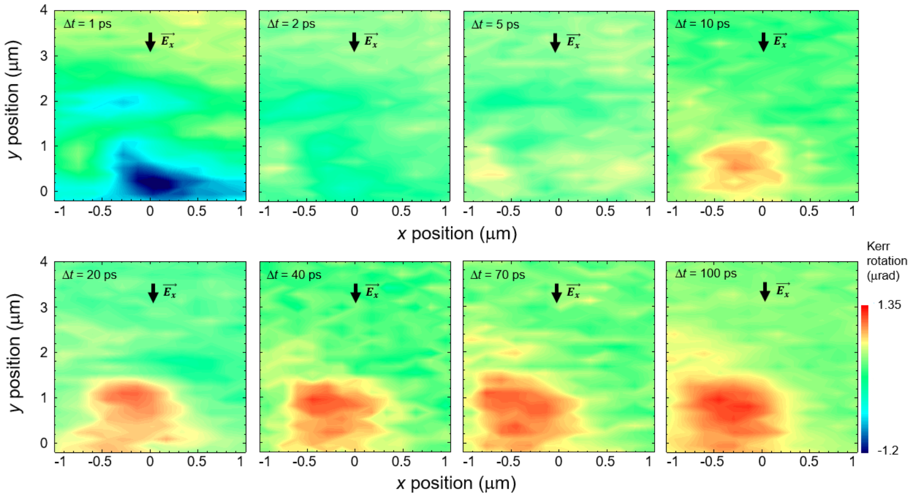

Figure B1. Full set of spatially resolved Kerr rotation data at Δ*t* = 1, 2, 5, 10, 20, 40, 70, and 100 ps.

In Fig. 3.7, the snapshot contour plots of spatially resolved Kerr rotation for a few representative Δt were presented (Δt = 5, 20, 100 ps). The extended dataset shown in Fig. B1 includes the spatially resolved Kerr rotation at Δt = 1, 2, 10, 40, and 70 ps when V_G = 2 V and the helicity of the remote pump is σ^+. The transversal transport of the valley polarization over time is expressed as the shift of the Kerr rotation peak in each panel. At Δt = 1 ps, the negative Kerr rotation is observed near the remote pump. Such a short-lasing negative peak was observed in transient θ_K measurements, showing the possibility that the indirect excitation of MoS_2 or rapid charge transfer between MoS_2 and WTe_2 induces temporal valley-polarized hole concentration localized at the region near the remote pump, considering that the θ_K by valley-polarized holes has opposite sign compared to the θ_K by valley-polarized electrons.

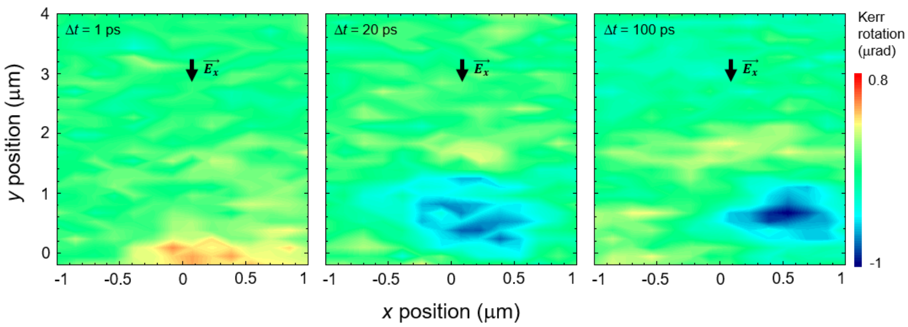

Figure B2. Spatially resolved Kerr rotation at Δt = 1, 20, 100 ps when the helicity of the remote pump is σ^- (contrary to the case shown in Fig. B1).

As a control experiment, the spatially resolved θ_K with the remote pump of σ^- helicity was also measured. Figure B2 shows the resultant 2D contour plots of spatially resolved θ_K when Δt = 1, 20, and 100 ps. The experimental conditions other than the helicity of the remote pump, i.e., V_G, E_x, remained unchanged. The transversal shift of the θ_K over time has an opposite direction compared to Fig. B1, and the sign of θ_K also changes as the injected electrons have an opposite spin polarization and go through the valley Hall transport toward an opposite direction compared to the case when the remote pump has σ^+ helicity.

B.2 Electronic probing of valley Hall transport

In Chapter 3, the spatially resolved differential PL and PL spectroscopy were used to argue that the spin-polarized electron generated by the remote pump in the monolayer WTe_2 is effectively converted into valley polarization in the monolayer MoS_2. To supplement this, conventional electronic transport measurement was also performed using the heterostructure device with similar geometry.

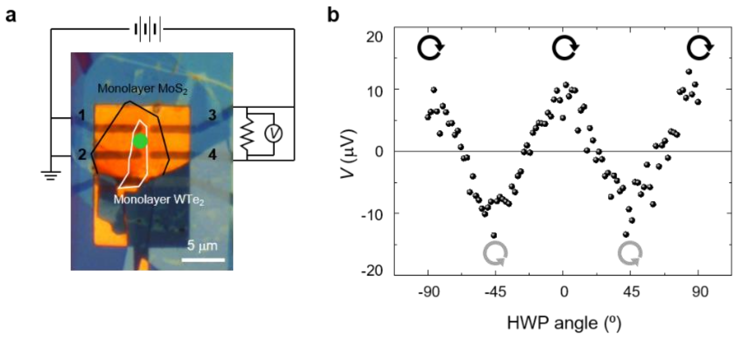

Figure B3. a. Optical microscopy image of the device used in the electrical probing of valley Hall transport. The green dot denotes the position of the CW pump (2 μm of spot size). The pump helicity-dependent voltage measured between contacts 3 and 4 shows a significant change of the voltage with respect to the helicity of the 1.55 eV pump, while there is no direct photoexcitation in MoS_2.

Figure B3a shows the optical microscope image of the device. Under the presence of a longitudinal electric field between contacts 1, 2, and 3, 4, the voltage difference induced in contact 3 and 4 was measured to detect the transversal valley Hall transport. The pump helicity-dependent voltage shown in Fig. B3b reveals there is a transversal transport corresponding to the helicity of the circularly-polarized pump. Note that the SHE induced in the monolayer MoS_2 also can derive the identical helicity-dependent photo-voltage. However, the magnitude of spin Hall conductance is negligible compared to the valley Hall conductance, as discussed in Chapter 3, thus, the observed helicity dependence supports the effective injection of a spin-valley polarized electron in the MoS_2/WTe_2 heterostructure device.

APPENDIX C - SUPPLEMENTARY DATA FOR CHAPTER 4

C.1 Extended dataset – B_z-dependent spatially resolved $\Delta\theta_K$

In Chapter 4, the line-cut plots of V_G-dependent spatially resolved $\Delta\theta_K$ under B_z were presented to show the connection between the localized $\Delta\theta_K$ and the time-reversal symmetry. Here, the full 2D plots of $\Delta\theta_K$ are shown.

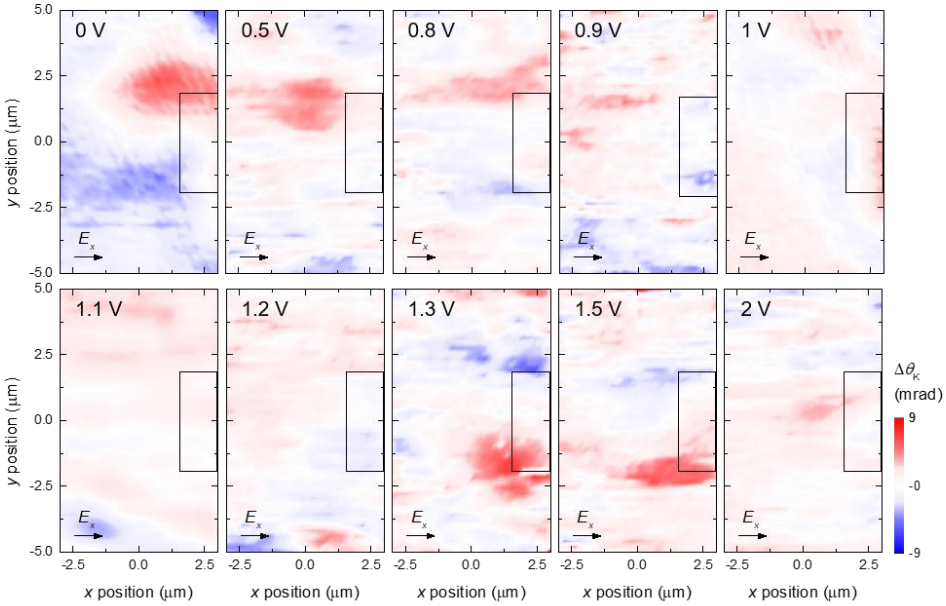

Figure C1. The full 2D contour plots of the V_G-dependent $\Delta\theta_K$ measured in device #1 when B_z = 0.5 T was applied. The bias voltage of 0.5 V was applied to generate a longitudinal electric field in +x direction.

When the external magnetic field of B_z = 0.5 T was applied, the $\Delta\theta_K$ localized at the y-position of hinges diminished at the V_Gs near the charge neutral point of WTe_2 (Fig. C1). This indicates the mass gap opening of hinge states due to the breaking of time-reversal symmetry, as discussed in Chapter 4.

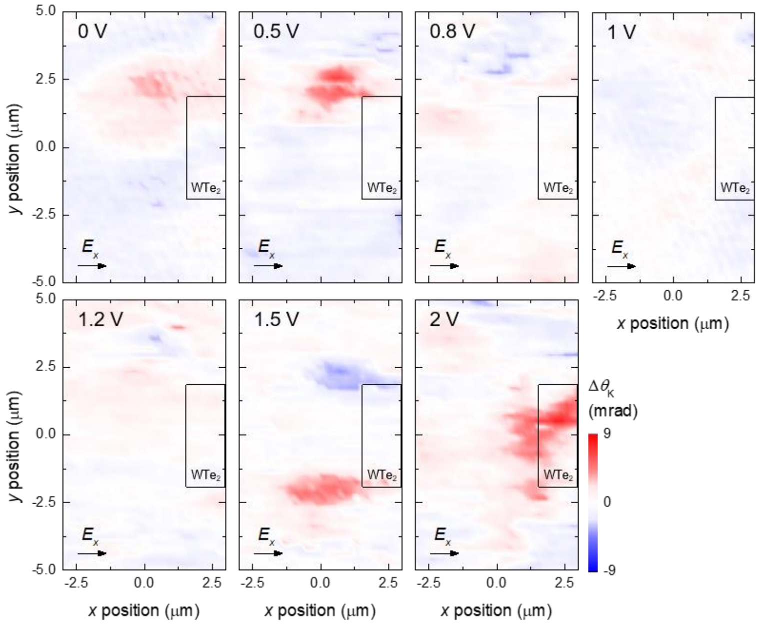

Figure C2. The full 2D contour plots of the V_G-dependent $\Delta\theta_K$ measured in device #1 when B_z = 1 T was applied. The bias voltage of 0.5 V was applied to generate a longitudinal electric field in +*x* direction.

As the B_z increased to 1 T, the range of V_G that has suppressed $\Delta\theta_K$ at the y-position of hinges got broadened, as shown in Fig. C2.

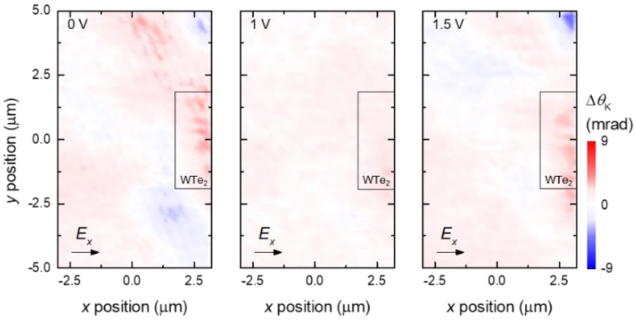

Figure C3. The full 2D contour plots of the V_G-dependent $\Delta\theta_K$ measured in device #1 when B_z = 2 T was applied. The bias voltage of 0.5 V was applied to generate a longitudinal electric field in $+x$ direction.

The V_G-dependent $\Delta\theta_K$ measured when 2 T of B_z has applied shows no clue of the spinful hinge states. Such a disappearance can be achieved by the merging of gapped hinge states with the bulk conduction/valance bands or complete topological phase transition of the multilayer WTe_2.

C.2 Spatially resolved $\Delta\theta_K$ from the additional devices

Two additional devices were made to check the consistency of spatially resolved $\Delta\theta_K$ measurement and confirm that the spinful hinge state is a general phenomenon that appears on the multilayer WTe_2 crystals of various thicknesses. The optical microscope images of all devices used in the study, including devices #1 and #4 which were mentioned in Chapter 5, are shown in Fig. C4. Figure C5 shows the thickness of WTe_2 in each device checked by the AFM measurements and the corresponding number of atomic layers are marked in the figure. Figure C6 shows the V_G-dependent electrical characteristics of the devices. The characteristics and parameters of each device are organized in Table C1.

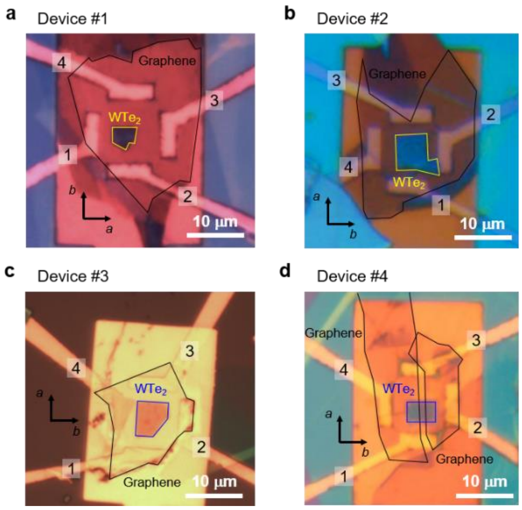

Figure C4. Optical microscope images of devices #1~4. Device #4 has a 1.5 μm wide gap in the middle of the graphene. The contact indices are marked with the numbers 1~4 in each image. The black arrows in each picture show the crystal axes orientation of multilayer WTe_2.

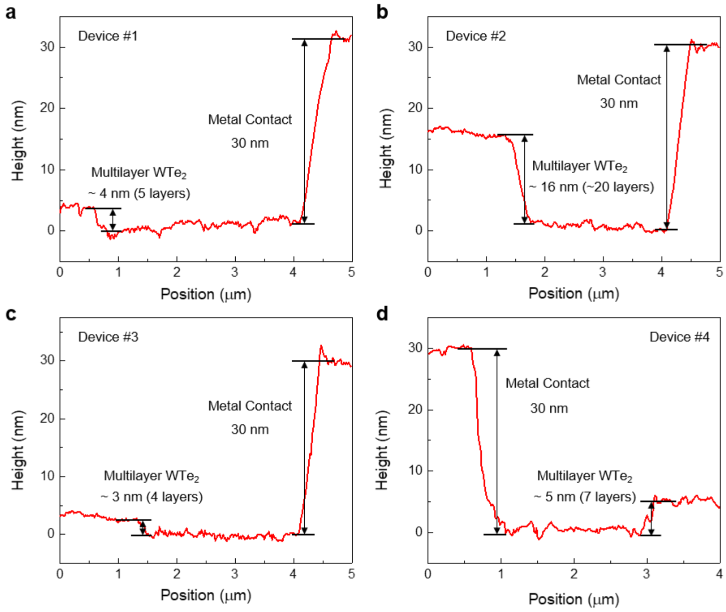

Figure C5. AFM data shows the thickness of multilayer WTe_2 crystal in each device. The thickness of metal contact (Ti 5 nm, Au 25 nm) was measured for reference

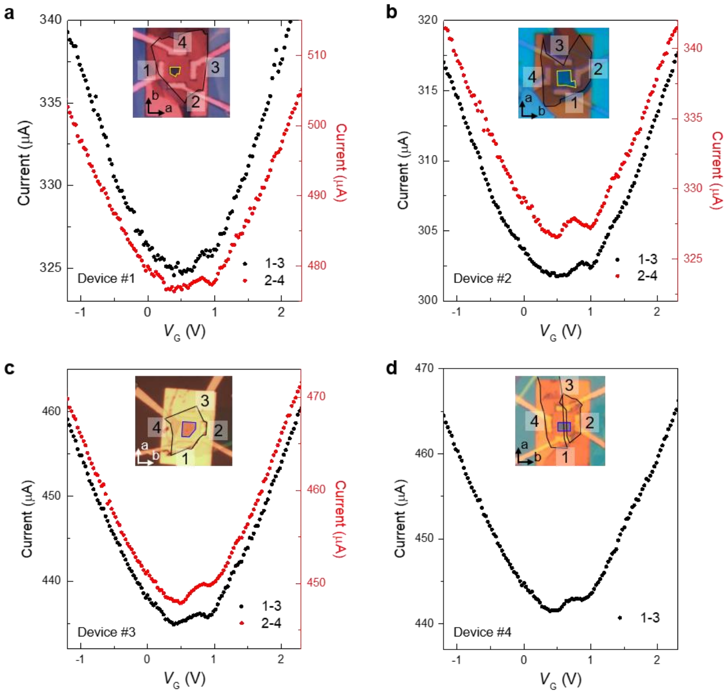

Figure C6. V_G-dependent current characteristics measured in devices #1~4 are shown. The current between contact 1, 3 (2, 4) corresponds to the current along the *a*- (*b*-) axis of multilayer WTe_2 in each device.

Table C1. Thickness and V_{CNP} of each device used in the experiments. V_{CNP} is the V_G that corresponds to the charge neutral point (i.e., Dirac point) of the multilayer WTe_2.

Device	WTe_2 thickness (nm)	Number of layers	V_{CNP} (V)
Device #1	4	5	0.95
Device #2	16	~ 20	1
Device #3	3	4	0.92
Device #4	5	7	0.88

The V_G-dependent spatially resolved $\Delta\theta_K$ observed in the supplementary devices (devices #2 and #3) are shown in Fig. C7. All the measurements were performed under the same conditions, i.e., cryogenic condition, data acquisition setting, and bias voltage. The resultant $\Delta\theta_K$ distributions observed in devices #2 and #3 are identical to the result obtained from device #1; it is localized at *y*-positions of the WTe_2 hinges and flips its sign as V_G passes across V_{CNP}, showing that the spinful states are localized at the hinges of multilayer WTe_2

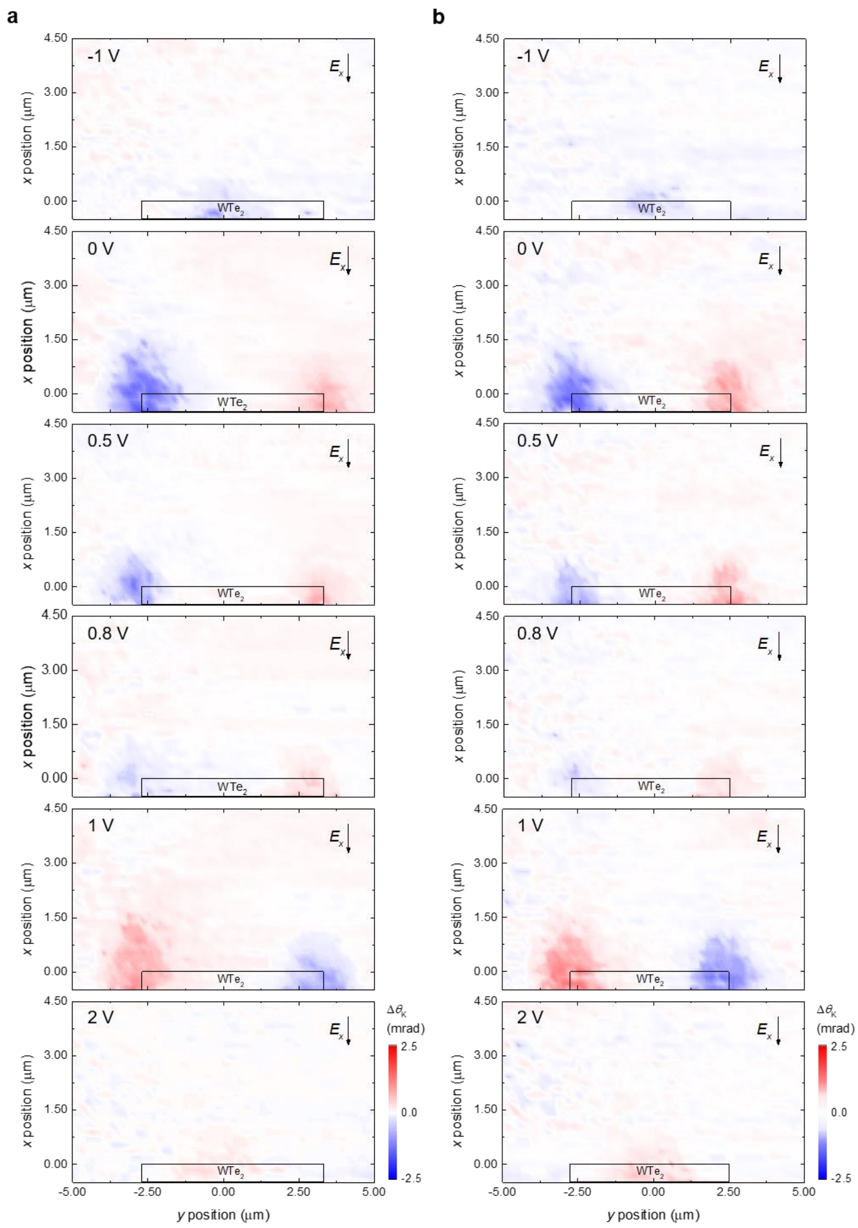

Figure C7. V_G-dependent spatially resolved $\Delta\theta_K$ from devices #2 (**a**) and #3 (**b**).

ABSTRACT (KOREAN)

위상 물질에서의 스핀 수송에 대한 광학적 연구

물질의 위상학적 상태라는 개념의 발견은 고체 밴드 이론의 새로운 장을 열었다. 많은 연구들을 통해 위상학적 밴드 특성에 대해 이해할 수 있게 되었고, 최근의 소자 제작 및 측정 방법론에 있어서의 발전에 힘입어 실험을 통한 실증의 방면에서도 큰 진보가 있었다. 위상학적 현상을 연구하기 위해서 고안된 여러 실험 방법 중, 본 학위논문은 광학적 측정을 통해 전자 스핀을 관찰하는 것에 초점을 맞춘 연구들을 다룬다. 특히, 물질의 광학적 특성을 직접 측정하는 기존의 방식에서 벗어나 광학 실험이 가지는 한계점을 극복하기 위해 특별히 고안된 반데르발스 이종접합 소자를 제작하였으며 이를 이용해 전자 수송의 스핀 자유도와 관련된 특성을 구별해내는 연구가 수행되었다.

시간- 및 공간-분해 광학 측정을 이용한 위상학적 스핀 수송에 대한 첫 번째 연구에서는 잘 알려진 전이금속 디칼코게나이드 MoS_2 에서의 밸리 홀 효과를 관찰하였다. 기존의 밸리 홀 효과 연구들이 직접적인 광 여기를 통해 밸리 분극을 형성하거나 전기적 측정을 통해 평형상태에서의 밸리 홀 효과를 관찰했던 것에서 더 나아가, 이차원 위상절연체인 단일층 WTe_2 와의 접합을 통해 광-여기 스핀 정렬 전자를 주입하고 이로써 생성된 밸리 분극을 MoS_2 에서 광학적으로 검출하는 방식을 사용함으로써 엑시톤에 의해 밸리 분극 수명이 제한되는 것을 피할 수 있었다. 그 결과 엑시톤 형성시 나타나는 Maialle-Silva-Sham 교환 반응이 억제되었고 4 ns 이상의 밸리 분극 수명과 4.49×10^3 cm^2/Vs 이 넘는 밸리 홀 전자이동도를 관찰할 수 있었다. 더 나아가 공간–분해 초고속 커 회전 측정을 통해 밸리 홀 효과의 알려진 원인들 중 실험결과를 잘 설명하는 성분을 찾아냄으로써 앞서 관찰되었던 MoS_2 의 비–엑시톤 밸리 홀 효과가 어떠한 원리로 형성되는지도 규명하고자 하였고, 밸리 홀 전도도와 밸리 홀 수송 수명의 비교와 이론 계산을 통해 밴드의 특성인 베리 곡률에 의해서 발생하는 내재적 밸리 홀 효과가 관찰된 밸리 홀 수송의 지배적인 원인이라는 것을 알아낼 수 있었다.

앞서 기술한 비-엑시톤 밸리 홀 효과의 연구에 사용되었던 스핀-정렬 전자 주입 개념을 활용하여 고차 위상절연체가 가지는 모서리 준위의 스핀 특성을 연구하였다. 고차 위상절연체는 최근에 제안된 새로운 위상학적 상태로, 이를 설명하는 모델과 물리적 특성에 대한 많은 이론 연구가 이루어지고 있지만 실제 고차 위상절연체 물질에 대한 실험은 제한적으로만 이루어져 왔다. 특히, 스핀 정렬 특성을 가지는 고차 위상절연체의 모서리 준위에 대한 실험적 증거는 보고된 바가 없었기 때문에 본 논문의 저자는 다중층 WTe_2 와 그래핀의 이종접합 구조를 이용한 소자에 대한 커 효과 측정을 통해 초전도 전류를 이용한 기존의 실험 방식이 가지는 한계를 극복하고자 하였다. 해당 연구에서 다중층 WTe_2 의 모서리 준위에서 그래핀으로 전자를 주입하고 그래핀에서 자기-광 효과에 대한 공간 분해 측정을 수행함으로써 모서리 준위가 스핀 정렬을 가지고 있다는 것을 성공적으로 보일 수 있었으며, 외부 자기장에 의한 위상학적 상태의 교란을 관측함으로써 관찰한 모서리 준위가 시간-역전 대칭성에 의해 보호되는 위상학적 준위임을 증명하였다.

Keywords: 위상절연체, 전이금속 디칼코게나이드, 초고속 분광학, 테하레르츠 분광학, 디락 페르미온, 엑시톤, 표면 플라즈몬, 파노 공명, 광 스타크 효과

LIST OF PUBLICATIONS

1. (**1st author**) **J. Lee**, J. Kwon, E. Lee, J. Park, S. Cha, K. Watanabe, T. Taniguchi, M.-H. Jo, and H. Choi, Spinful hinge states in the higher-order topological insulators WTe_2. *In preparation*.

2. (Co-author) G. Jin*, C. Lee*, Odongo F. N. Okello, S. Lee, M. Park, S. Cha, S. Seo, G. Moon, D. Yang, C. Han, H. Ahn, **J. Lee**, H. Choi, J. Kim, S. Choi, and M. Jo, Heteroepitaxial van der Waals semiconductor superlattices. *Nat. Nanotechnol.* **16**, 1092-1098 (2021).

3. (**1st author**) **J. Lee***, W. Heo*, M. Cha, K. Watanabe, T. Taniguchi, J. Kim, S. Cha, D. Kim, M. Jo, and H. Choi, Ultrafast non-excitonic valley Hall effect in MoS_2/WTe_2 heterobilayers. *Nat. Commun.* **12**, 1635 (2021).

4. (Co-author) S. Sim*, H. Shin*, D. Lee, **J. Lee**, M. Cha, K. Lee, and H. Choi, Opposite behavior of the ultrafast dynamics of the exciton shift and the linewidth broadening in bilayer ReS_2. *Phys. Rev. B* **103**, 014309 (2021).

5. (Co-author) S. Paik*, G. Kim*, S. Chang, S. Lee, D. Jin, K. Jeong, I. Lee, **J. Lee**, H. Moon, J. Lee, K. Chang, S. Choi, J. Moon, S. Jung, S. Kang, W. Lee, H. Choi, H. Choi, H. Kim, J. Lee, J. Cheon, M. Kim, J. Myoung, H. Park, and W. Shim, Near-field sub-diffraction photolighography with an Elastomeric photomask. *Nat. Commun.* **11**, 805 (2020).

6. (Co-author) S. Sim*, D. Lee*, **J. Lee**, M. Cha, S. Cha, W. Heo, S. Cho, W. Shim, K. Lee, J. Yoo, R. P. Prasankumar, H. Choi, and M. Jo, Role of weak interlayer coupling in ultrafast exciton-exciton annihilation in two-dimensional rhenium dichalcogenides. *Phys. Rev. B* **101**, 174309 (2020).

7. (Co-author) S. Sim*, S. Lee*, J. Moon, C. In, **J. Lee**, M. Noh, J. Kim, W. Jang, S. Cha, S. Seo, S. Oh, D. Kim, A. Soon, M. Jo, and H. Choi, Picosecond competing dynamics of apparent semiconducting-metallic phase transition in the topological insulator Bi_2Se_3. *ACS Photonics* **7**, 759-764 (2020).

8. (Co-author) S. Sim, D. Lee, **J. Lee**, H. Bae, M. Noh, S. Cha, M. Jo, K. Lee, and H. Choi, Light polarization-controlled conversion of ultrafast coherent-incoherent exciton dynamics in few-layer ReS_2. *Nano Lett.* **19**, 7464-7469 (2019).

9. (Co-author) S. Cha*, M. Noh*, J.-H. Kim, J. Son, H. Bae, D. Lee, H. Kim, **J. Lee**, H. Shin, S. Sim, S. Yang, S. Lee, W. Shim, C.-H. Lee, M.-H. Jo, J. S. Kim, D. Kim, and H. Choi, Generation, transport, and detection of valley-locked spin photocurrent in WSe_2-graphene-Bi_2Se_3 heterostructures. *Nat. Nanotechnol.* **13**, 910-914 (2018).

10. (**1st-author**) **J. Lee**, S. Sim, S. Park, C. In, S. Cho, S. Lee, S. Cha, S. Lee, H. Kim, J. Kim, W. Shim, J. Kim, D. Kim, and H. Choi, Role of spin Hall effect in the topological side surface conduction. *ACS Photonics* **5**, 3347-3352 (2018).

11. (**1st-author**) **J. Lee***, S. Cho*, S. Park, H. Bae, M. Noh, B. Kim, C. In, S. Yang, S. Lee, S. Y. Seo, J. Kim, C. -H. Lee, W. -Y. Shim, M. -H. Jo, D. Kim, and H. Choi, Highly efficient computer algorithm for identifying layer thickness of

atomically thin two-dimensional materials. *Jour. Phys. D: Appl. Phys.* **51**, 11LT03 (2018).

Presentations

1. **(International) J. Lee** "Spin and charge dynamics across the topological heterojunction in monolayer 1T′-WTe_2", Oral presentation, Conference on Lasers and Electro-Optics (CLEO) 2019, San Jose, USA

2. (Domestic) J. Lee "Ultrafast measurement of persistent valley Hall effect by spin injection across the MoS_2/WTe_2 interface", Oral presentation, 2019 KPS Fall Meeting, Gwangju, Korea

3. (Domestic) J. Lee "Spin and charge dynamics of the quantum spin Hall state across the topological heterojunction", Oral presentation, Optical Society of Korea (OSK) Winter Annual Meeting 2019, Hoengseong, Korea

4. (Domestic) J. Lee "Ultrafast study of unipolar valley Hall effect using van der Waals heterobilayer", Oral presentation, Optical Society of Korea (OSK) Summer Meeting 2020, Busan, Korea

5. (**International**) **J. Lee** "Ultrafast study of non-excitonic valley Hall effect in MoS_2/WTe_2 heterojunctions", Oral presentation, Advanced Lasers and Their Applications (ALTA) 2021, Seogwipo, Korea

6. (Domestic) **J. Lee** "Optical observation of the spinful higher-order topological hinge state in multilayer WTe_2", Oral presentation, Optics and Photonics Congress (OPC) 2021, Seogwipo, Korea

7. (**International**) **J. Lee** "Higher-order topology in twisted bilayer WTe_2", Oral presentation, The 12th Recent Progress in Graphene and Two-dimensional Materials Research Conference, Seoul, Korea

8. (**International**) **J. Lee** "Observation of the spinful higher-order topology in multilayer T_d-WTe_2", Oral presentation, CLEO 2022, San Jose, USA